AN INVESTIGATION INTO THE RELATIONSHIPS BETWEEN THE GEOMAGNETIC FIELD, COSMIC RAYS AND TRAPPED PARTICLES BY MEANS OF THE EARTH SATELLITE ARIEL I

THESIS

submitted by

ALASTAIR CHANTRY DURNEY

for the degree of

DOCTOR OF PHILOSOPHY

in the

UNIVERSITY OF LONDON

April 1964

ABSTRACT

This thesis describes how the magnetic rigidity spectrum of primary cosmic rays with Z greater than or equal to three in the rigidity interval between 2.5 and 16.0 Gv. has been determined by means of a cerenkov counter carried in Ariel I. There is a clear change of slope in the spectrum at 8.5 Gv and this is tentatively interpreted as the upper limit to the solar modulation at this time (May - June, 1962).

The characteristics of the detector allowed an analysis of the effects of the 'Starfish' nuclear explosion. Evidence has been found for the redistribution of the geomagnetically trapped radiation in the region between L = 4.7 and 3.2 earth radii by an explosion-generated hydromagnetic wave. After the explosion a shell of electrons was found centred on L = 1.14, continuously fed by the decay of fission fragments which remained in the vicinity of the explosion. An artificial radiation belt was observed and electrons from fission fragment decay were found out as far as L = 5 earth radii. At high L values the energy spectrum of the artificial radiation belt particles was softer than that of electrons from fission fragment decay. The 'sweeping' effect of the Earth's southern magnetic anomalies on the lower edge of the artificial radiation belt is demonstrated and a short-lived decay mechanism was observed in action.

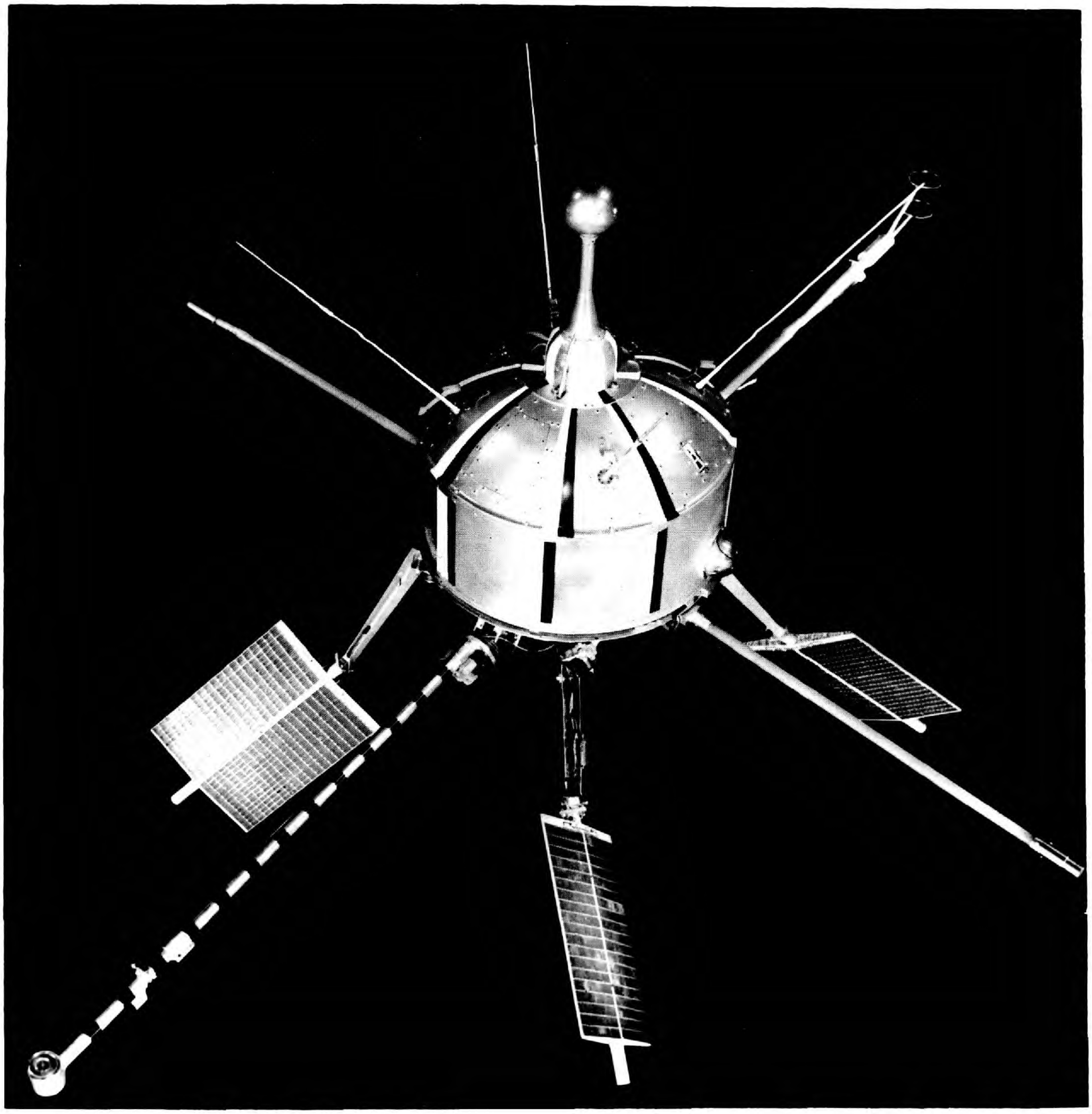

The Earth Satellite Ariel I.

CONTENTS

CHAPTER 1

GENERAL INTRODUCTION

Work over the past two decades has shown that the sun exerts a profound influence on both the intensity and energy spectrum of the cosmic ray flux incident on the top of the earths' atmosphere. An eleven year cycle of intensity variation has been found and correlated with the sunspot cycle, sudden increases in the radiation intensity have been associated with solar flares, and many other examples of the suns' effects have been discovered. Models of the interplanetary fields and mechanisms whereby the cosmic ray intensities may be modulated by the sun have been propounded on the basis of the experimental results. The diversity of these models emphasize how little of this subject is known, but they do serve to illustrate that more information regarding the strengths and directions of the magnetic fields in interplanetary space and accurate knowledge of the energy dependance of the modulation process are required before details of the true mechanisms can be exposed.

The technique of making measurements from probes and earth satellites has proved to be a very powerful tool for investigating the near environment of the earth in space. During the past six years an unexpected picture of the earths' magnetosphere and its associated phenomena has begun to be assembled from pieces of information gleaned by these methods (eg. Parker 1962, Gold 1962.). It is to be expected that in the near future some information about limited parts of the interplanetary magnetic and electric fields will be gained by direct measurements made from space probes, indeed these have already begun (eg. Pioneer V and Mariner II). However the only method available at present for studying the large-scale configuration of the interplanetary field is to observe its effect on the numbers and energies of primary cosmic rays. For satisfactory results, these observations should be made over a long period of time.

At first sight, this condition would seem to be satisfied by ground-based detectors, numbers of which have been operated continuously for several years. Unfortunately these detectors can only measure the secondary particles produced by the interaction of the primary radiation and the atmosphere. The yield of secondary particles varies with the energy of the primary ray so ground-based detectors cannot measure the energy spectrum of the primary radiation without knowledge of the yield functions. The yield functions in turn cannot be calculated because of lack of knowledge of the interaction processes; yield functions obtained from empirical data have so far only achieved a limited accuracy (eg. Webber and Quenby 1959). For these reasons ground-based detectors are unsuitable for making accurate measurements of the primary cosmic ray spectrum.

The problem of yield functions may be overcome by using detectors carried by balloons. The lifetime of these is only a few hours, but numerous individual measurements of the primary spectrum have been made using balloons flown at pressures of 10 gm/cm^2 or less. However, statistical and experimental limitations have resulted in a low accuracy of results and in an almost complete lack of empirical information concerning the time variations of nuclei heavier than alpha particles. These heavy nuclei are likely to provide the most accurate measurements of the primary spectrum since the proton and alpha particle flux measurements are contaminated by secondary processes and by particles thrown out of the sun.

All these difficulties may be overcome by using a heavy nuclei detector flown in a satellite. This instrument would be able to monitor the primary radiation directly, and would be expected to operate for several months. If another detector was flown at aeroplane altitudes during the lifetime of this detector, the yield functions could be calculated and the measurements continued after the satellite instrument had ceased to function. Thus long-term changes in the spectrum could be detected. This extension of the experiment is based on the assumption that the energy spectrum for primary protons and alpha particles is not different from that of the heavier nuclei.

It has been known for some time that the earth acts as a magnetic spectrometer; particles with lower rigidities are excluded from regions of the earths' surface nearer to the equator. Both the aeroplane and satellite instruments would use this effect to measure the different energies (rigidities) of the primary rays. The rigidity thresholds at different latitudes and longitudes have been calculated by several investigators. The most accurate, worldwide results available at present are the vertical, sea level threshold rigidities calculated by Quenby and Wenk (1962) for all latitudes lower than 70 degrees. The accuracy of of these threshold rigidities, when adjusted to satellite conditions, is the factor which limits the accuracy of the experiment at present. It is hoped in turn that the accuracy of the threshold rigidities may be improved by using the results of the satellite and aeroplane surveys.

In addition to its ability to monitor the primary radiation directly over comparatively long periods of time, a satellite instrument has the potential to make fast measurements of the primary spectrum. This arises because a satellite scans its complete range of latitudes four times every orbit, and so the range of threshold rigidities is completely swept about every half hour. If the counting rates were large enough this would enable spectral time variations of only a few hours to be detected. Unfortunately, no such time variations were observed during the lifetime of our satellite instrument, also the counting rate was probably too low to have detected any changes other than extremely large ones.

The data from the instrument which was conceived on the basis of the above arguments and was flown in Ariel I are still being analysed. This thesis is concerned with a preliminary estimation of the quiet period cosmic ray primary spectrum and a detailed analysis of the Starfish high altitude nuclear explosion as seen by our instruments. As the cerenkov unit could detect the presence of large numbers of electrons with energies greater than about 2.5 Mev, and since our instrument package included a geiger counter, the examination of the artificial radiation has yielded more results than might be expected from a device designed to investigate only the heavy primary radiation. The estimation of the primary spectrum is more accurate than those previously obtained by other experimenters in this field (Pomerantz and Witten, 1962; Kurnosova, Logachev, Razorenov and Fradkin, 1962).

CHAPTER 2

THE APPARATUS

2.1 Experimental Philosophy.

The object of this experiment was to measure the primary cosmic ray flux at different geomagnetic latitudes. The measurements were to be contaminated with the least possible numbers of natural radiation belt particles, albedo particles, and solar accelerated particles.

In order to achieve this, a cerenkov detector was designed as is shown in figure 2. The cerenkov material (perspex was chosen for its low scintillation property) was in the form of a thin, hollow sphere, four inches in diameter and coated with a white diffusing paint on the outside so that it acted as its own light integrating sphere. Bursts of light produced by relativistic particles in the 3 mm. thick perspex were detected by a photomultiplier, type VMP 11/44 R, made by 20th Century Electronics Ltd. The photocathode of this photomultiplier fitted into a two inch diameter hole in the side of the sphere. The electrical pulses so produced at the photomultiplier anode were passed through an impedance transformer and a variable attenuator into a discriminator (see figure 3). When one of these pulses was large enough to fire the discriminator, the latter passed a pulse through a gate into an 8-binary store. The contents of this store were examined every 2.56 seconds by a 'high speed encoder', the information then being telemetred directly to the ground. Every 30.72 seconds the store was examined by

Figure 2

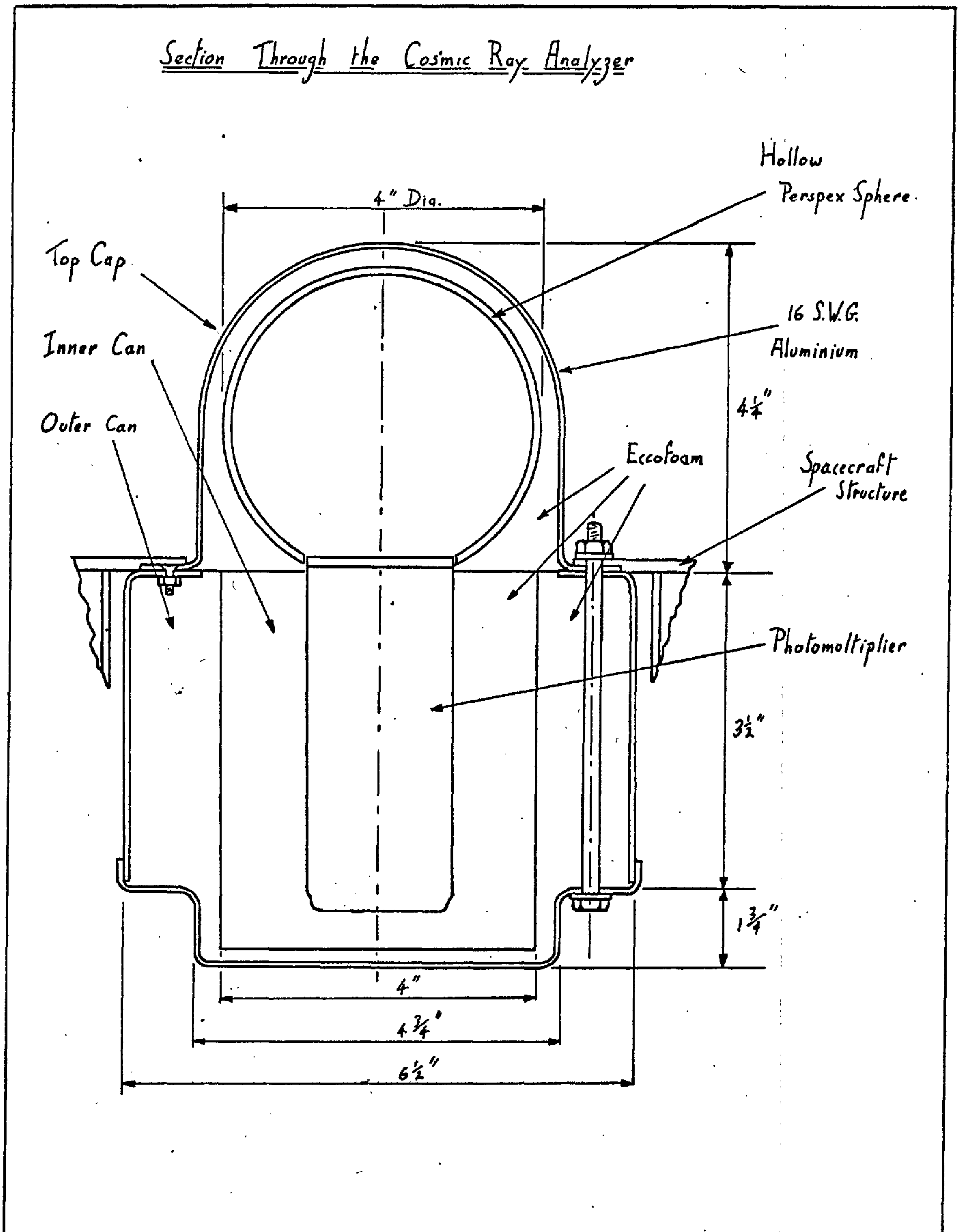
Section Through the Cosmic Ray Analyzer
Hollow
Perspex Sphere
4" Dia.
Top Cap
16 S.W.G.
Aluminium
Inner Can
Outer Can
4¼"
Eccofoam
Spacecraft
Structure
Photomultiplier
3½"
1¾"
4"
4¾"
6½"

Figure 3.

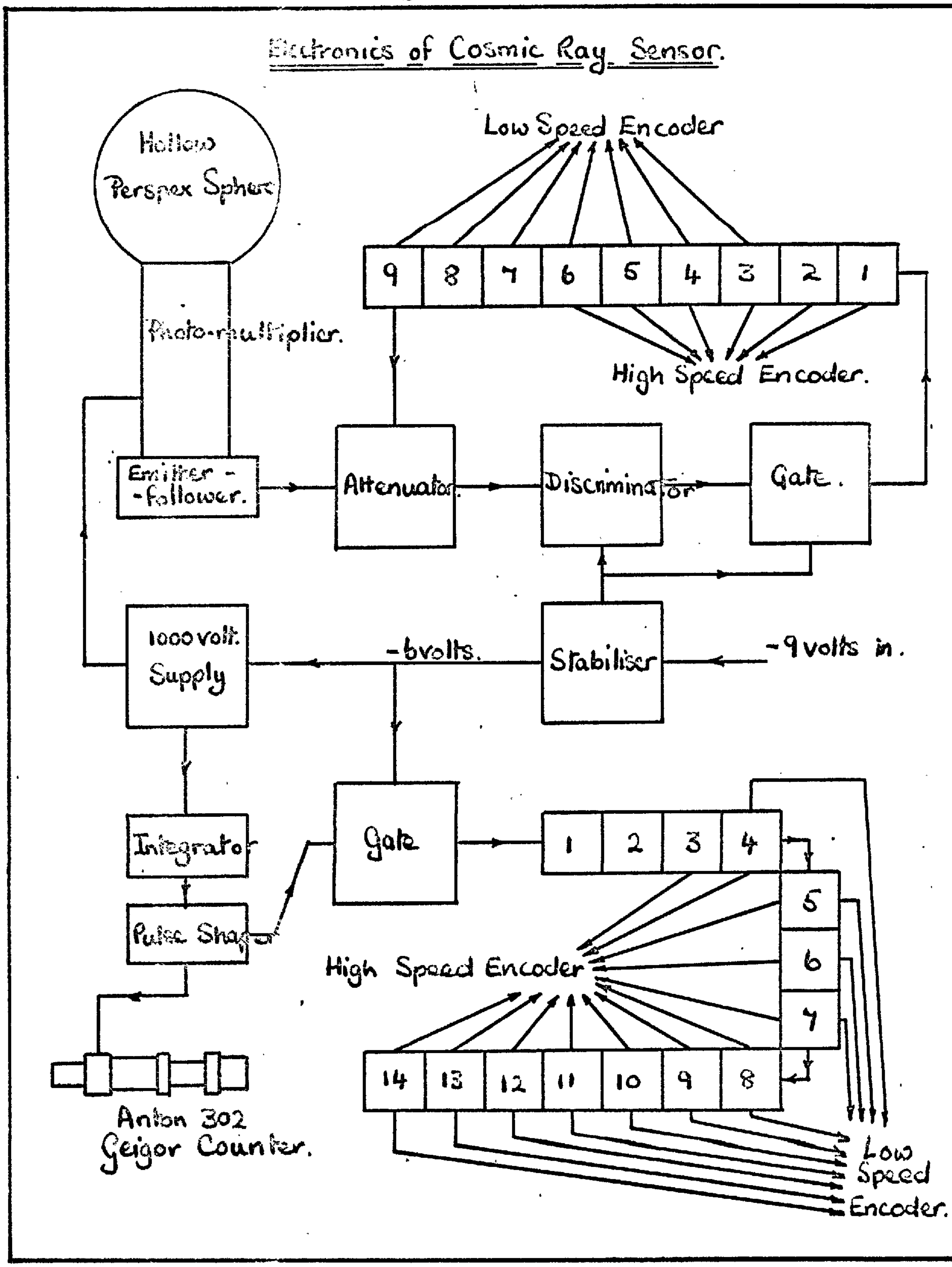
Electronics of Cosmic Ray Sensor.
Hollow Perspex Sphere
Photo-multiplier.
Emitter - -follower.
Attenuator.
Discriminator
Gate.
Low Speed Encoder
High Speed Encoder.
9
8
7
6
5
4
3
2
1
1000 volt. Supply
-6volts.
Stabiliser
-9 volts in.
Integrator
Pulse Shaper
Gate
High Speed Encoder
1
2
3
4
5
6
7
8
9
10
11
12
13
14
Low Speed Encoder.
Anton 302 Geiger Counter.

a 'low speed encoder' which transferred this information to a tape recorder. For the duration of this latter examination (1.92 seconds) the gate between the discriminator and the store was closed in order to prevent the store contents changing. The tape recorder could be played back at 48 times the recording speed by a command signal transmitted from the ground, Thus data obtained over a period of 100 minutes (the time equivalent to the capacity of the tape recorder) could be collected in just over two minutes by one tracking station. As this 100 minutes represented one complete orbit, this enabled the experimenters to recover 70 % of the available data between the launch and July 12th. For some periods 90 % data recovery was achieved.

By using a cerenkov detector, it was hoped to eliminate all non-relativistic radiation from the measurements. The relativistic components of the natural radiation belts and of albedo have negligible numbers of particles with charges greater than two. Furthermore, the proportion of singly and doubly charged particles in the total flux of solar-accelerated particles is greater than for cosmic rays in general (Biswas et al., 1962). Since cerenkov light produced by a particle is proportional to Z^2 where Z is the charge on the particle, it is possible to set the dicriminator level so that particles with a charge of 2 or less are not detected. In this way contamination by albedo and radiation belt particles is eliminated and that from solar-accelerated particles considerably reduced. Therefore the genuine cosmic ray flux may be measured free from serious contamination if the reduction in counting rate can be tolerated. The detector was designed to have a large area (80 cm^2) and to be sensitive to particles arriving from as large a solid angle as possible in order to counteract this disadvantage. By means of the large solid angle it was hoped also to reduce counting rate variations due to the different orientations of the detector with respect to the Earth. In practice, the limitations to the solid angle were set by the positions of the electronic packages in the body of the satellite. The unit was mounted on the spin axis of the satellite so that the orientation of its sensitive solid angle would be independent of the spin.

Instead of rejecting only all those particles with charges of two or less, the instrument was designed so that the discrimination level could be doubled from time to time, thus rejecting a slightly larger range of particles. This was done simply by arranging that a ninth binary added on to the cerenkov store should vary the attenuation between the photomultiplier and the discriminator. Thus the sensitivity changed every 256th count. This addition was made in order to provide some form of check on the system; if the spectra computed from the two different levels of sensitivity agree, then it is reasonable to say that the spectrum does not depend on the gain of the apparatus.

On the unit flown, the ratio of the pulse heights required to fire the discriminator on the seperate sensitivities was 1.83 ∓ 0.05. However, owing to the poor geometry of the system, the rejection of particles did not occur at single discrete levels. The problem of determining the efficiences of the system for various nuclei is extremely complex, but the table in figure 37 has been constructed from the calibration data and the abundance spectrum of the primary cosmic radiation (Waddington, 1961), and gives an approximate idea of the numbers involved. Figure 37 and details of the calculation are to be found in Appendix B.

Since the particle populations in the radiation belts are very high, it would have been optimistic indeed to expect them to have no effect whatsoever on the cerenkov detector. For this reason a small geiger counter was included in the instrument package so that the radiation belts could be detected. By means of an integrating device the geiger counter was arranged to cut off at counting rates greater than about 80 counts per second. This was done to safeguard the voltage applied to the photomultiplier which was operated from the same high tension supply as the geiger counter, and to prevent possible ambiguities arising because of the geiger store being filled more than once in between low speed encoder samples. The geiger counter used was an Anton 302 with 1 mm. of lead shielding. The minimum total shielding was as follows;

Aluminium	1.01 gm/cm^2,
Eccofoam	0.73 gm/cm^2,
Lead	1.13 gm/cm^2,
Iron	0.4 gm/cm^2.

This gives a total of 3.27 gm/cm^2 which allows a 10 % probability of penetration for 7.4 Mev electrons or a 50 % penetration probability for 10.5 Mev electrons. By using a proton accelerator it has been found that the penetration threshold for protons is about 43 Mev. The geometrical factor of the counter is 0.6, it has an efficiency of 0.3 % for γ photons and an efficiency of 80 % for fast electrons and cosmic rays. For electrons detected by means of the bremsstrahlung they produce in the aluminium shell of the unit, the overall efficiency has an upper limit of 0.001 % (based on figures given by O'Brien et alii, 1961). From this it may be calculated that one count per sampling interval is equivalent to the following flux;

0.08 electrons/cm^2/second, (by direct penetration)
or 20 γ rays/cm^2/second,
or 6×10^3 electrons/cm^2/second (bremsstrahlung, lower limit).

Note that the actual time available for counting during a 30.72 second interval was only 26.88 seconds owing to the 3.84 second gating pulse of the geiger channel.

2.2 Construction.

McMichael Radio Ltd. of Slough built two prototype units and three flight units to our specifications. The mechanical construction of the unit and its position in the satellite may be understood by examining figures 4, 5, 6 and 7. The mass of the completed units including the eccofoam was 2,410 gm. The power consumption was 11 milliamperes at -6.6 volts and 18 milliamperes at -9 volts. The operating temperature limits were 60°C and -15°C.

Details of the electronic circuits were given by Elliot, Quenby, Mayne and Durney, 1961.

Figure 4

The Ariel I Cosmic Ray Unit.

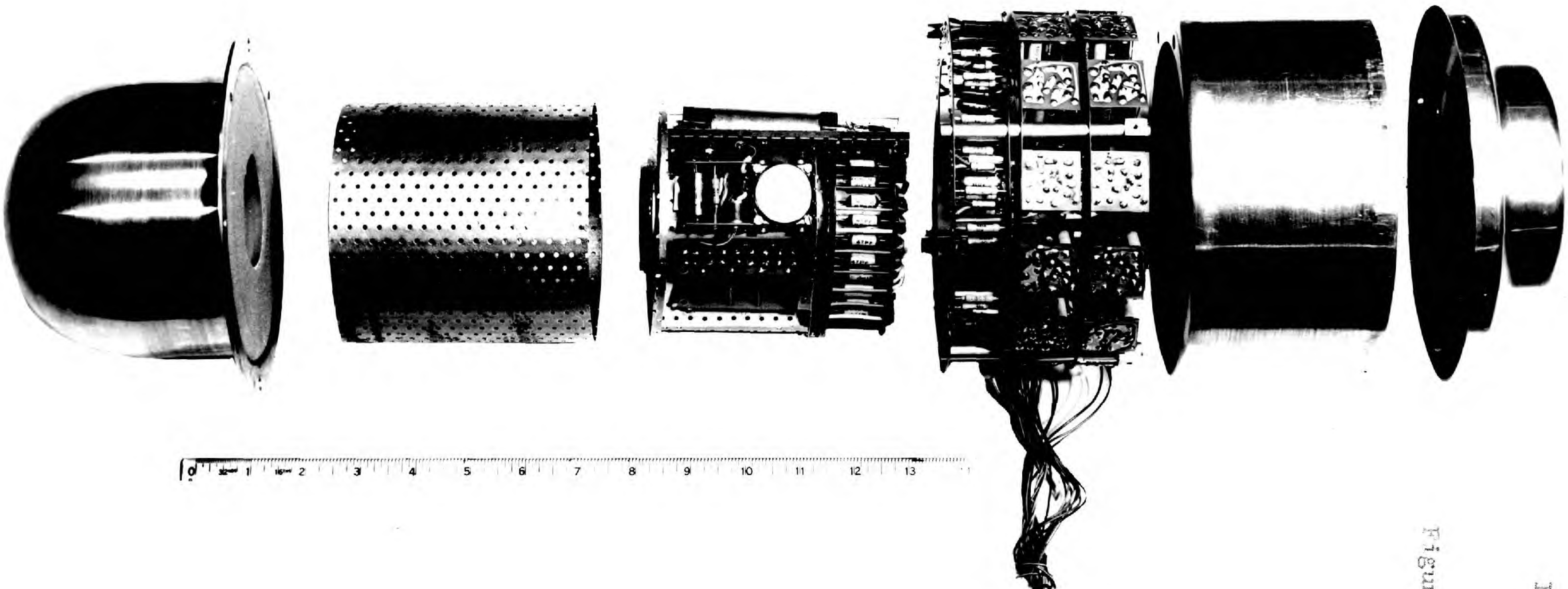

Figure 5

An Exploded View of the Cosmic Ray Unit.

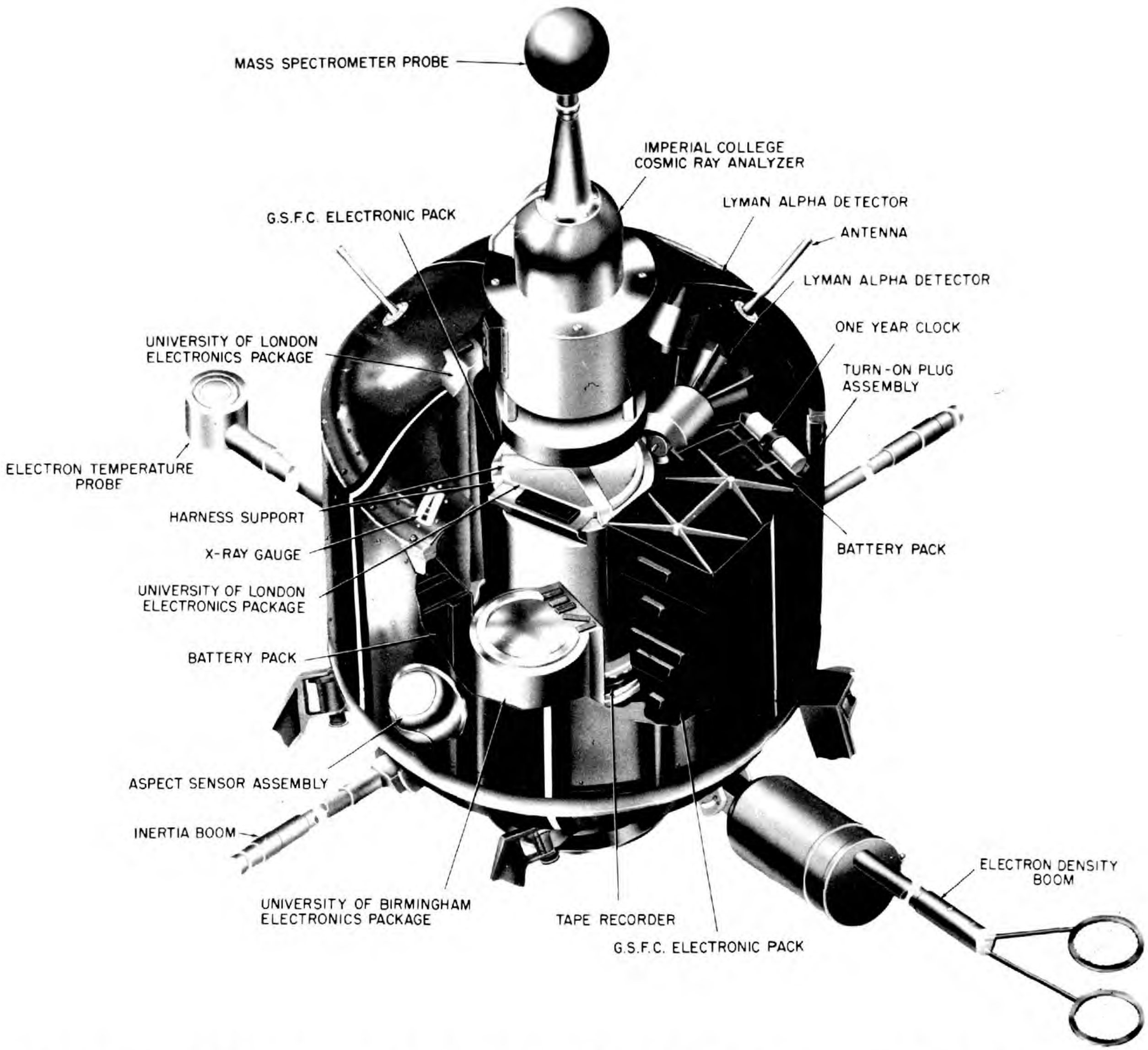

INTERNATIONAL IONOSPHERE SATELLITE

Figure 6

Figure 7

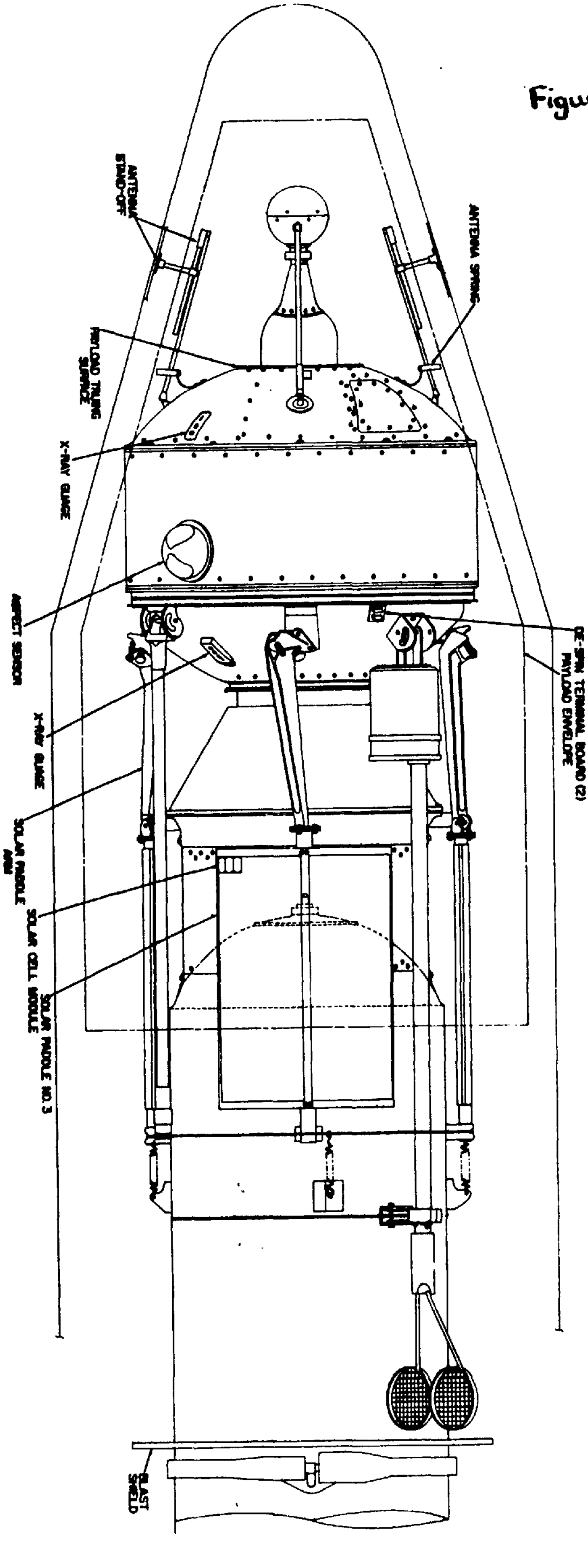
ANTENNA STAND-OFF
ANTENNA SPRING
PAYLOAD TRUING SURFACE
X-RAY GUAGE
ASPECT SENSOR
X-RAY GUAGE
SOLAR PADDLE ARM
SOLAR CELL MODULE
SOLAR PADDLE NO.3
DE-SPIN TERMINAL BOARD (2)
PAYLOAD ENVELOPE
BLAST SHIELD

2.3 Calibration.

A μ-meson scintillator telescope was used to measure the response of the cerenkov detector to singly-charged particles passing through the photomultiplier face and through the centre portion of the sphere. The discriminator was then set so that about 5 % or less of the doubly-charged particles passing normally through the glass face would be detected. The apparatus was temperature cycled to determine its over-all change of sensitivity with temperature and a thermistor was inserted in the discriminator to eliminate the first order term of this.

Calibration of the geiger counter consisted of first setting the maximum counting rate of the device to be about 100 per second, then its response to standard sources placed in certain set positions around the unit was noted. This laboratory calibration has been combined with an 'in flight' calibration to give the curve in figure 8. The 'in flight' calibration was derived from the ratio of geiger to cerenkov counting rates, making the assumption that the cerenkov counting rate was linearily proportional to the radiation intensity at the geiger counter. This assumption is reasonable so long as the energy spectrum of the particles remains approximately constant.

2.4 The 'In Flight' Performance of the Apparatus.

The original intention was to test the design of the cerenkov detector by mounting pre-prototype units on Black Knight rockets to be fired on ballistic trajectories at Woomera, Australia. However, owing to telemetry and vehicle malfunctions no useful data were obtained from

Figure 8

Geiger Counter Characteristic on July 9th. 1962.

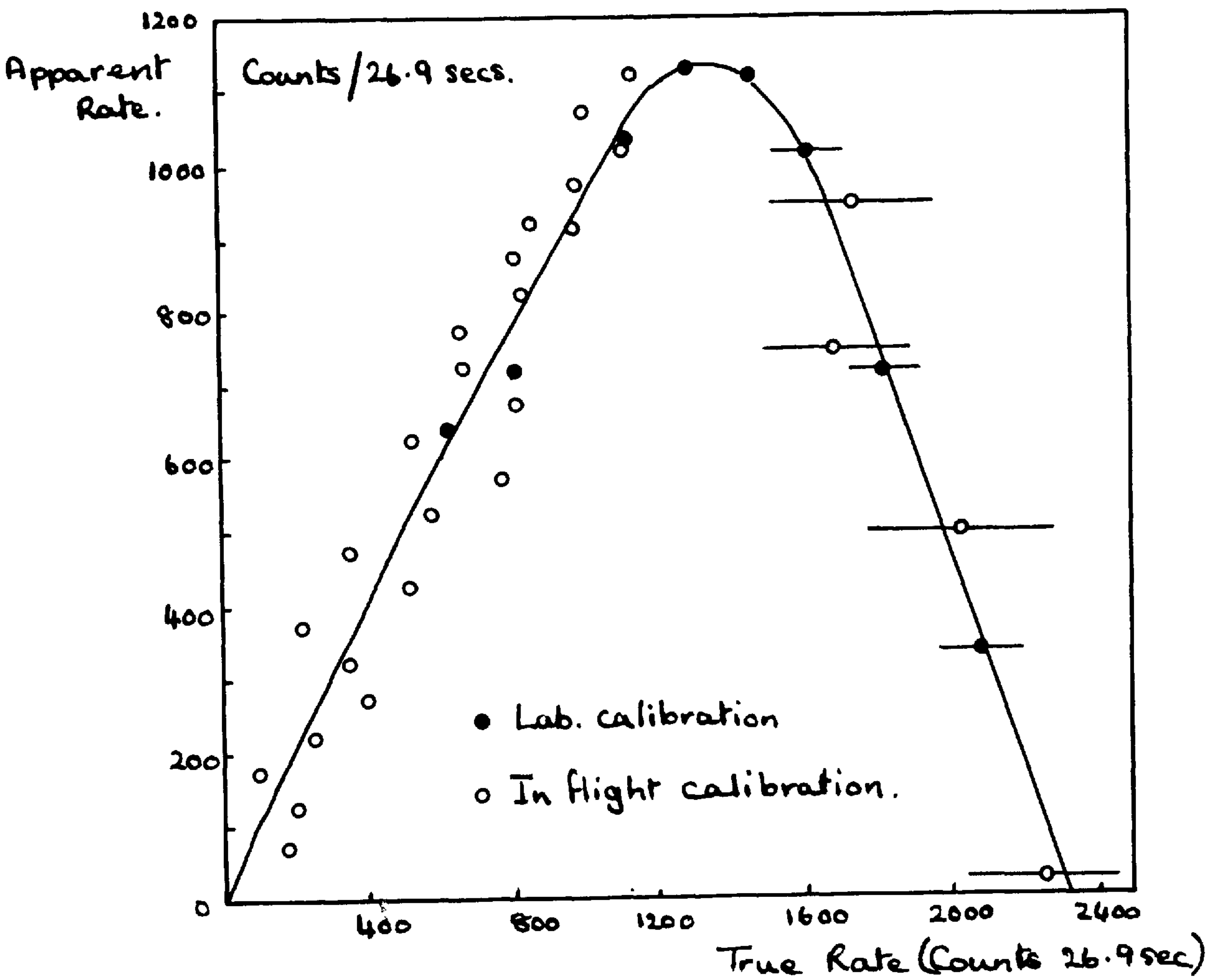

the first two flights. The third flight was made after the launching of the satellite and so the basic physics of the design were first tested by the satellite unit itself. There was therefore no possibility of making modifications to the satellite unit to correct any faults which might have been discovered on the proving flights. Fortunately the instrument behaved much as expected.

At 1800.00 hours UT. on the 26th of April 1962, Ariel I was launched into an orbit with an inclination of 54 degrees, a perigee of 395 km. and an apogee of 1215 km. The launch was not perfect as the following paragraphs will explain.

The spin rates of the satellite were monitored during injection so that any mishaps which occured at this crucial phase of the launch could be detected. This was done by placing an aspect sensor (designed by the University College team) on the dutchman connecting the spacecraft to the Bell X 248 third stage motor, and stationing a ship underneath the point of injection to pick up the directly telemetred signals from this.

The injection procedure should have been as follows: release of the 'stretch yoyo' to reduce the spin rate, release of the booms to allow their erection by contrifugal force, release of the solar paddles to allow their erection, and finally seperation of the spacecraft from the third stage motor. The booms and solar paddles of the spacecraft were strapped down to the body of the motor prior to their release. Analysis of the signals picked up by the ship gave spin rates that were only possible if the booms and paddles were released before the stretch yoyo, presumeably because of the burning of the straps or premature explosion of their catches caused by the heat of the burning solid fuel on the other side of the fiberglass motor case. Fortunately none of the booms or solar paddles appear to have been snapped off by the greater centrifugal forces and the final spin rate was very near the design figure. Whether the yoyo became entangled with any of the booms or paddles is a matter for speculation. However this haphazard erection did cause the attitude of the spacecraft after injection to be different from the intended one. This in turn upset the carefully calculated heat balance of the satellite, but the effects of this were not immediately obvious.

Soon after launch it was apparent that the cerenkov detector was slightly sensitive to inner belt particles. By operating a spare Cosmic Ray unit in the beam of the proton accelerator at Harwell, Berkshire, it was proved that this was due to scintillation light produced by protons travelling sideways through the glass face of the photomultiplier. Otherwise, the cerenkov unit behaved correctly until May 18th when the satellite moved into a 100 % sunlight orbit. The combination of the wrong attitude and the one hundred percent sunlight orbit probably raised the temperature of the Cosmic Ray unit above the design maximum of 60^{o}C. Migration of the photomultiplier photocathode was greatly speeded up, with a consequent decrease in gain. This phenomenon was also observed during pre-prototype tests above 60^{o}C. The effect of this is shown in figure 9 where the gain is represented by the average

Figure. 9

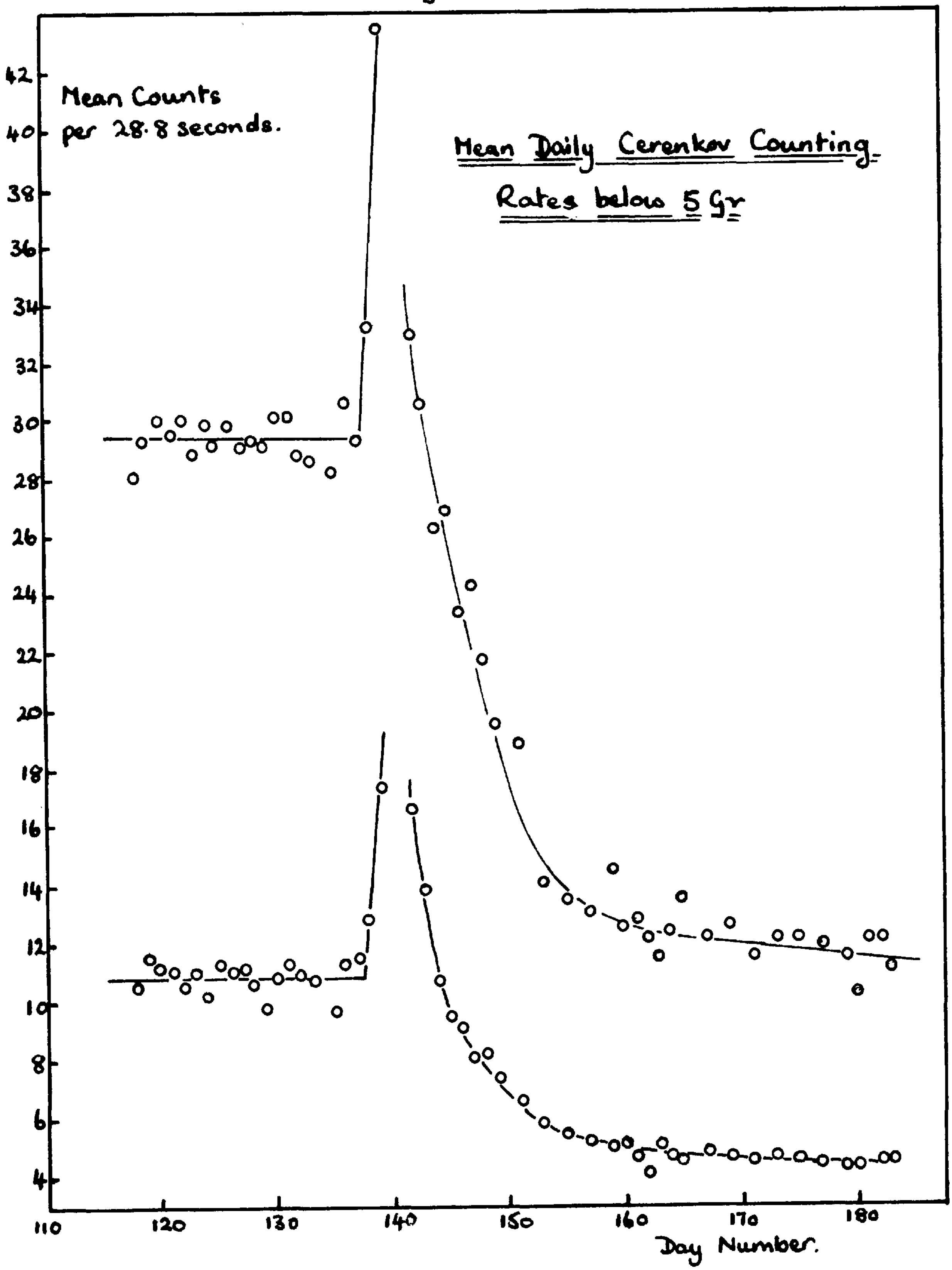
Mean Counts
per 28.8 seconds.
Mean Daily Cerenkov Counting
Rates below 5 Gr
42
40
38
36
34
32
30
28
26
24
22
20
18
16
14
12
10
8
6
4
110
120
130
140
150
160
170
180
Day Number.

daily counting rate of the cerenkov detector for regions where the cut-of rigidity is less than 5 Gv. The correlation of these curves with the temperature curve and the curve representing the percentage of sunlight per orbit is illustrated in figure 10. It should be noted that the temperatures shown are those of the centre of the satellite. The actual temperatures of the Cosmic Ray unit would be different from these, although the directions of the temperature changes would be the same. The gain changes were small after June 4th and the counter worked normally until 0900 hours UT. on July 9th when the 'Starfish' nuclear explosion took place. This decrease in gain has been used in the correction of the counting rates necessary because of the variation in the intensity of the cerenkov light for particles with velocities close to the relativistic limit in the perspex (section 4.2.1.).

A large amount of fission electrons were released by the Starfish nuclear explosion. Considerable numbers of these were able to penetrate the wall of the cerenkov detector. Although the light from them could not trigger the discriminator, in some regions the particle flux was large enough to be able to increase the photomultiplier dark current to such an extent that the high tension voltage supply was overloaded. Thus the gain was reduced occasionally and sometimes the counting rate became negligible. This effect was not observed before the Starfish explosion. It has been possible to use this phenomenon (see sections 5.2.1 to 5.2.5 inclusive) since estimates of the reduction in gain give some idea of the numbers of electrons present with sufficient energy to penetrate the detector. Assuming that the minimum energy electrons

Figure. 10

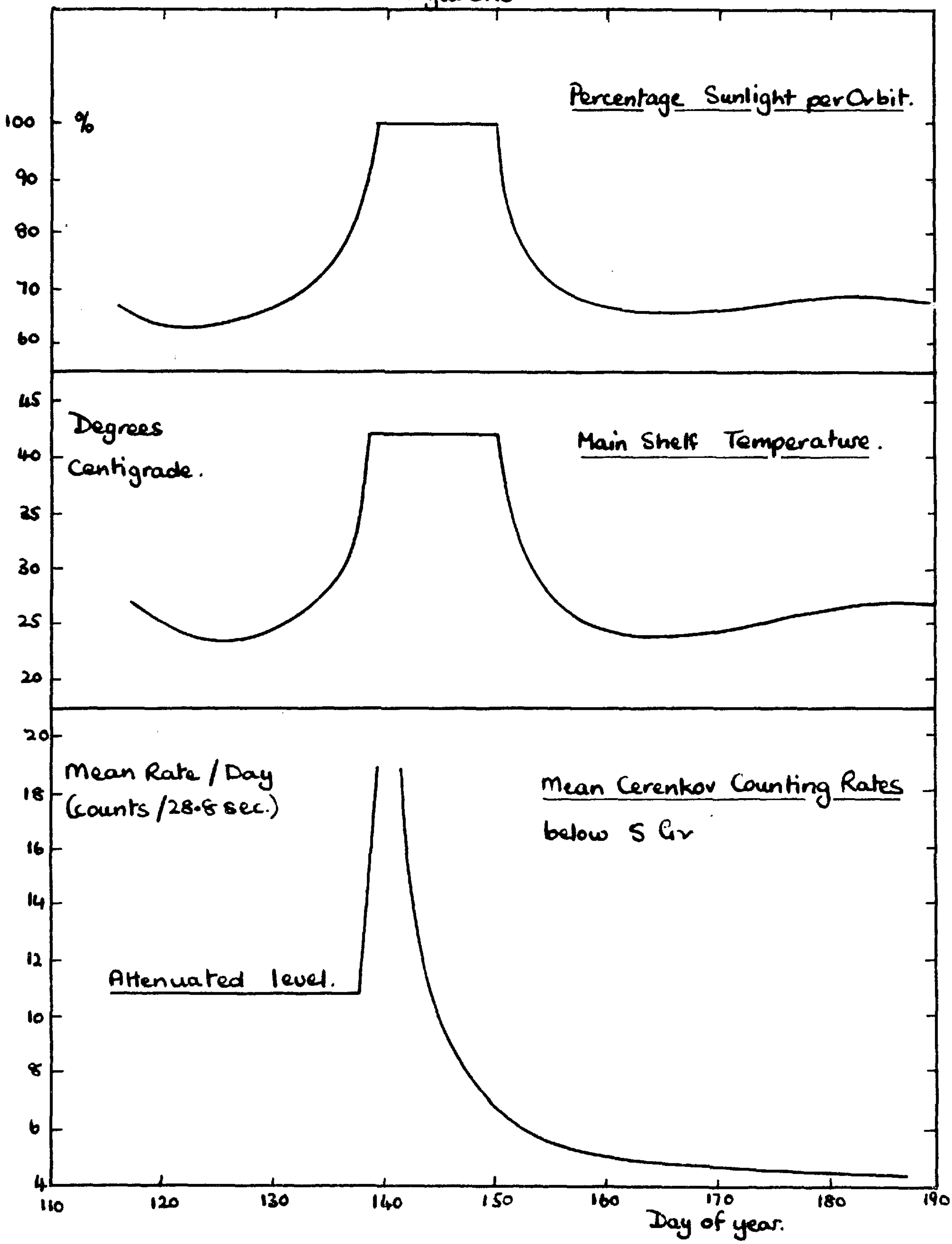
Percentage Sunlight per Orbit.
%
100
90
80
70
60
Degrees
Centigrade.
Main Shelf Temperature.
45
40
35
30
25
20
Mean Rate / Day
(counts / 28.8 sec.)
Mean Cerenkov Counting Rates
below 5 Gv
Attenuated level.
20
18
16
14
12
10
8
6
4
110
120
130
140
150
160
170
180
190
Day of year.

which have any effect are those which produce light in only one side of the sphere, then the shielding is effectively a minimum of;

0.4 gm/cm^2 aluminium,

0.1 gm/cm^2 eccofoam,

0.3 gm/cm^2 perspex.

This gives a total of 0.8 gm/cm^2 which has a 50 % probability of being penetrated by a 2.4 Mev electron. An estimate has been made in Appendix A of the numbers of electrons required to reduce the gain by an order of magnitude.

From April 26th until July 12th the geiger counter operated correctly, but with a slowly decreasing upper limit to the counting rate. After July 12th the operation of Ariel I became intermittent owing to the deterioration of the solar batteries, and as a result the satellite tape recorder failed in mid-August. At the beginning of September the geiger counter ceased to function, presumeably due to a transistor failure; the cerenkov detector ceased to operate in mid-December.

CHAPTER 3

THE ENVIRONMENTAL TESTING

In addition to the design considerations set by the physics of the experiment, several severe practical requirements were necessary for apparatus which was to be flown in a satellite. The unit had to be economical in its use of power, it had to be light, compact, capable of operating for a year without failure, and finally it had to be capable of withstanding the prototype satellite environmental tests without damage. These environmental tests were designed to show whether the satellite was capable of surviving the pre-launch, launch and orbiting strains. Any of the prototype parts which failed any of these tests were modified until they could pass them, and these modifications were incorporated in the flight units. The tests were carried out at the Goddard Space Flight Center, Maryland. The procedure and specifications are shown below and are the normal ones for apparatus to be launched by a multistage rocket from Cape Canaveral, the last stage being a Bell X 248 solid fuel motor.

3.1 Integration.

The prototype sub-assemblies were first mechanically integrated to eliminate fitting problems. They were then electrically integrated to ensure electrical compatability between units and absence of interference. The electrical integration included temperature cycling between

-15°C and 50°C to search for design problems that may have occurred at temperatures other than ambient.

3.2 Spin and Balance Test.

The spacecraft was balanced both statically and dynamically about its spin axis. It was then operated whilst spinning for:

1 minute at 225 rpm,

30 minutes at 150 rpm.

3.3 Temperature Tests.

These tests were as follows:

1. The payload (non-operating) was subjected to -30°C for 6 hours.
2. The payload (non-operating) was subjected to 60°C for 6 hours.
3. The temperature was stabilised at 5°C, the payload was then switched on and tested.
4. The temperature was stabilised at -10°C, the payload was then switched on and tested.
5. The temperature was stabilised at 50°C, the payload was then switched on and tested.

Between each of the above tests the payload was tested at room temperature.

3.4 Humidity Test.

The payload was exposed to 95 % relative humidity at a temperature of 30°C for 24 hours and was switched on and tested whilst still under those conditions. It was then allowed to dry out whilst the performance was carefully monitored. Finally the spacecraft was tested at room temperature.

This test was intended to check whether permanent damage would be done to the satellite if it was stored under those conditions at any time.

3.5 Vibration Tests.

These were carried out in the following order:

Thrust Axis Test (tall fixture).

1. 10 - 50 cps at 2.3g

   50 - 250 cps at 21 g

2. Random, 20 - 250 cps at 11.5 g (0.07 g^2/cps) for 4 minutes.

Thrust Axis Test (short fixture).

3. 250 - 500 cps at 10.7 g

   500 - 2000 cps at 21 g

   2000 - 3000 cps at 54 g

4. Random, 250 - 2000 cps at 11.5 g (0.07 g^2/cps) for 4 minutes.

Transverse Axis Test (tall fixture) X - X direction.

5. 10 - 50 cps at 0.9 g, also 50 - 150 cps at 2.1 g.

6. Random, 20 - 150 cps at 11.5 g (0.07 g^2/cps) for 4 minutes.

7. Resonance dwell, $\frac{1}{2}$ minute sweep, 550 - 650 cps at 4.2 g.

Transverse Axis Test, Y - Y direction (tall fixture).

8. 10 - 50 cps at 0.9 g

   50 - 150 cps at 2.1 g

9. Random, 20 - 150 cps at 11.5 g (0.07 g^2/cps) for 4 minutes.

10. Resonance dwell, ½ minute sweep, 550 - 650 cps at 4.2 g

Transverse Axis Test, Y - Y direction (short fixture).

11. 150 - 500 cps at 2.1 g

    500 - 2000 cps at 4.2 g

12. Random, 150 - 2000 cps at 11.5 g (0.07 g^2/cps) for 4 minutes.

13. Resonance dwell, ½ minute sweep, 550 - 650 cps at 4.2 g.

Transverse Axis Test, X - X direction (short fixture).

14. 150 - 500 cps at 2.1 g

    500 - 2000 cps at 4.2 g

15. Random, 150 - 2000 cps at 11.5 g (0.07 g^2/cps) for 4 minutes.

16. Resonance dwell, ½ minute sweep, 550 - 650 cps at 4.2 g.

All frequency sweeps were logarithmic.

All frequency sweeps except the resonance dwells were at the rate of two octaves per minute

The tall fixture was used to simulate the third stage rocket motor and allow the various booms and paddles to be attached in their folded positions.

The short fixture was used at higher frequencies because of the attenuation in the tall fixture at these frequencies.

The acceleration values shown here were those applied by the machines at the base of the fixtures.

3.6 Acceleration Test

The space craft was subjected to a steady thrust axis acceleration of 25 g for 5 minutes.

3.7 Shock Test.

The spacecraft was subjected to a half sine wave pulse of 30 g peak amplitude and 11 milliseconds duration. This was intended to simulate the shock due to the lighting of the booster.

3.8 Thermal Vacuum Tests.

The programme for these was as follows:

Vacuum operation.

The spacecraft was operated as pressure in the test chamber was reduced to 3×10^{-6} mm Hg, the limit of the capability of the system. This operation took about 12 hours for completion.

Cold Vacuum Soak.

The chamber was evacuated, stabilised at a temperature of -10^{o}C, then the spacecraft was switched on and operated at this temperature for 7 days, a complete check of the system being performed every 12 hours.

Hot Vacuum Soak.

The chamber was evacuated, stabilised at a temperature of 55^{o}C, then the spacecraft was switched on and operated at this temperature for 3 days, complete tests being performed every 12 hours.

The spacecraft was tested at ambient temperature and pressure before and after each of the above operations.

3.9 Solar Aspect Test.

This consisted of operating the spacecraft in vacuum, illuminated by a ring of tungsten filament heat lamps with the walls of the chamber maintained at a temperature of -60°C. The lamps were first operated in a ring representing an angle of 30 degrees between the forward spin axis and the satellite-sun line, then in a ring representing an angle of 135 degrees between the same two lines. The rings of lamps were intended to simulate the sun as seen from a revolving satellite. The temperatures of the various units were monitored during these tests. This was a fairly crude attempt to produce the temperature gradients that would actually be experienced in the satellite during operation in orbit.

3.10 Summary of the Prototype Tests.

Owing to the amount of trouble that is generally experienced during these tests, only very rough estimates can be made of the time required to complete them. The tests on Ariel I lasted six months. A list of the problems experienced in these six months is given below.

Temperature and Humidity Tests.

Sub-assembly design problems	1
Component failures (excluding connectors)	1

Wiring harness failures (including connectors)	0
Faulty assembly failures	3
Test equipment failures	4
Total:	9

Vibration, Acceleration and Shock Tests.

Sub-assembly design problems	5
Component failures (excluding connectors)	6
Wiring harness failures (including connectors)	5
Faulty assembly failures	1
Test equipment failures	1
Total:	18

Thermal Vacuum and Aspect Tests.

Sub-assembly design problems	8
Component failures (excluding connectors)	13
Wiring harness failures (including connectors)	3+
Faulty assembly failures	6
Test equipment failures	7
Total:	37

Components which failed due to design problems have not been included in these lists. Note the large number of component failures which occurred during the thermal vacuum tests. Owing to the relatively large amount of trouble caused by the prototype wiring harness, this was redesigned for the flight units.

3.11 Environmental Testing of the Flight Units.

These tests were not so severe as those carried out on the prototype, nor were the humidity or solar aspect tests made.

The temperature test consisted of 24 hours at 35°C, and another 24 hours at -10°C.

The same frequency ranges were used as in the prototype vibration tests, but the accelerations were reduced to 2/3 of the prototype levels.

The hot and cold thermal vacuum tests were limited to two days each, the temperatures being 35°C and -10°C respectively.

The estimated time for the environmental testing of the flight units was built up as shown below. Time for trouble shooting has been allowed in these figures.

Component collection	1 day
Spacecraft assembly and turn-on	3 days
Spacecraft testing and initial removal of troubles	4 days
Calibration of analog experiments	5 days
Setting up for temperature test	3 days
Temperature test	1 day
Preperation for vibration ('loctiting' etc.)	3 days
Initial balancing of the payload	4 days
Vibration tests	5 days
Setting up for thermal vacuum test	1 day
Thermal vacuum test	9 days
Antennae pattern measurement	5 days
Final calibration of analog experiments	6 days

Final balancing of the payload	6 days
Total:	56 days

In practice, difficulties were experienced with each payload which added on about half as many days again to the total given above.

After the vibration tests only minor modifications could be made to the spacecraft, for dismantling and re-assembly would have made re-vibration necessary. This was undesireable, since each vibration test increases the chance of the tested structure failing due to fatigue.

The flight units were transferred to Cape Canaveral by road when they were completely ready. There they were tested to ensure they were still in perfect operating condition. Flight unit I was attached to the third stage motor, then the complete assembly was spun and balanced to align the centres of gravity and inertia with the spin axis. This operation required five days. The third stage assembly was then hoisted up the launching gantry and placed on top of the second stage. In order that the vehicle preparations could be made in time, the latest this could be done was 4 days before launch. A complete practice count-down was performed the day before launch.

The first launch attempt was abortive owing to a faulty second stage which started to show signs of trouble at T -6 minutes (April 10th). The satellite was not operated between this date and the next count-down practice which was performed on April 25th.

The satellite was successfully launched on April 26th, 1962.

CHAPTER 4

THE ENERGY SPECTRUM OF THE PRIMARY COSMIC RADIATION

The information from the cerenkov detector in the satellite was received in the form of store samples, ie. the number of counts contained in the store at intervals of 30.72 seconds. These numbers have been differenced to give counting rates, and were correlated with the real time of the sample, the geographic position of the satellite, Quenby-Wenk vertical threshold rigidities, the scalar magnitude of the magnetic field and L values. This work was done with the aid of an IBM 7090 computer. The important quantities in the following discussion in addition to the counting rates, are the altitudes and the Quenby-Wenk figures.

4.1 Data Selection.

This first analysis was carried out on the results for about 600 orbits which were available for the period between the 26th April and the 9th July, 1962. Twenty-four percent of those data were unuseable because they were collected between May 18th and June 4th during which time the sensitivity of the cerenkov counter was changing.

By using the geiger counter results, cerenkov data collected in the inner belt were picked out and rejected because of the sensitivity of the latter counter to the inner radiation belt protons. The maximum geiger counting rates which may be expected from the cosmic radiation are shown by the curve in figure 11. Counting rates greater than these

Figure. 11

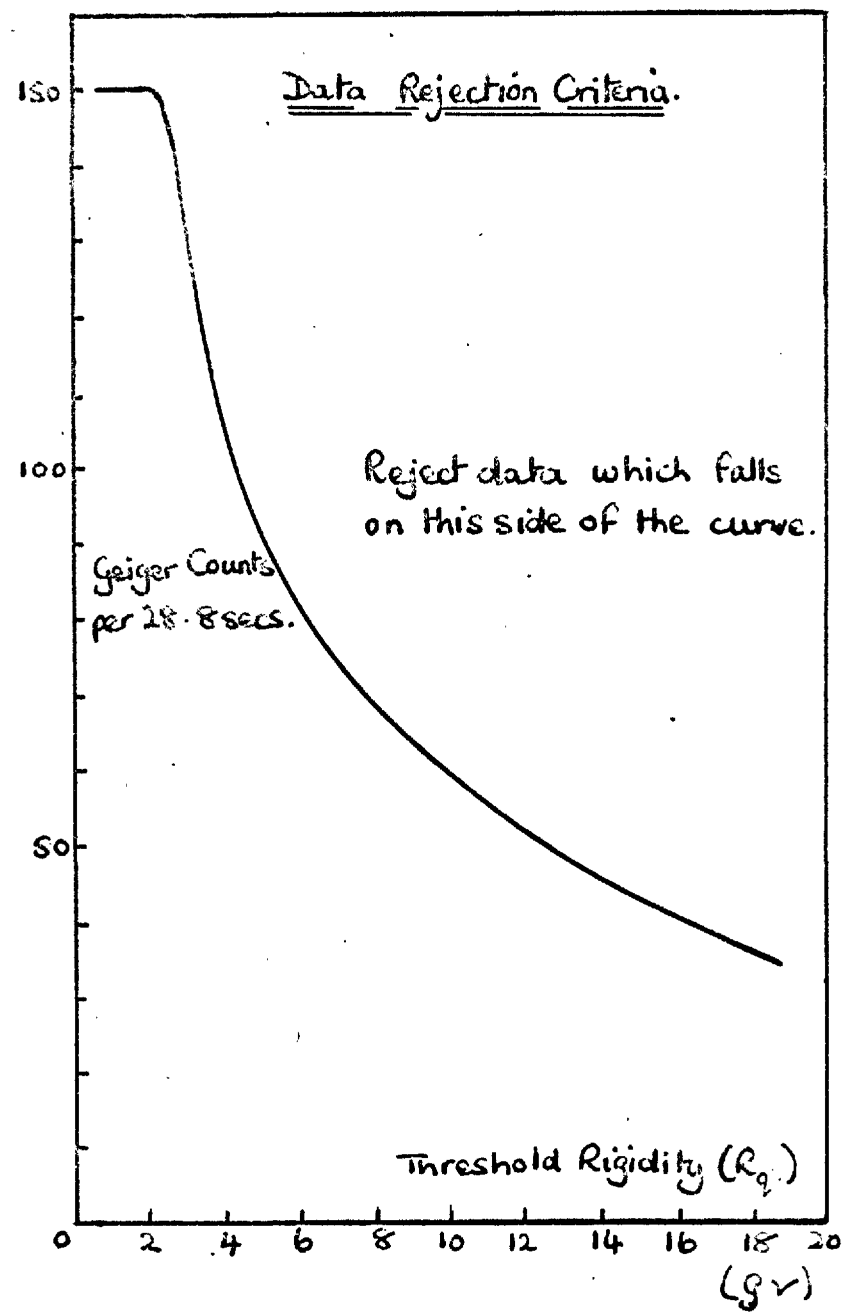
Data Rejection Criteria.
150
100
50
0
Reject data which falls on this side of the curve.
Geiger Counts per 28·8 secs.
Threshold Rigidity (R_q)
2 4 6 8 10 12 14 16 18 20
(gv)

indicate that the satellite was passing through a region containing trapped particles. From figure 11, it can be seen that the absolute maximum geiger counting rate which will be tolerated without rejection of the data is 150 counts per interval. In figure 12 is shown the area occupied by cosmic ray counts in a geiger-cerenkov ratio diagram and also part of the curve on which the points for the counting rates lie when the instrument is passing through the inner belt (cosmic ray counts have been subtracted from the data to make this curve). It should be clear that even if all 150 geiger counts per interval are due to radiation belt particles, then the contaminated cerenkov rate cannot exceed 1.5 counts per interval, which is small when compared with the average cosmic ray counting rate. In practice no radiation belt peaks were observed in the geiger counting rates in regions where the threshold rigidity is less than 5 Gv, so this means the geiger counting rate caused by radiation belt particles could not have exceeded 90 counts per interval. This places an even tighter restriction on the possible contamination of the cerenkov counting rates. Thus this method of detecting trapping regions is sensitive to radiation intensities well below those at which the trapped particle contribution to the cerenkov counting rates becomes appreciable.

For the time during which data were collected, the attitude of the satellite was such that the shadowing effect of the Earth on the cerenkov detector was greater at increased altitudes (see section 4.2.3). The data fall naturally into two homogeneous groups; that collected by the satellite at altitudes greater than 800 km where the average

Figure. 12

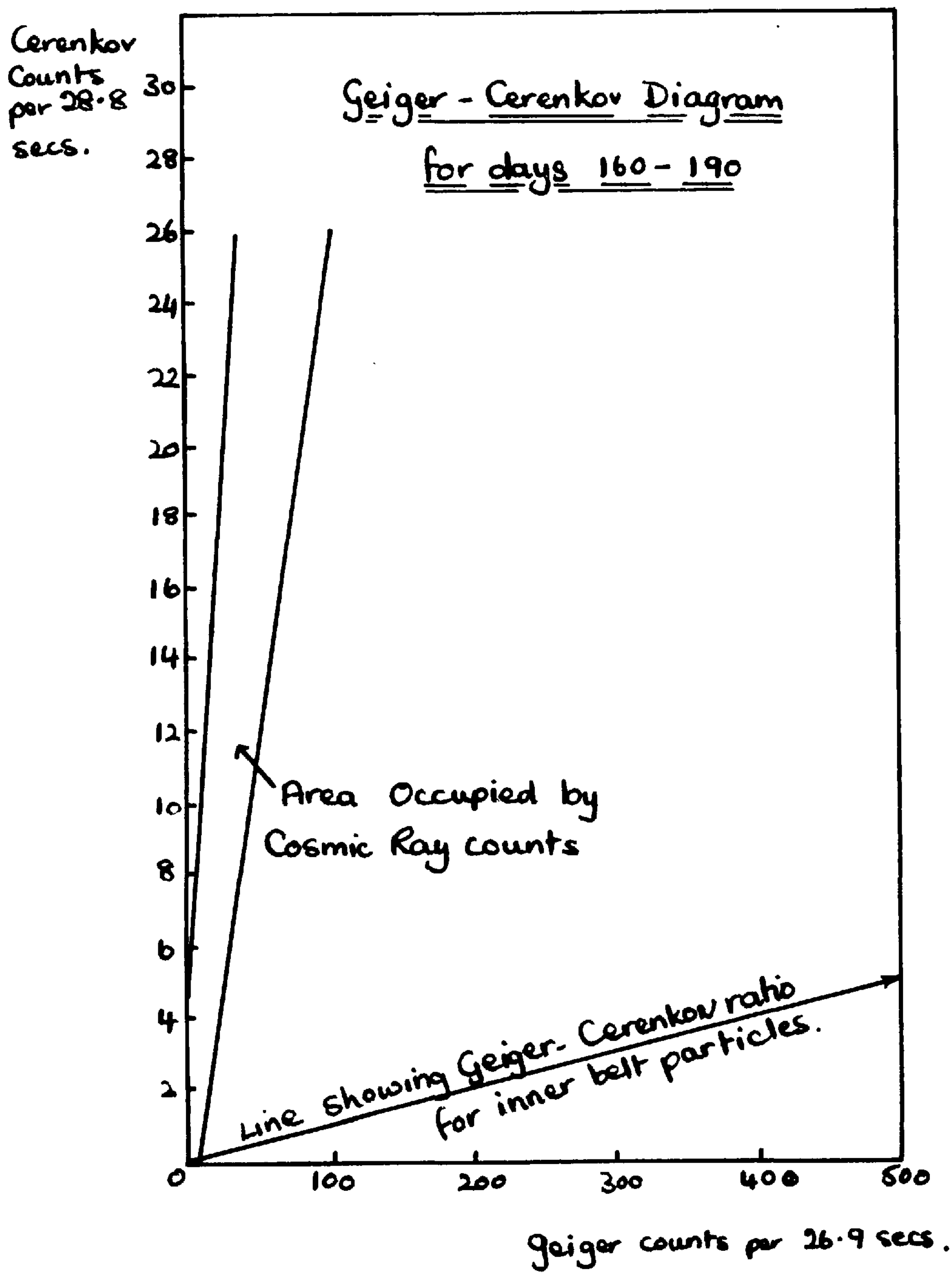
Cerenkov Counts per 28·8 secs.
Geiger - Cerenkov Diagram for days 160 - 190
30
28
26
24
22
20
18
16
14
12
10
8
6
4
2
0
100
200
300
400
500
Area Occupied by Cosmic Ray counts
Line showing Geiger- Cerenkov ratio for inner belt particles.
Geiger counts per 26·9 secs.

Earth's shadowing effect is large, and that collected at altitudes less than 800 km where the average Earth's shadowing effect is relatively small. Both groups contain results which extend over the entire range of the threshold rigidities scanned by the satellite. Only the group containing data obtained below 800 km has been used in this preliminary analysis in order to keep the Earth's shadowing effect to a minimum and because of the greater uncertainty in the threshold rigidities as the Quenby-Wenk figures are extended to greater altitudes. This restriction of the data also minimises the altitude effect on the counting rates and reduced the work necessary to remove the Van Allen radiation contribution to the counting rate. The percentage of this contribution was larger above 800 km.

4.2 Errors and Data Corrections.

The chosen group of results was used to plot the curves in figure 13. The open circles represent the mean counting rates between April 26th and May 18th, the filled circles represent the mean counting rates between June 4th and July 9th. It so happened that the gain of the unattenuated level after the change in sensitivity was nearly equal to the gain of the attenuated level before the change. By making use of this it is possible to draw the gain versus counting rate curves as in figure 14. The corrections considered for these results are listed below in the order of their importance.

4.2.1 The Fall-Off in Cerenkov Light for Slow Particles.

From Frank and Tamm's classical theory of the cerenkov radiation

Figure. 13

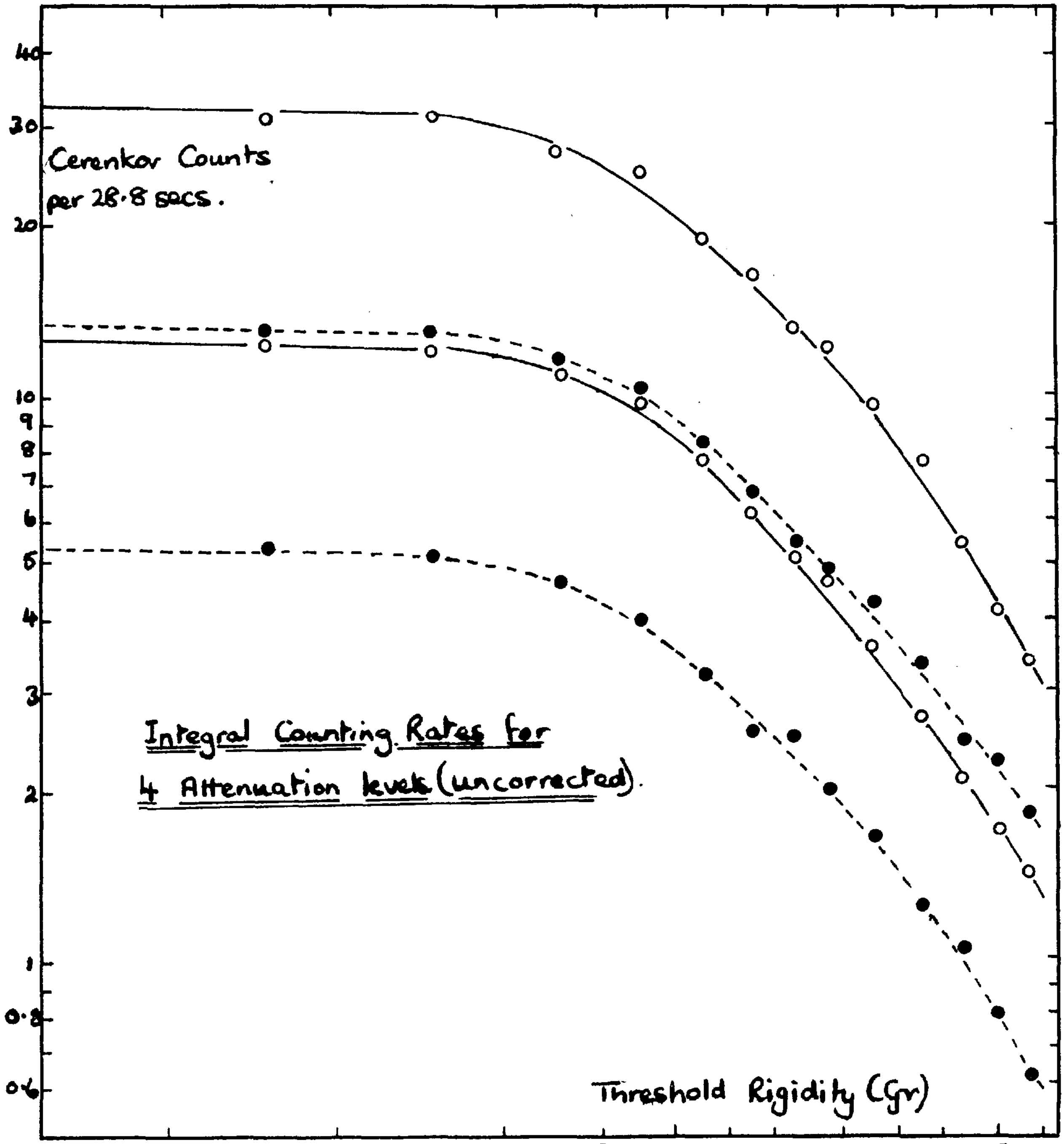
Cerenkov Counts
per 28·8 secs.
Integral Counting Rates for
4 Attenuation levels (uncorrected).
Threshold Rigidity (Gv)
40
30
20
10
9
8
7
6
5
4
3
2
1
0·8
0·6
0·3
0·6
1
2
3
4
5
6
8
10
12
15
18

Figure. 14

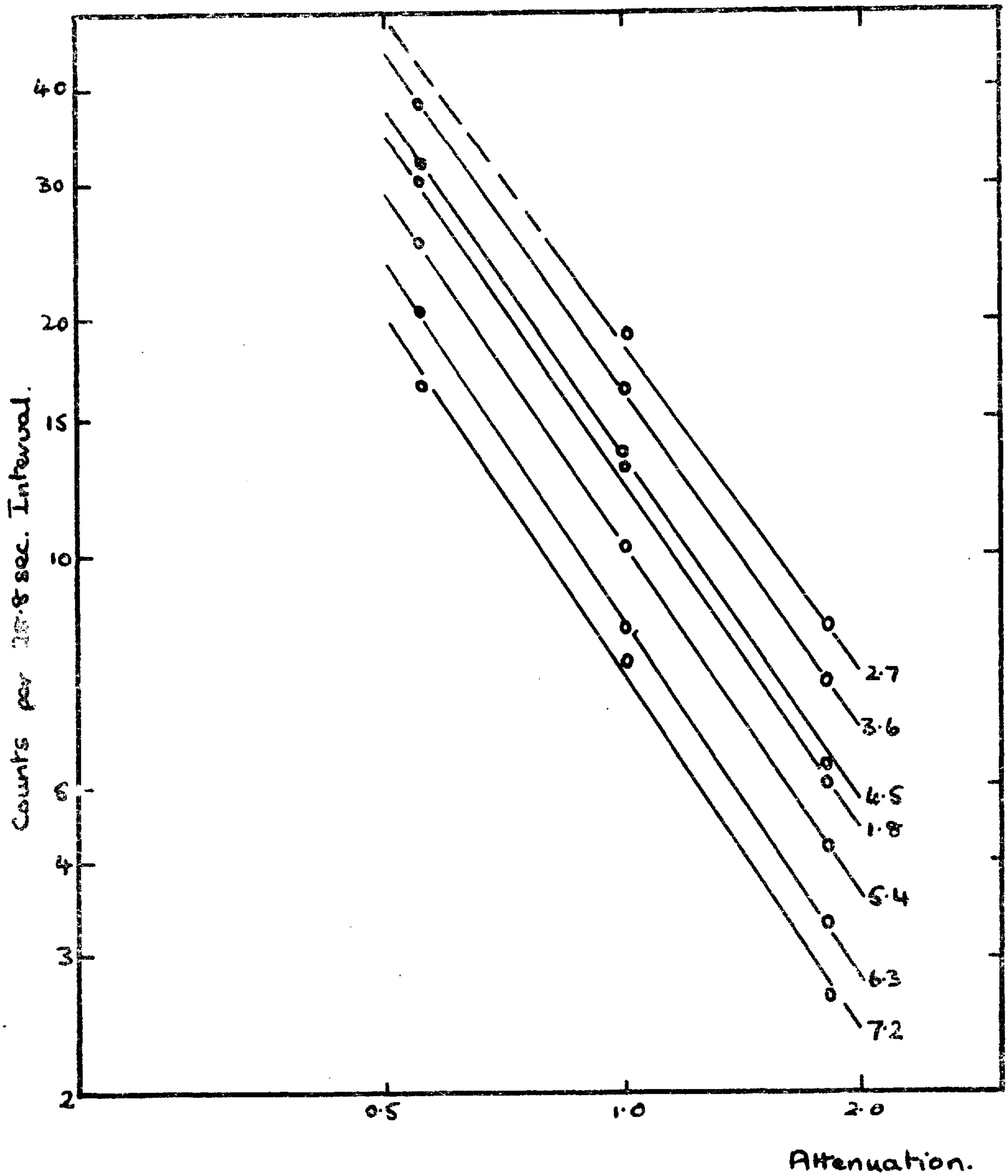

Counts per ·8 sec. Interval.
40
30
20
15
10
6
4
3
2
0·5
1·0
2·0
Attenuation.
2·7
3·6
4·5
1·8
5·4
6·3
7·2

(1937):

$$N = 2\pi\alpha d\left(\frac{1}{\lambda_1} - \frac{1}{\lambda_2}\right) \quad (1 - 1/\beta^2 n^2)$$

where N = number of photons yielded in the spectral range λ_1 to λ_2,

α = fine structure constant = $e^2/$ hc = 1/137,

β = v/c where v is the particle velocity,

n = refractive index of the substance traversed by the particle,

d = path length of the particle.

From this it can be seen that N is proportional to $(1 - 1/\beta^2 n^2)$. Thus particles near to the cerenkov limit of the perspex will produce less light than the faster ones, for which $\beta \rightarrow 1$. Since the velocity of a particle increases monotonically with its rigidity, this means that the gain of the detector is effectively less for particles of lower rigidity. Obviously this will introduce a systematic error which could lead to an underestimation of the counting rates at low rigidities. This error may be eliminated if it is possible to find the value of the factor $(1 - 1/n^2)/(1 - 1/\beta^2 n^2)$ by which the gain must be multiplied to bring it to the value for which $\beta \rightarrow 1$, and from the counting rate versus gain curves, obtain the equivalent counting rate for the corrected gain. To do this we must know β for the various rigidities.

Now the rigidity of a relativistic particle is defined by the expression:

$$R = mc^2\beta/Ze(1 - \beta^2)^{\frac{1}{2}},$$

where m is the rest mass of the particle and Ze is its charge. For primary cosmic rays other than protons, the specific charges are close to two, therefore the term mc^2/Ze is approximately constant and equal to 1.9 Gv. Thus the value of β for each rigidity may be found from this expression and the gain factor calculated. In figure 14 the counting rate - gain curves are shown for rigidities which have values of $(1 - 1/n^2)/(1 - 1/n^2\beta^2)$ greater than 1.05. The corrected counting rates may be read directly from these curves except for rigidities of 1.8 Gv and less for which the correction factors were equal to 7 or greater, and so are outside the range of the curves.

When this correction is completed, the probable error in the counting rate depends on the deviation of the actual counting rate - gain curves from the straight lines which have been fitted to the available experimental points. This is hard to estimate, but the error is certainly less than the errors produced by the effects which are discussed in the following section.

4.2.2 Threshold Rigidity Corrections

The Quenby-Wenk threshold rigidities are calculated for vertically incident particles at sea level. The satellite results which were used were obtained at a mean height of 600 km, using a detector with a wide solid angle of acceptance. At low lattitudes the effective threshold rigidities for a wide angle detotor must be different to the vertical threshold rigidities since there is a large variation in threshold rigidity with zenith angle. At higher lattitudes the vertical thresholds will be closer to the effective threshold rigidities for the detector since according to Stormer theory this east-west effect is not so marked; when the vertical threshold rigidity falls to zero the effective threshold for our detector must be the same (Lemaitre and Vallarta, 1933).

Now the effective threshold rigidity of the detector may be defined as the rigidity value at that sharp cut-off in the primary cosmic ray spectrum which would produce the same counting rate in the detector as that actually observed. When the blocking of the sensitive solid angle of the detector by the earth is a minimum, particles will be received from a solid angle of roughly 2π. This is almost the same situation as that of an observer on the Earth's surface, assuming there is no atmosphere. Thus if we can discover the effective threshold for the observer on the Earth's surface, it is only necessary to adjust this to 600 km. above sea level to find the effective threshold for our detector.

In calculating this effective threshold rigidity, the allowed and forbidden directions of the particles incident on the Earth must be taken into account. It is found that particles can arrive from a cone of angles, outside of which all directions are forbidden. This is known as the Stormer cone. The Stormer cone may be divided into three sections, the main cone, the shadow cone and the penumbra. Particles can arrive from all directions inside the main cone, they cannot arrive from any direction inside the shadow cone because their curving trajectories intersect the Earth's surface before they reach the observer. The penumbra is a region where some directions are allowed and some are forbidden. The calculation of the Stormer cone is fairly simple, the calculation of the main, shadow and penumbral cones is complex. Since a large error arises in adjusting the effective threshold rigidity to the satellite altitude, it is not worthwhile to calculate the effective thresholds accurately for the Earth's surface at this stage. As a first approximation, therefore, the effective threshold at the equator may be calculated and those for other geomagnetic latitudes obtained by using the expression:

$$R_{eff\ (sea\ level)} = R_q + R_q^2(R_1 - R_2)/R_2^2 .$$

$R_{eff\ (sea\ level)}$ = the effective threshold rigidity at sea level,

R_q = the Quenby-Wenk threshold rigidity,

R_1 = the effective threshold rigidity at the equator,

R_2 = the Quenby-Wenk threshold rigidity at the equator.

This expression gives the correction from vertical to effective threshold rigidity as a second order term, ensuring that the correction falls off quickly as we move away from the equator. This is necessary since the difference between the rigidities of the highest energy particle and the lowest energy particle to reach the observer falls quickly with increasing latitude, and in some way this difference must be proportional to the correction factor.

At the equator the penumbral effect is negligible. Thus the Stormer cone consists of only the main and shadow cones. Kasper (1958) has shown that the shadow cones are small. We may make, therefore, a further approximation and say that all directions inside the Stormer cone are allowed. The rigidity threshold for any direction in the sky is then given by Stormer's expression:

$$R = ZeM \cos^4\lambda/cr^2(1 + \sqrt{1 - \cos\alpha \cos\beta \cos^3\lambda})^2$$

where M = the dipole moment,

Ze = the charge of the particle,

r = the radial distance from the dipole centre,

eM/cr^2 = 59.6 Gv for the Earth's surface,

λ = lattitude,

α = azimuthal angle,

β = zenith angle.

This equation treats the Earth as a dipole and takes no account of the eccentricity of the real Earth's dipole field or of the magnetic anomalies.

For the equator $\lambda = 0$, and the curve shown in figure 15 may be obtained by integrating the allowed directions for the various particle rigidities. The relative intensities are given as percentages of the intensities to be found at infinity (using Liouville's theorem). The total primary cosmic ray intensity seen by an observer at the equator on the Earth's surface can be found by multiplying this curve by the differential primary rigidity spectrum. The effective equatorial threshold rigidity at sea level is then simply the rigidity which corresponds to this intensity in the integral primary cosmic ray spectrum. The last two steps were taken by graphical means, assuming the integral primary spectrum to have an exponent of 1.5 (McDonald and Webber, 1959). This gave an effective threshold rigidity of 15.9 Gv at sea level.

This number is mainly sensitive to the slope of the curve in figure

Figure. 15

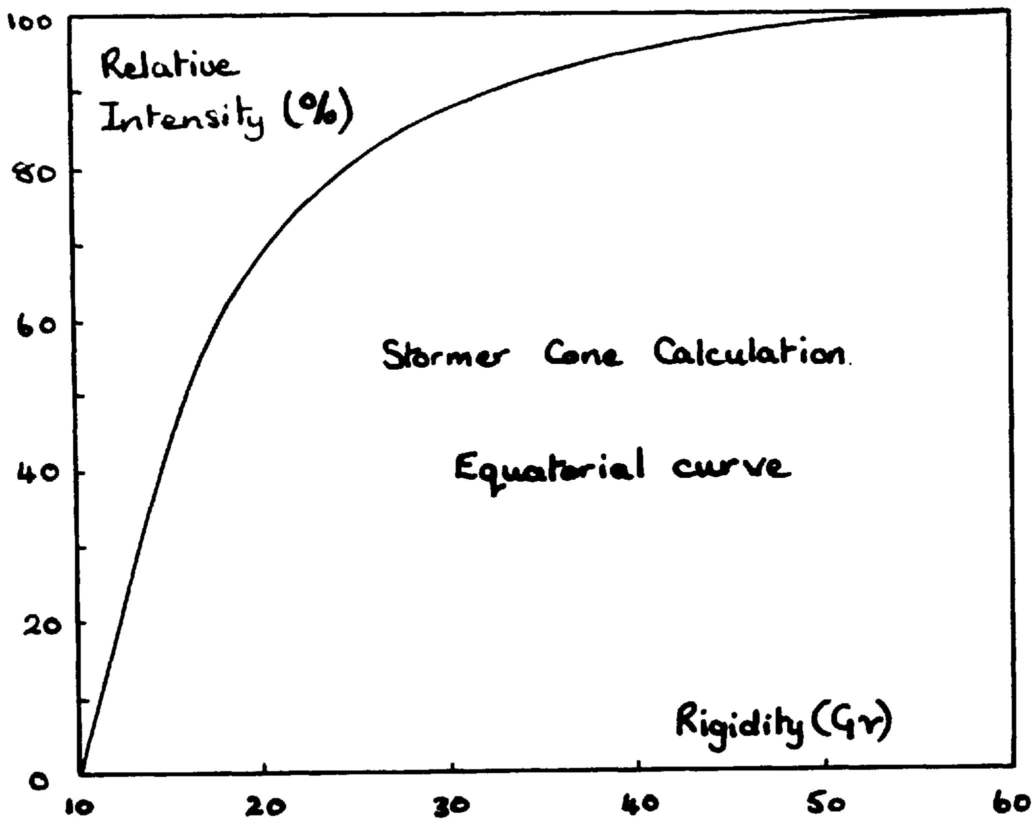

100
80
60
40
20
0
Relative
Intensity (%)
Stormer Cone Calculation.
Equatorial curve
Rigidity (Gv)
10
20
30
40
50
60

15 for threshold rigidities below 30 Gv. It is insensitive to the shape at higher rigidities where the Earth's shadow cone has most effect. It is also insensitive to the slope which is assumed for the primary cosmic ray spectrum. For these reasons, this number is probably a fairly accurate estimate of the mean, equatorial, effective threshold rigidity.

From the Stormer equation shown above, the vertical (or Quenby-Wenk) threshold rigidity at the equator is 14.9 Gv. So, by substitution we have:

$$R_{eff}\ (\text{sea level}) = R_q + 4.5 \times 10^{-3} R_q^{\,2}.$$

The results obtained by the satellite above 800 km can be used to correct these effective threshold rigidities to a mean height of 600km above sea level. The uncorrected data from above 800 km have been averaged to obtain curves similar to those shown in figure 13. There are differences between these two sets of curves which must be due to the different circumstances in which the two sets of data were collected, in other words the difference in altitudes and in the Earth's shadowing effect. The altitude has an effect (I) because of the change in effective threshold rigidity as the satellite moves away from the Earth and (II) because of the smaller solid angle subtended by the Earth at the detector for greater altitudes. The latter causes the counting rate to increase since particles can arrive from more directions. This effect is discussed in section 4.2.4.

Since the Earth shadowing effect (see section 4.2.3) and altitude effect (II) alter the counting rate by relatively simple geometrical means, then to a first approximation the differences they introduce between the two sets of curves are eliminated if the counting rates are normalised to make the plateaux of the curves co-incide. The result of this operation is shown in figure 16. The remaining difference between the two sets of curves must now be due mainly to altitude effect (I) which indirectly changes the counting rate by changing the effective threshold rigidity. The two sets of curves in figure 16 are the same shape within the limits of the errors, but the threshold rigidity values of the highor altitude curve are 25 % higher than those for the lower altitude curve. Thus in moving from a mean altitude of 600 km to a mean altitude of 1000 km, the true effective threshold rigidities are decreased by a factor of 100/ 125 = 0.8.

Assume the threshold rigidity (R) is proportional to $1/r^x$, where x is unknown, then:

$$R_{600} / R_{1000} = 125/100 = (7370/6970)^x \ .$$

(The mean diameter of the Earth is taken to be equal to 6370 km.)

$$\text{Thus } x = 4$$

$$\text{and } R_{600}/R_{\text{sea level}} = (6370/6970)^4$$

$$R_{600} = 0.7\ R_{\text{sea level}}$$

Stormer theory predicts that R will be proportional to $1/r^2$, in which case the correction factor would have been 0.84 instead of 0.7. The difference between the Stormer prediction and the experimental results is almost certainly caused by the increasing transparancy of the penumbra at greater altitudes. The works of Hutner, Vallarta (1948) , and Koenig permit some qualitative remarks about the penumbra, and it would seem that above 35 degrees of geomagnetic latitude the penumbra

Figure. 16

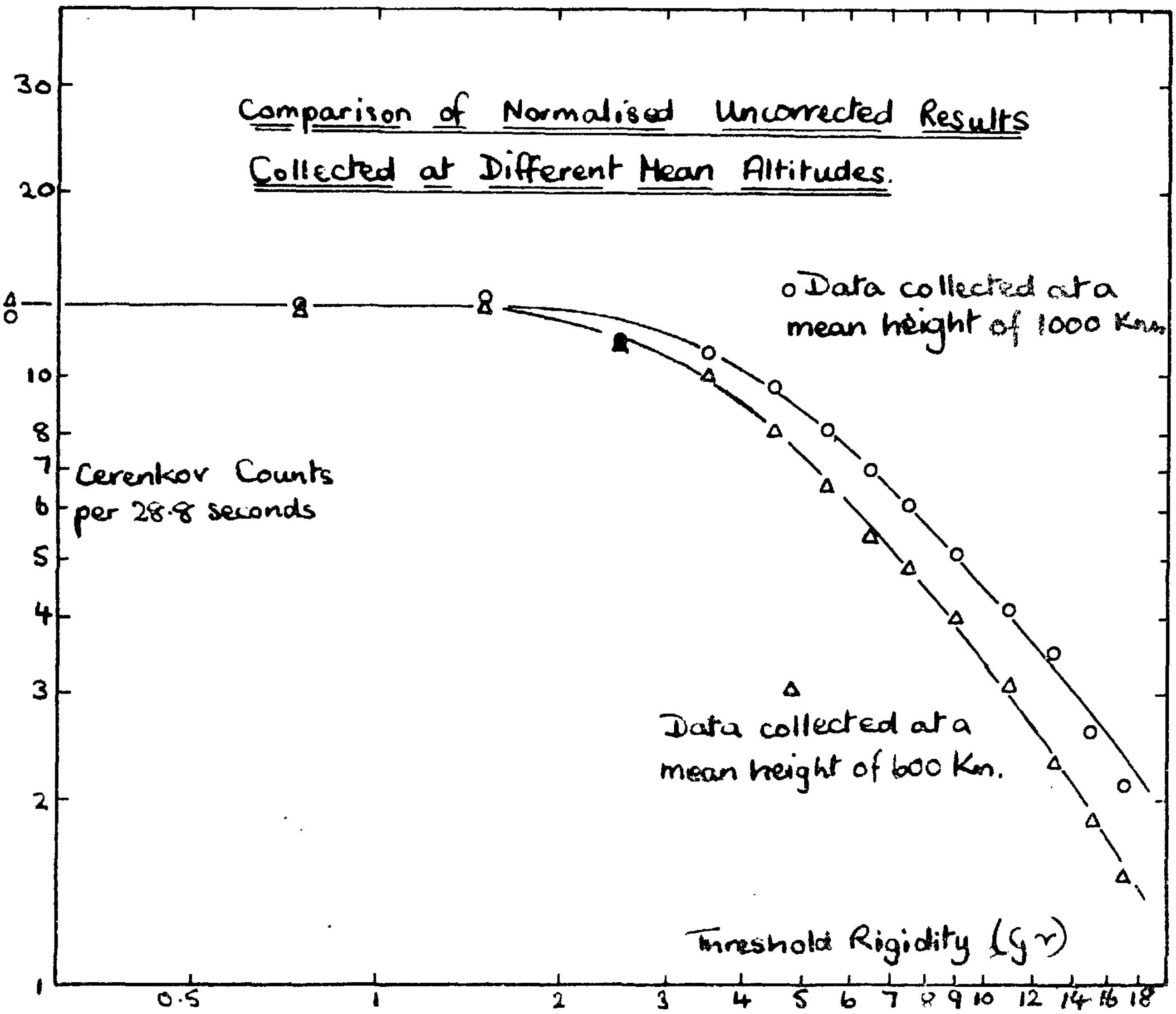
Comparison of Normalised Uncorrected Results
Collected at Different Mean Altitudes.
o Data collected at a mean height of 1000 Kms
Δ Data collected at a mean height of 600 Km.
Cerenkov Counts per 28·8 seconds
Threshold Rigidity (Gv)
30
20
10
8
7
6
5
4
3
2
1
0·5
1
2
3
4
5
6
7
8
9
10
12
14
16
18

is almost completely transparent at sea level. Therefore we would expect it to have little effect above 35°, and that the correction factor at Quenby-Wenk values less than about 8 Gv would be proportional to $1/r^2$. Despite this prediction there is no firm evidence of this if figure 16 is examined. Therefore a correction factor of 0.7 (ie. R proportional to $1/r^4$) has been assumed for rigidity values down to 2 Gv.

It is hoped eventually to use the model experiment which is in operation at Imperial College to improve the accuracy of these threshold rigidity corrections by increasing our understanding of the problem, but for the present, as a first approximation it may be assumed that the effective threshold rigidity at an altitude of 600 km is given by:

$$R_{eff} = 0.7\, R_q + 3.1 \cdot 10^{-3} R_q^{\,2} \quad (\mp 8\%)$$

The error here is a combination of the empirical error arising from the altitude adjustment and an error which is harder to determine since it depends on how far the true state of affairs differs from the assumption that the correction factor needed for each lattitude is given by the expression for $R_{eff\ (sea\ level)}$ on page 52.

The size of the empirical error may be deduced from figure 16 and is ∓ 4%.

The error due to applying the expression for $R_{eff\ (sea\ level)}$ will probably be greatest in the 12 Gv threshold rigidity region, where large changes in the penumbra and shadow cones are occuring. It is estimated that the error here will not be larger than the size of the correction factor itself, or ∓ 7%. Above 30° of lattitude (at threshold rigidities lower than 10 Gv) where the factors influencing the rigidity values become less complex, and also at the equator, the expected error would be much less. Thus the error shown in the above result is a possible maximum.

4.2.3 Earth Shadowing Effect.

As the spacecraft moves in its orbit, we would expect a variation in the counting rate owing to the varying portion of the sensitive solid angle of the detector that is blocked by the Earth. This may be called the Earth shadowing effect. Figure 17 illustrates the aspect of the satellite on two days, day 120 and day 130. The shape of the curve changes slowly from the day 120 shape to the day 130 shape in the intervening period. The hatched portion represents the area covered by these intervening curves where the altitude was less than 800 km. In other words this hatched portion represents the aspects of the satellite for the results from this period that were used in this preliminary calculation of the primary spectrum. For these results it can be seen immediately that the Earth's shadowing effect is much greater in the northern hemisphere than in the southern. The contrast between the effects in the two hemispheres is greater during this period than at any other before the Starfish explosion. If the average counting rates for the various threshold rigidities in the northern and southern hemispheres are compared for this period, it is found that the greatest differences (south - north) for any threshold rigidity are given by:

$$\text{attenuated level difference} = (1.5 \mp 2.5)\ \%$$

$$\text{unattenuated level difference} = (-3.3 \mp 2.5)\ \%$$

Figure 17

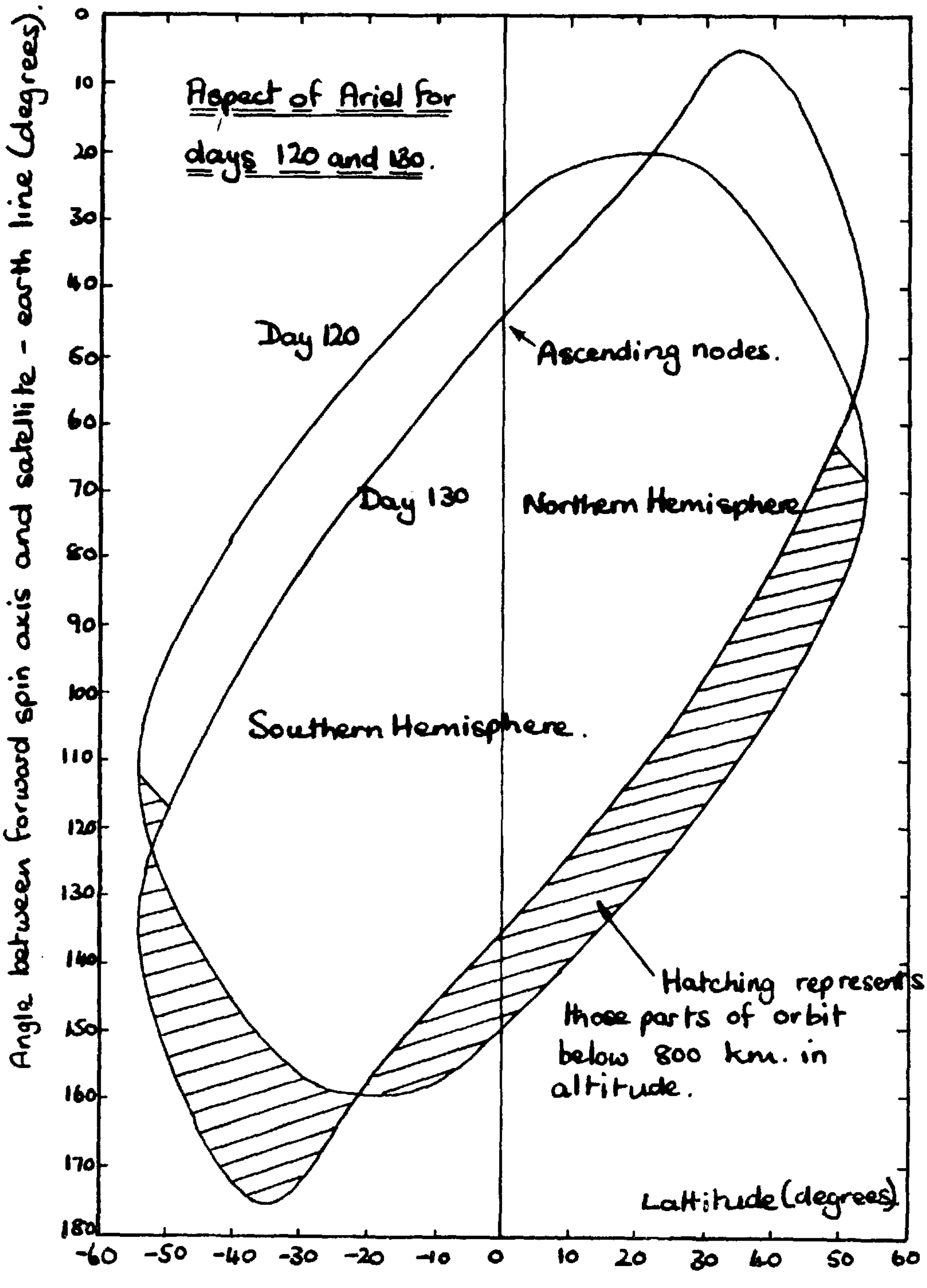
Aspect of Ariel for
days 120 and 180.
Day 120
Day 130
Ascending nodes.
Northern Hemisphere
Southern Hemisphere.
Hatching represents
those parts of orbit
below 800 km. in
altitude.
Angle between forward spin axis and satellite - earth line (degrees).
Latitude (degrees)
0
10
20
30
40
50
60
70
80
90
100
110
120
130
140
150
160
170
180
-60 -50 -40 -30 -20 -10 0 10 20 30 40 50 60

Thus, by empirical means, it may be concluded that the error introduced by this aspect effect is negligible compared with the error in the corrected threshold rigidities, and so no correction has been attempted.

In addition to the above, another type of counting rate variation will arise from the variation of threshold rigidity over the different parts of the sky. If the sensitive solid angle of the detector is blocked by the Earth so that only part of the sky is visible, then due to this variation of threshold rigidity, the portion of sky seen by the detector does not necessarily have the same effective threshold rigidity as does the whole of the sky. This effect will be most marked in the equatorial plane.

The data were examined for such an effect. Counting rate variations caused by the first Earth shadowing effect were removed by considering only those parts of the orbit where the angle between the spin axis of the satellite and the satellite-Earth line was 90°. This occurred at the equator only in the region of days 145 and 190. The region around day 145 was chosen for inspection because of the better statistics (the counting rate was higher) and because the heights at the equatorial crossings (the nodes) were almost the same. The counting rates for the ascending node and the descending node respectively were averaged using data taken between 10° north and 10° south of the geomagnetic equator for days 145 to 150 inclusive. The daily means were weighted to take into account the varying gain of the detector at this time. It was found that the ascending nodes had a mean counting rate 18 % greater than the descending nodes, but this difference disappeared when the slight disparity in mean heights was taken into account, using $1/r^4$ for correction. The two values were then 5.26 and 5.46 in arbitrary units. These agreed within their statistical errors which were 4 % and 3 % respectively. Thus if we examine the most likely lattitudes with the best satellite aspect for this effect we find it must be less than ∓ 5 %. This error will be greatly reduced when the results are averaged over long periods with varying aspects, and so again it is less than that for the threshold rigidities and no correction has been attempted.

4.2.4 Altitude Considerations.

Apart from the correction to the threshold rigidities for altitude as is outlined in section 4.2.2 there must be a different type of altitude correction. This arises from the increase in counting rate caused by the increase in the solid angle from which particles can arrive at the detector as the spacecraft moves away from the Earth and the solid angle subtended by the latter at the satellite decreases.

Now in the period between about day 155 and day 165 the apogee and perigee occur at the northern and southern extremities of the orbit (figure 18). If the high lattitude, average counting rates in the northern and southern hemispheres are compared for this period (there is no effect due to change in the effective threshold rigidity with altitude at high lattitudes owing to the plateau in the rigidity - counting rate curve) then it is found:

Figure . 18

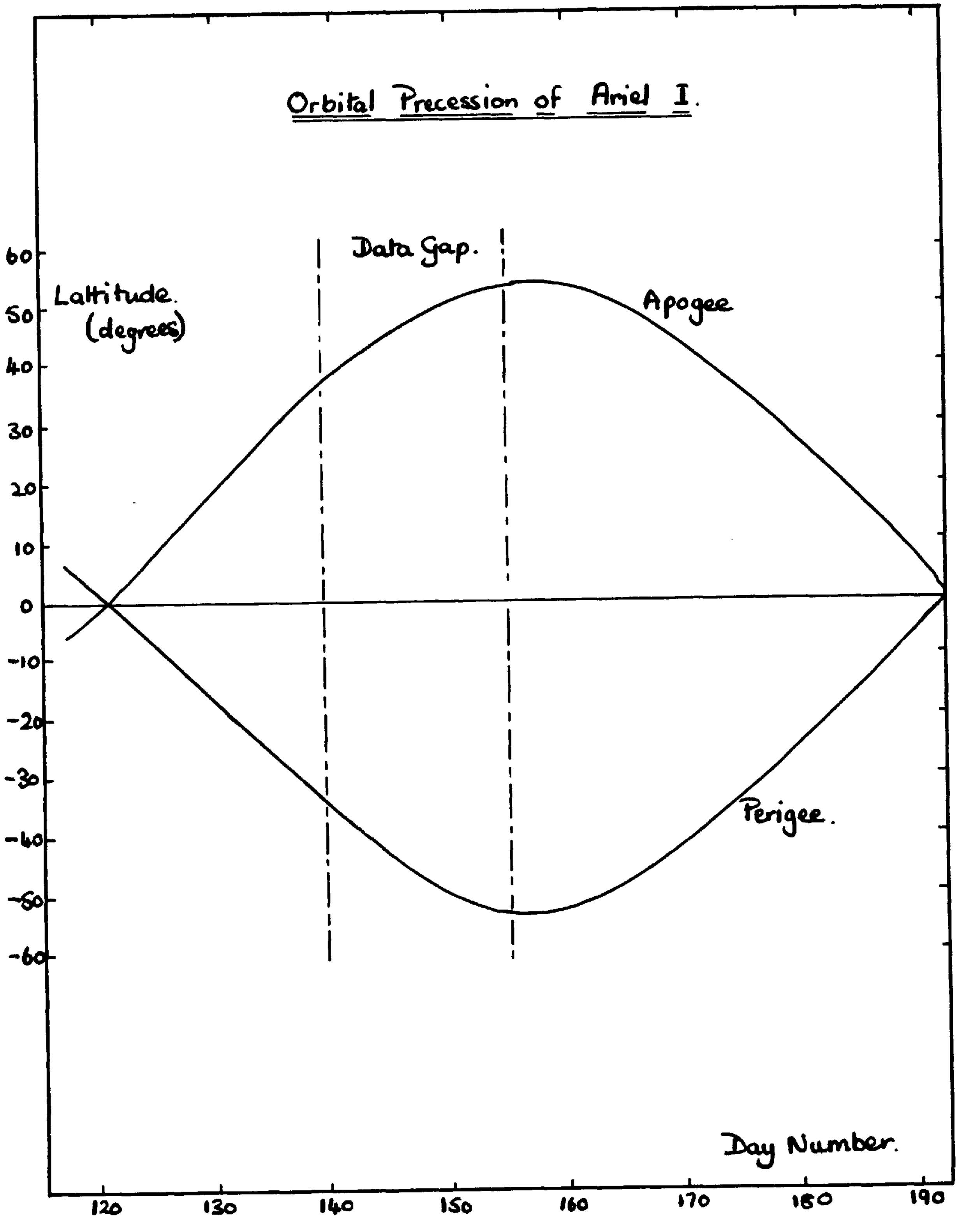
Orbital Precession of Ariel I.
Data Gap.
Lattitude
(degrees)
Apogee
Perigee.
Day Number.
60
50
40
30
20
10
0
-10
-20
-30
-40
-50
-60
120
130
140
150
160
170
180
190

attenuated level difference = (5.8 ∓ 2.5) %

unattenuated level difference = (10.7 ∓ 2.2) %.

There is an appreciable difference. However the averaging process reduces the error considerably since the altitude at each threshold rigidity varies as the orbit processes. Over the complete period from which the data were taken, the mean altitudes for the different rigidities were all found to lie within ∓ 25 km. Again this means there is a negligible error and correction was unnecessary.

4.3 Discussion of the Results.

The integral rigidity spectrum obtained from these results is shown in figure 19. There is a clear change of slope of the spectrum in the region of 8.5 Gv, and this is tentatively interpreted as the upper limit to the solar modulation process at this time (May - June 1962). The results for this spectrum were obtained at a relatively quiet period in the solar cycle as is illustrated by figure 20, which shows there were no large disturbances of the cosmic ray flux between April 26th and July 9th. The Mount Washington neutron monitor (geomagnetic lattitude = 57° N, altitude = 1909 metres above sea level) had returned to a counting rate between 8 and 10 % lower than its previous sunspot minimum at this period.

To determine the effect of the solar modulation process on the primary rigidity spectrum it is necessary to know the unmodulated shape of the spectrum. This is inaccurately known for the heavy nuclei, but in August 1956 (near solar minimum) the slope of the rigidity spectrum

Figure. 19

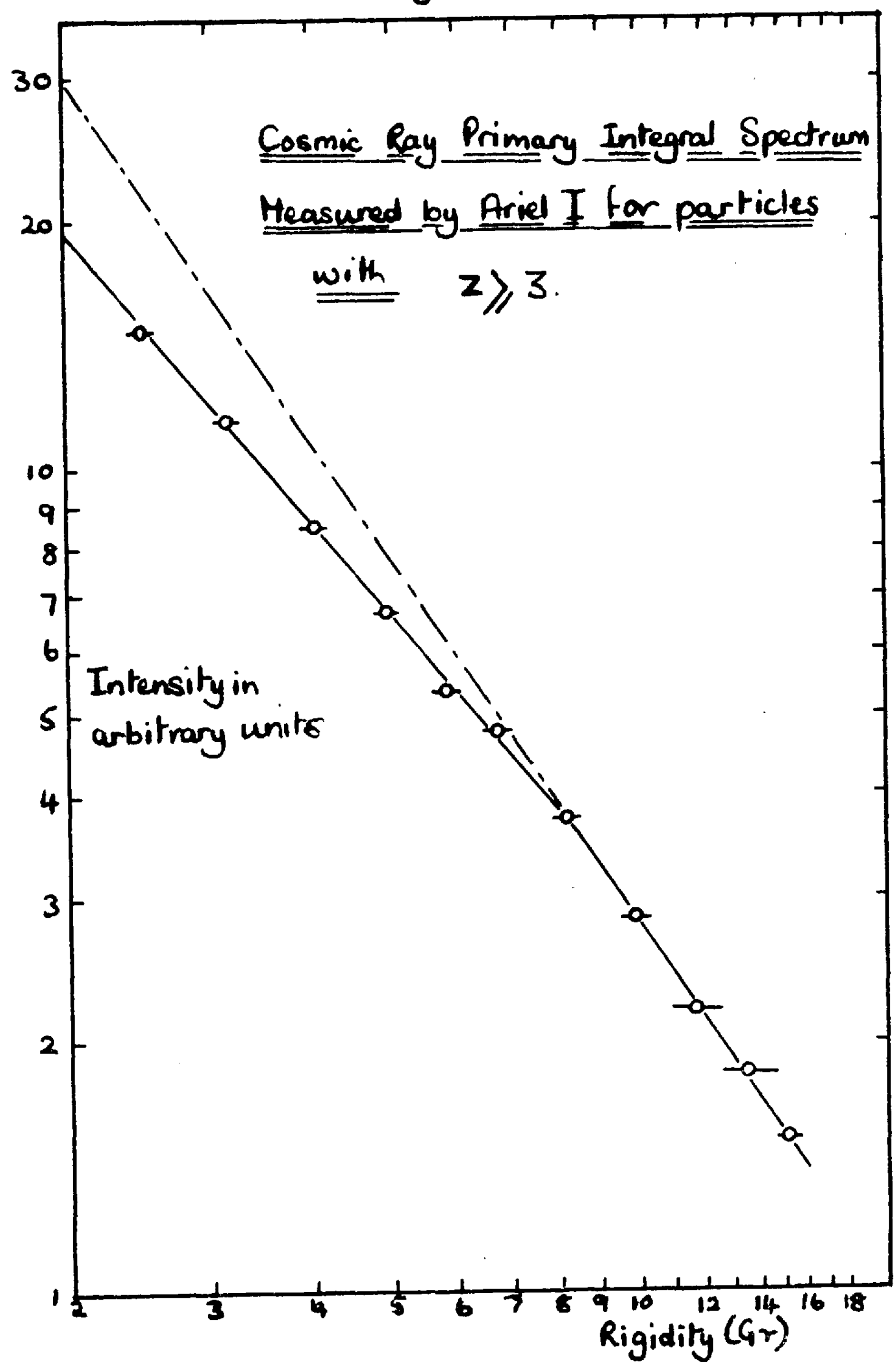
Cosmic Ray Primary Integral Spectrum
Measured by Ariel I for particles
with Z ≥ 3.
Intensity in
arbitrary units
30
20
10
9
8
7
6
5
4
3
2
1
2
3
4
5
6
7
8
9
10
12
14
16
18
Rigidity (Gv)

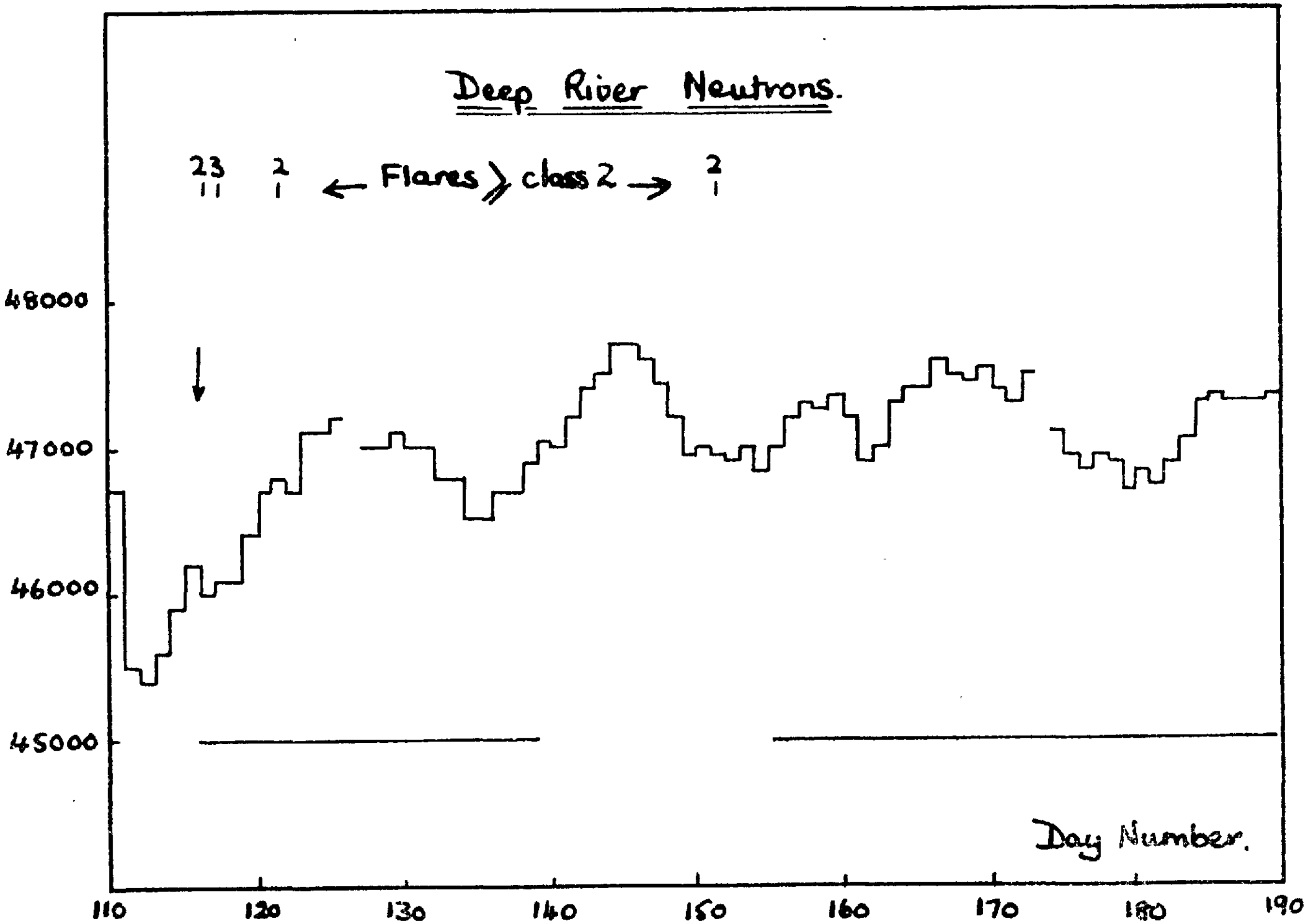
Deep River Neutrons.
2 3
2
← Flares ≫ class 2 →
2
48000
47000
46000
45000
Day Number.
110
120
130
140
150
160
170
180
190

Figure 20

for alpha particles was found to have an exponent of -1.5 in the rigidity range from 2 to 5 Gv (McDonald and Webber, 1959). This agrees with an extrapolation of the slope of the high rigidity end of our spectrum. From the measured difference in these slopes between 2 and 8.5 Gv, the rigidity dependence of the solar modulation in May and June 1962 may be represented by

$$I_e = I(R/R_o)^{0.3 \mp 0.15} \qquad \text{for } 2.5 < R < R_o$$

where I_o = intensity of primary cosmic rays with rigidities greater than R at the Earth,

I = intensity of cosmic rays at infinity,

R_o = 8.5 Gv.

From figure 19, the unmodulated primary cosmic ray rigidity spectrum for particles heavier than alpha particles above 8.5 Gv has an exponent of -1.5 ∓ 0.15.

The results of two experiments similar to ours have been published by Pomerantz and Witten, also by Kurnosova, Logachev, Razorenov and Fradkin, 1962. The Russian results are based on the data from cerenkov instruments flown in Sputniks V and VI, the American experiment consisted basically of an ion chamber carried by Explorer VII. These experiments were conducted at various periods during 1960, a time of high solar activity. The results are too statistically inaccurate and disturbed by time variations to allow any conclusions to be drawn when compared with the Ariel I results.

CHAPTER 5

THE GEOMAGNETICALLY TRAPPED PARTICLES

5.1 Introduction.

At 9 seconds past 09.00 hours U.T. on July 9th 1962, a nuclear bomb equivalent to 1.4 megatons of T.N.T. was exploded at a height of 400 km above sea level in the vicinity of Johnston Island in the central Pacific Ocean. A large amount of radiation was released by this explosion. Our instruments on Ariel I were able to detect some of this radiation and occasionally were able to indicate the type of particles which were present. The satellite was almost at its most southerly lattitude and near the geomagnetic longitude of the explosion at the time of detonation, and so was well positioned for observing the impact of the burst on normal conditions. Owing to the good data coverage, the distribution of the artificial radiation around the Earth and some early decay modes could be closely followed. Ariel I had been operating for 2½ months at this time so the areas apparently occupied by the natural radiation had already been mapped out. Because of this the artificial and natural radiations could be distinguished, and in this respect we had an advantage over following satellites, despite their better measuring ability. For these reasons an analysis has been made of the results obtained between the time of the explosion and the time when the satellite first went into undervoltage. In order to understand fully this analysis and its implications, some knowledge of the geomagnetically trapped radiation is necessary, and therefore a brief résumé is given in the rest of this chapter.

5.2 Experimental History.

The existence of the natural geomagnetically trapped radiation was discovered by J.A. Van Allen's research group, working at Iowa, who found that geiger counters launched in the earth satellites Explorer I and Explorer III were jammed by an unexpectedly high flux of radiation (Van Allen, 1958, also Van Allen et al. 1958). The presence of these high intensities of energetic particles was quickly confirmed by data from Sputnik III.

The observations from Sputnik III (Vernov and Chudakov 1960), Explorer IV (Van Allen, McIlwain and Ludwig, 1959) and Pioneer III (Van Allen and Frank 1959) showed regions of enhanced counting rates from L values of about 1.5 earth radii to values of about 10 earth radii with a region of low counting rates at about L = 2 earth radii. Thus the radiation appeared to be separated into two zones. The region for $L < 2$ earth radii was called the inner zone, and that for $L > 2$ earth radii was called the outer zone. L values are discussed in section 5.6.

Nuclear emulsions flown in rockets by Freden and White (1959) showed that the inner zone contained large numbers of penetrating protons. The 1959 rocket flights of Holly and Johnson (published 1960) showed electrons to be the most numerous particles in the inner zone. Reports of other investigations into the composition of the inner zone using rocket-borne apparatus may be found in Freden and White 1960, Naugle and Kniffen 1961, Armstrong et al. 1961, and Heckman and Armstrong

1962. The last reference contains a measurement of the proton spectrum of the inner zone for the rocket trajectory of this particular experiment. Naugle and Kniffen were the first to show that the proton spectrum becomes softer with increasing L value in the energy range between 10 and 100 Mev.

Cladis et al. (1961) demonstrated conclusively that the outer zone contained electrons. They measured the energy spectrum and pitch angle distribution of electrons near the lower edge of the outer radiation zone using apparatus flown in a Javelin rocket.

A comprehensive assault on the unknown aspects of the trapped radiation was carried out by instruments flown in Explorer XII. Data from this satellite showed that there were not two distinct zones, but instead the whole of the trapping region was filled with protons (Davis and Williamson, 1962) and electrons (O'Brien and Laughlin 1962, Rosser et al. 1962) whose energy spectra varied with distance from the Earth. However the use of the terms 'inner zone' and 'outer zone' will be continued in this thesis for convenience. Protons of roughly 100 kev energy and electrons with about 40 kev energy were found in crudely comparable intensities out as far as the boundary between the geomagnetic and interplanetary fields, which was at variable radial distances of between 8 and 11 earth radii on the daylight side of the earth at this time (August to December 1961, see Cahil and Amazeen 1962). Measurements of the electron spectra in the energy range of 40 to 110 kev were also made in the equatorial plane (O'Brien and Laughlin 1962).

Large variations of the particle flux have been observed (e.g.

Arnoldy et al. 1960, Pizzella et al. 1962). These variations appear to increase in amplitude with increasing distance from the Earth. They also appear to be related to solar flares in some way which is not clearly understood at present. The geographic position of X-ray bursts at balloon altitudes and the timing of aurora have been observed to coincide with reductions of counting rates in the outer zone. This is rather tenuous evidence for the dumping of outer zone electrons into the atmosphere. More recently, O'Brien (1962) using a direction sensitive counter in Injun I has observed large numbers of electrons entering the atmosphere at high lattitudes. Thus there is convincing evidence that at certain times the lifetimes of electrons in the outer zone may be only a few hours long. The time variations of the trapped radiation are of interest since they can give some indications of trapped particle lifetimes. These in turn can lead to conclusions concerning the origins of the trapped radiation; for example a weak source of trapped particles may supply the necessary flux if the trapped lifetime is long enough.

The experimental investigations of the trapped particles may be summarised by saying that the spatial extent of this radiation is roughly known, some preliminary work has been done on the study of the constituents, and time variations have been observed and associated with some geomagnetic phenomena. The origin of the trapped radiation and its exact operation in the mechanics linking solar explosions with magnetic storms and auroral activity on the Earth are still subjects for speculation.

5.3 Origin.

It has been pointed out that the decay of the neutron albedo produced by the interaction of cosmic rays with the Earth's atmosphere should lead to the trapping of both electrons and protons in the geomagnetic field (Singer 1958, Vernov et al. 1959, Kellogg 1959). Alternatively, it has been proposed (Gold 1959) that the trapped particles originate in the solar atmosphere and are transferred from the solar to the terrestial magnetic fields by the magnetohydrodynamic effects occuring at the boundary between these fields during magnetic storms.

It seems possible that an appreciable number of the trapped protons have their origin in neutron albedo produced by solar flare generated protons (Lenchek 1962). Some discussion has taken place as to whether a sizeable contribution to the trapped protons is also due to albedo arising from the normal cosmic ray flux. There appear to be two schools of thought on this matter (Lenchek and Singer 1962; Pizzella et al. 1962). However, the neutron albedo theory cannot account for the large numbers of trapped electrons which are observed. The solar origin theory has been discarded since the probe Pioneer V failed to find the large amounts of interplanetary radiation necessary to make this theory workable. It seems more likely that a large number of the trapped electrons are accelerated in situ by hydrodynamic waves generated at the magnetosphere surface by impingeing solar plasma. This was suggested by Dessler in 1958. The exact mechanics of this process are still obscure.

5.4 Artificial Radiation Belts.

Following a suggestion by Christofilos (1959) artificial radiation belts were produced at L values of 1.72, 2.12 and 2.16 earth radii by a series of high altitude nuclear explosions during August and September of 1958. This operation was given the code name 'Argus'. The objects of these tests were to demonstrate that particles could be trapped in the Earth's magnetic field, to check calculations of the trajectories of these particles and to study the effects of the explosions at the points of the bursts and at the magnetic conjugates. Aurora and magnetic disturbances were seen at these positions (Newman 1959, Peterson 1959). The artificial radiation belts were found by Explorer IV which was launched for the purpose of detecting them. They were sufficiently stable for Van Allen et al. (1959) to be able to say that the radial diffusion rate of the particles could not be greater than 2 km. per day at a height of 1500 km. above the surface of the Earth. On the day of a magnetic storm some evidence was found for a decrease in the intensity of the two artificial belts then existing.

Effects of the Starfish nuclear explosion are discussed in Chapter 6.

5.5 Motion of Charged Particles in a Dipole Field.

The compexities of this problem may be reduced by using as an approximation the concept of the 'guiding centre' of a particle. This concept was introduced by Alfven (1960). The particle motion here is described in terms of:

a. A rapid gyration about a field line with a cyclotron period T_c and radius R_c. The centre of this gyration is the guiding centre.

b. Motion of the guiding centre of the particle along the line of force. This motion is periodic also; the particle is reflected by the converging magnetic field near the Earth and bounces back and forth in the exosphere with a bounce period T_b.

c. A drift in longitude around the Earth with a period of revolution T_r.

Assuming the Earth's field may be approximated by a dipole field, the following table has been calculated for particles at 2000 km. altitude near the equator (L = about 1.3 earth radii) and gives a useful idea of the quantities involved (Hess 1962).

	R_c	T_c	T_b	T_r
50 kev. electron	50 m.	2.5 microsec.	0.25 sec.	11.5 hrs.
1 Mev. electron	320 m.	7 microsec.	0.1 sec.	53 min.
1 Mev. proton	10 km.	4 millisec.	2.2 sec.	32 min.
10 Mev. proton	30 km.	4.2 millisec.	0.65 sec.	3.2 min.
500 Mev. proton	250 km.	6 millisec.	0.11 sec.	5.04 sec.

For a comprehensive mathematical discussion of the Stormer, Alfven and McIlwain calculations of the motions of charged particles in dipole and near-dipole fields see H. Elliot (1963).

5.6 L - Vales.

As extensive use is made of this concept in the next chapter, a brief attempt at a physical explanation is given here. The mathematical basis will be found in articles by McIlwain (1961) and Elliot (1963).

A charged particle, drifting in the Earth's magnetic field, can be shown to cling approximately to a surface constructed of magnetic lines of force (McIlwain 1961). These lines of force are defined by McIlwains' so-called longitudinal invariant. The surface may be called a magnetic shell and is labelled by a quantity L. The definition of L is such that if the magnetic field of the Earth was a perfect dipole field centred on the centre of the Earth, then the distance between the latter and any L shell in the equatorial plane, when stated in earth radii, would give the L value of that shell.

Now as the trapped particle spirals towards the Earth along a line of force, its rate of approach is slowed down by the increasing magnitude of the scalar magnetic field (B), and it is eventually turned back at the maximum value of B which the particle can reach. For any one particle this value of B is the same at each of these reflection points, which are known as 'mirror points'.

Thus the orbit of any trapped particle can be completely defined by two quantities: the value of L for the shell to which the particle is tied and the value of B at the mirror points. Therefore each point on a graph where B is plotted against L will represent a particular particle orbit, and so the B - L diagram is a convenient (because it is two dimensional) method of classifying trapped particle orbits.

As an example of this, trapped particle populations can be represented by contour lines on these graphs.

Care must be exercised when using this system to analyse satellite results since a particle observed by the detector has not necessarily reached its maximum B value.

To assist in the physical interpretation of B - L diagrams the Earth's surface has been transposed into B - L coordinates and this process is described below. Although an idealised Earth's surface has been used, this is useful in giving some indication of those parts of a B - L diagram which must lie below sea level and therefore cannot be occupied by trapped particles.

In magnetic coordinates, the Earth's surface may be located by the scalar magnitude of the magnetic field at sea level and by the magnetic shell which intersects any particular geographic point. If, again, the Earth's magnetism was represented by a perfect dipole located at the Earth's centre, its axis being the spin axis of the Earth, then the system would be entirely symmetrical about the dipole axis and the field on the Earth's surface would be constant with longitude. Thus for any given L shell at the Earth's surface there would be a unique value of B, and the Earth's surface would be represented by a single curve in a B - L diagram However, as a first approximation, the Earth's magnetic field is represented by a perfect dipole displace 430 km. from the Earth's centre. Figure 21 shows the Earth's surface in a magnetic coordinate system, in this case polar geomagnetic coordinates. Two particular longitudes have been superimposed in this diagram. The inner curve

Figure 21

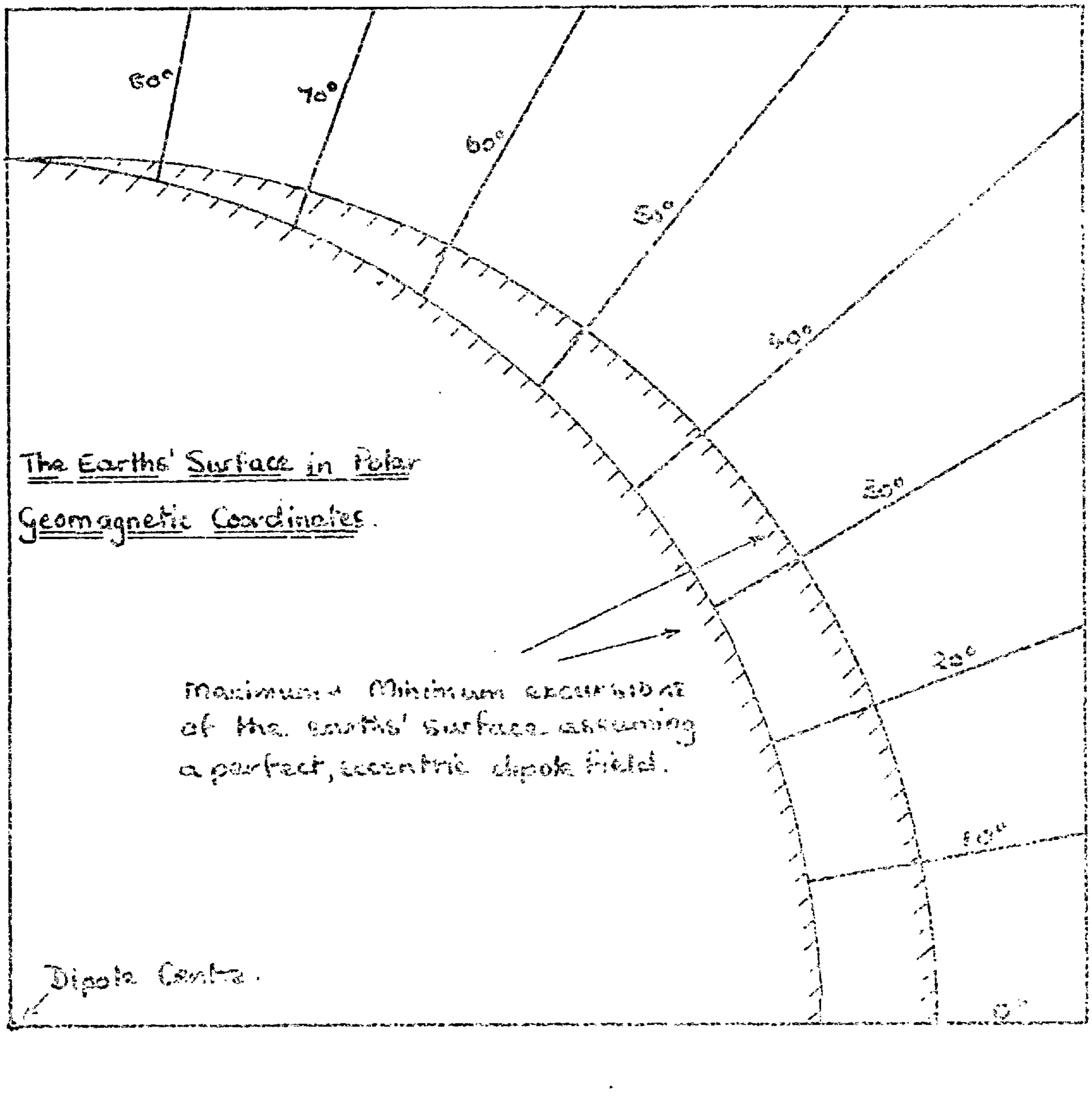

80°
70°
60°
50°
40°
30°
20°
10°
0°
The Earths' Surface in Polar Geomagnetic Coordinates.
Maximum + Minimum excursions of the earths' surface assuming a perfect, eccentric dipole field.
Dipole Centre.

shows the longitude with the largest B values at the Earth's surface and the outer curve represents the longitude with the smallest B values. All other longitudes with intermediate values of B must be represented by curves which lie between these two. The angles shown are geomagnetic lattitudes. This diagram demonstrates that the Earth's surface cannot be drawn as a single line when a magnetic system of coordinates is used. In figure 22 these two longitudes are shown in another magnetic coordinate system, B - L coordinates this time. The 'distortion' from figure 21 is evident. The angles shown are again geomagnetic lattitudes.

In actual fact, superimposed on the eccentric dipole field of the Earth are magnetic anomalies which will distort these curves even more by varying the quantity B. It is useful to know in B - L coordinates the position of the line representing the Earths surface where the mirror points of trapped particles are at their lowest altitudes. This 'lowest mirror points line' is shown in figure 22. Particles which are observed above this line in B - L coordinates cannot drift completely around the Earth since their theoretical mirror points must be below sea level for some longitudes. The broken line in figure 26 shows the geographic position of the lowest mirror point line.

Figure 23 shows various heights above the Earth's surface on the lowest mirror point line. The B and L values from which these curves were constructed were calculated by Hess (private communication) using Jensen and Cain coefficients.

Figure. 22

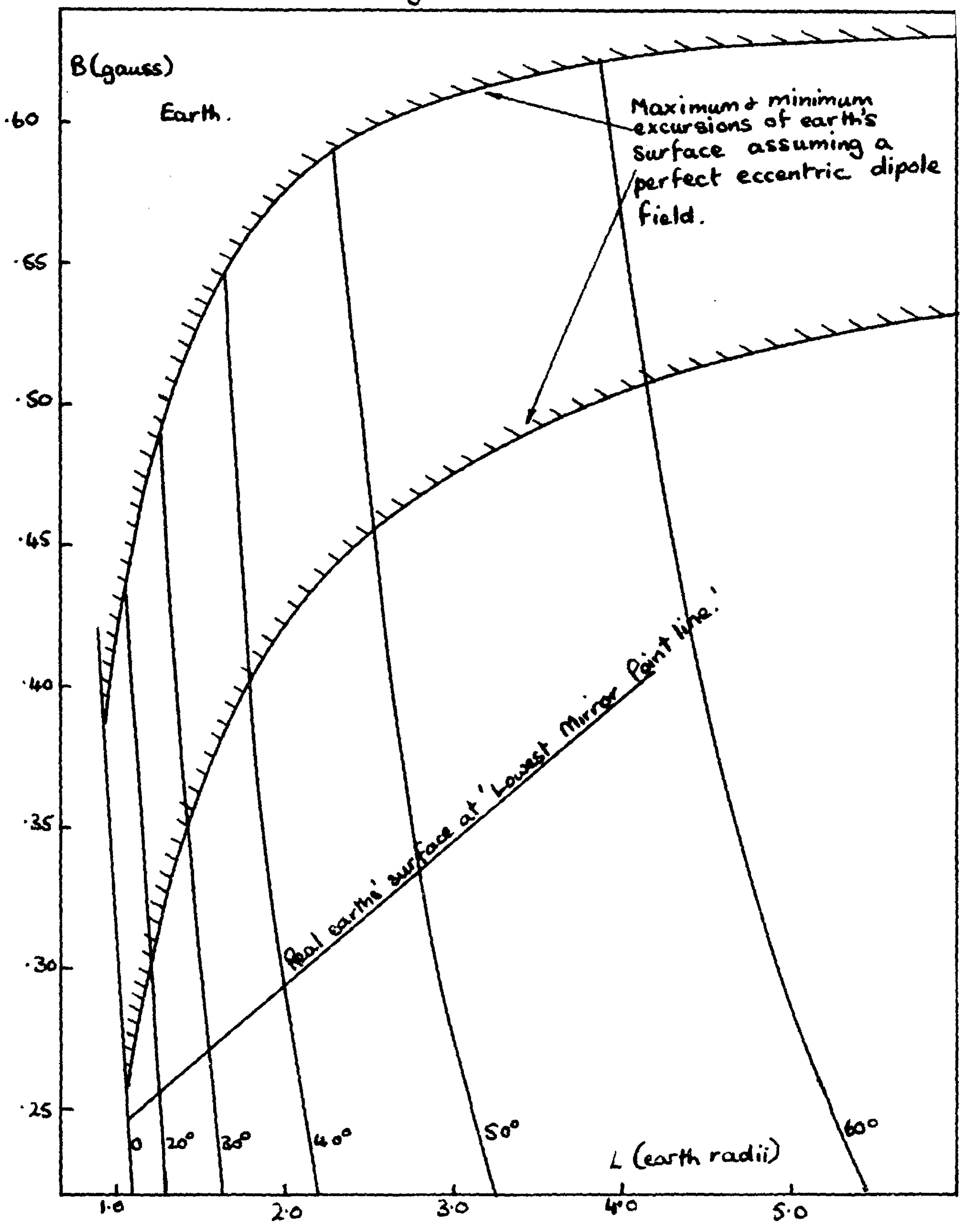

B (gauss)
Earth.
Maximum & minimum excursions of earth's surface assuming a perfect eccentric dipole field.
Real earth's surface at 'Lowest Mirror Point line.'
·60
·55
·50
·45
·40
·35
·30
·25
0
20°
30°
40°
50°
60°
L (earth radii)
1·0
2·0
3·0
4·0
5·0

Figure. 23

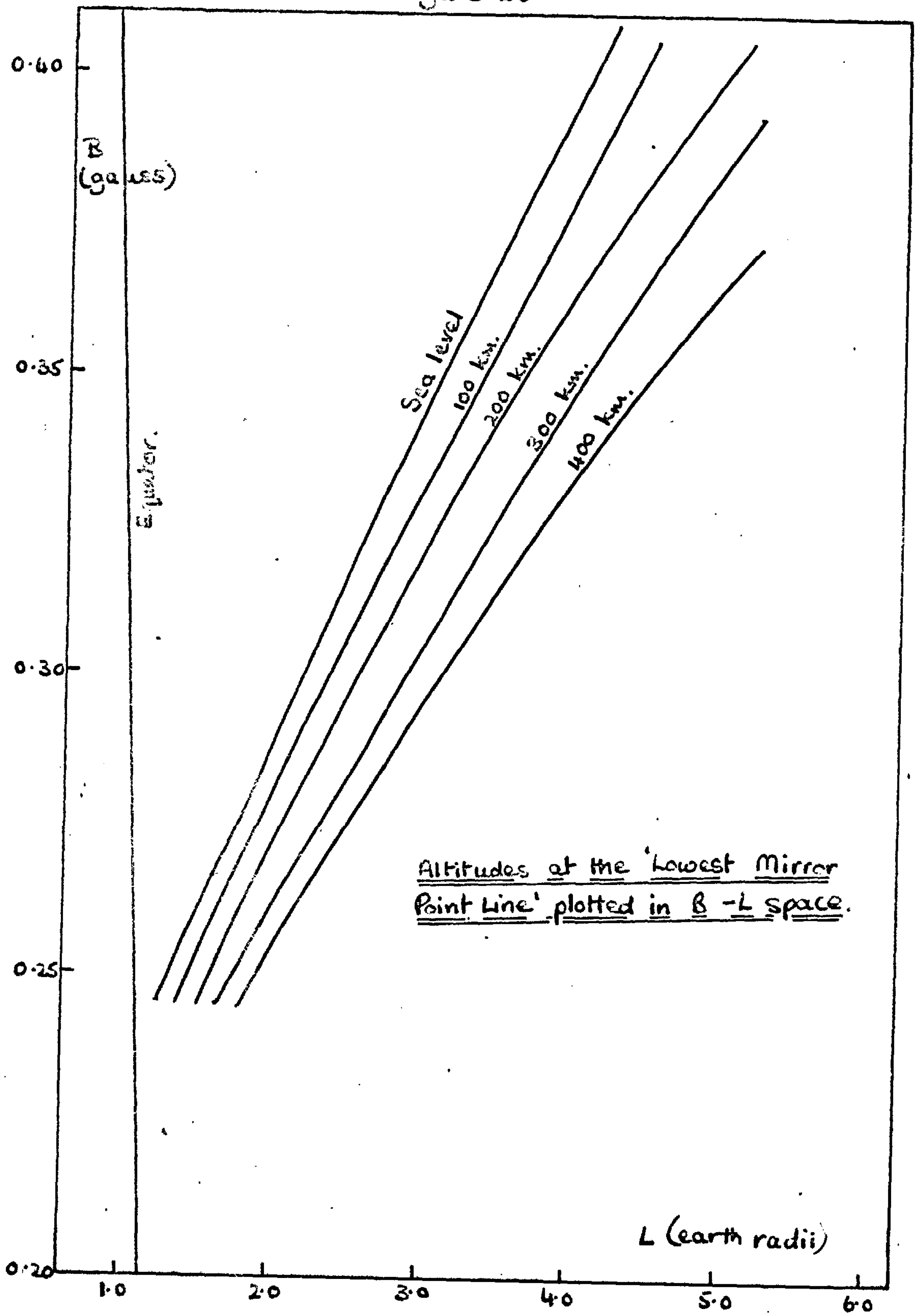
0·40
0·35
0·30
0·25
0·20
B
(gauss)
Equator.
Sea level
100 km.
200 km.
300 km.
400 km.
Altitudes at the 'Lowest Mirror
Point Line' plotted in B -L space.
L (earth radii)
1·0
2·0
3·0
4·0
5·0
6·0

CHAPTER 6

THE STARFISH NUCLEAR EXPLOSION

6.1 Introduction.

As stated previously, the explosion occurred at 9 seconds past 09.00 hours U.T. on July 9th, 1962 at a height of 400 km. above sea level. The position was 16.7° N, 169.5° W in geographic coordinates, or B = 0.29 gauss and L = 1.12 earth radii in trapped particle coordinates (Van Allen et al. 1962). Aurora were seen immediately at the magnetic conjugate and as far south as New Zealand (30 geomagnetic degrees below the conjugate, Gabites and Rowles, 1962), widespread magnetic disturbances were reported, for example by Casaverde et al. 1963, or Gill 1962, and synchrotron radiation was found to spread into a belt encircling the Earth and extending 25 degrees on either side of the geomagnetic equator. The latter was reported by Dyce and Horowitz, 1963.

Before discussing the picture which may be built up from the Ariel results, it is desireable to have some idea of the quantities involved in this explosion so that these can form a background for any calculations which are necessary. A theoretical summary of these quantities is made below.

6.2 A Summary of the Explosion Quantities.

An unspecified fraction of the explosive power was due to fusion. This means that in calculations of the effects caused by fission, upper limits can be established if it is assumed that the whole explosion was due to fission.

The energy released by a 1.4 megaton fission explosion equals 6×10^{22} ergs, $= 3.5\times10^{28}$ Mev (Singer, 1962). If each fission releases about 200 Mev, then the total number of fissions could be about 2×10^{26}. This would yield some 10^{27} electrons from decay of fission products (Latter, Herbst and Watson 1961) with a differential energy spectrum probably approximated by $3.86 \exp.(-0.575\,E - 0.055\,E^2)$ for the range $1 < E < 7$ Mev, where E is the kinetic energy of the electron in Mev and the spectral expression is in units of electrons per fission per Mev (Carter, Raines,Wagner and Wyman, 1959).

According to Latter, Herbst and Watson about one neutron per fission escapes from a nuclear burst, thus an upper limit of about 2×10^{26} fission neutrons could be released from the Starfish explosion. These neutrons would have a most probable energy of 0.8 Mev and a mean energy of about 2 Mev (Atomic Energy Commission, 1955). They would decay into electrons of about 780 kev energy and protons mostly with energies of 1 Mev.

In the first 10^{-7} seconds after a fission explosion, a burst of prompt γ rays is emitted, the total flux being given by the nominal expression:

$$F = Y_f\, 10^{10}/R^2 \quad \gamma \text{ rays per cm}^2. \qquad (\text{ Singer })$$

where Y_f = fission yield of the explosion in kilotons,

F = flux, distance R km. from the explosion.

Following this, delayed γ rays are emitted from the fission fragments as they decay. The total flux for the first second after the explosion is roughly constant and 100 times greater than the total flux of prompt γ rays. After this first second the flux falls off according to $t^{-1.2}$ so we may write:

$$F = Y_f \, 10^{12} \, t^{-1.2}/R^2 \quad \gamma \text{ rays per cm}^2 \text{ for } t > 1 \text{ sec.}$$

The mean energy of these fission fragment decay γ rays is about 1.5 Mev (Petrov, 1960).

In the case of a fusion explosion, the reactions give rise to 14 Mev neutrons. Assuming all these neutrons escape, this gives an extreme upper limit of about 3×10^{27} for fusion neutrons if a completely fusion explosion is assumed.

Bearing the above figures in mind, the following analysis was performed using data from the 4th June to about 2100 hours on the 12th July when the satellite went into undervoltage for the first time. The analysis assumes that there was negligible disturbance to the radiation around the Earth from natural causes between the 9th and the 12th July. This assumption is supported by the information shown in figure 24. Class one flares were found from previous data to have undetectable effects on the particle densities at the energies seen and in the regions scanned by our detectors in Ariel.

6.3 Outer Natural Radiation Belt Particles.

6.3.A Figure 25 illustrates the counting rates recorded by the geiger and cerenkov detectors immediately before and after the explosion. From the counting rates recorded by the geiger it is apparent that the satellite encountered two distinct bursts of particles, labelled burst A

Figure. 24

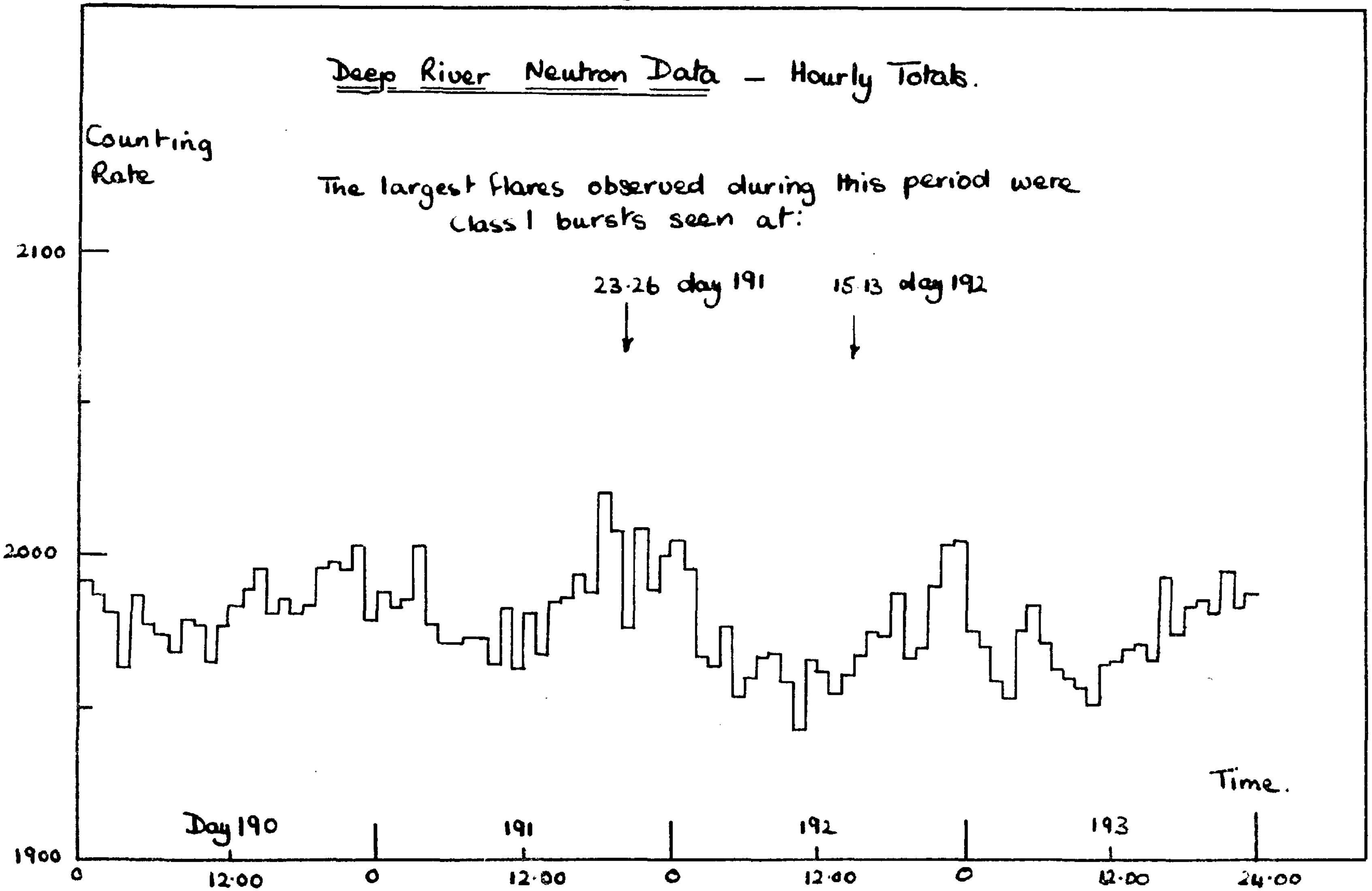
Deep River Neutron Data – Hourly Totals.
Counting Rate
The largest flares observed during this period were
Class I bursts seen at:
23.26 day 191
15.13 day 192
2100
2000
1900
Time.
Day 190
191
192
193
0
12:00
0
12.00
0
12.00
0
12.00
24.00

Figure. 25

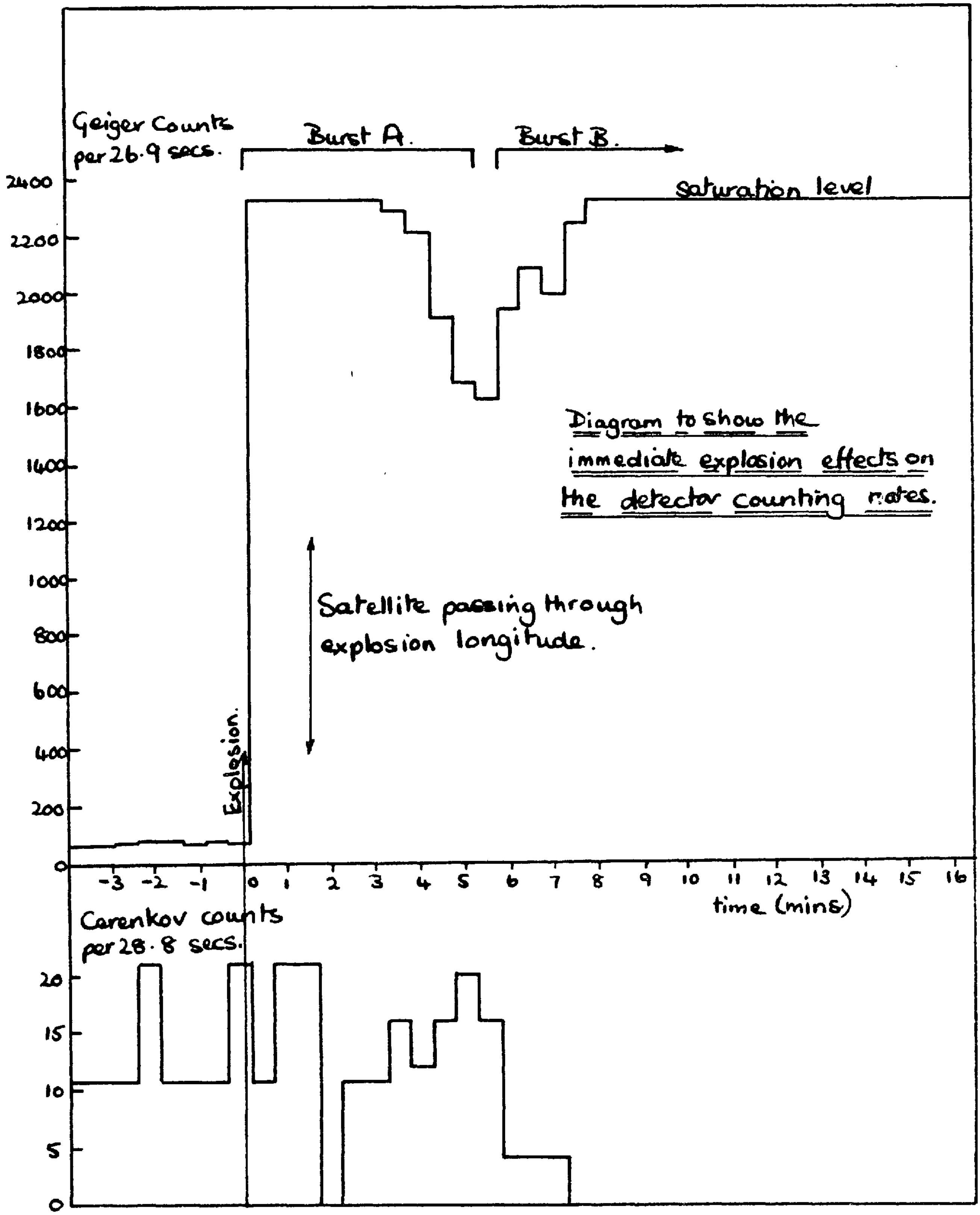
Geiger Counts per 26·9 secs.
Burst A.
Burst B.
saturation level
2400
2200
2000
1800
1600
1400
1200
1000
800
600
400
200
0
Diagram to show the immediate explosion effects on the detector counting rates.
Satellite passing through explosion longitude.
Explosion.
-3 -2 -1 0 1 2 3 4 5 6 7 8 9 10 11 12 13 14 15 16
time (mins)
Carenkov counts per 28·8 secs.
20
15
10
5
0

and burst B for convenience. Burst A commenced within 20 $\mp$ 10 seconds of the explosion (the satellite was at an altitude of 819 km, latitude 52° S, longitude 163° W). The cerenkov detector, however, saw only burst B, it was unaffected by the particles in burst A. This is illustrated by figure 26 in which the group of points from burst A lies in a different area to those from burst B and in such a position that they show the cerenkov detector was counting at the normal cosmic ray rate during this burst.

Now protons released by the explosion would not be energetic enough to penetrate either of the detectors. The L values of the satellite position during burst A (L = 4.7 to 3.5 earth radii) ensured that no inner belt protons (L = 2.4 earth radii, see figure 27) were present. Thus from the discussion of cerenkov detector saturation in section 2.4, page 27, we may say immediately that in burst A the geiger was mainly counting either γ radiation or bremsstrahlung from electrons of energies less than about 2 Mev.

Multiplying the geiger saturation rate of 2,300 counts per interval by the geometric factors of the geiger counter from section 2.1 for bremsstrahlung and γ rays respectively it is found that the flux was at least:

$$10^7 \text{ electrons per cm}^2 \text{ per second,}$$

$$\text{or } 5 \times 10^4 \ \gamma \text{ rays per cm}^2 \text{ per second.}$$

<u>6.3.B</u> Since the satellite was underneath the outer radiation belt at this time, it is tempting to say at once that burst A must be the

Figure 26

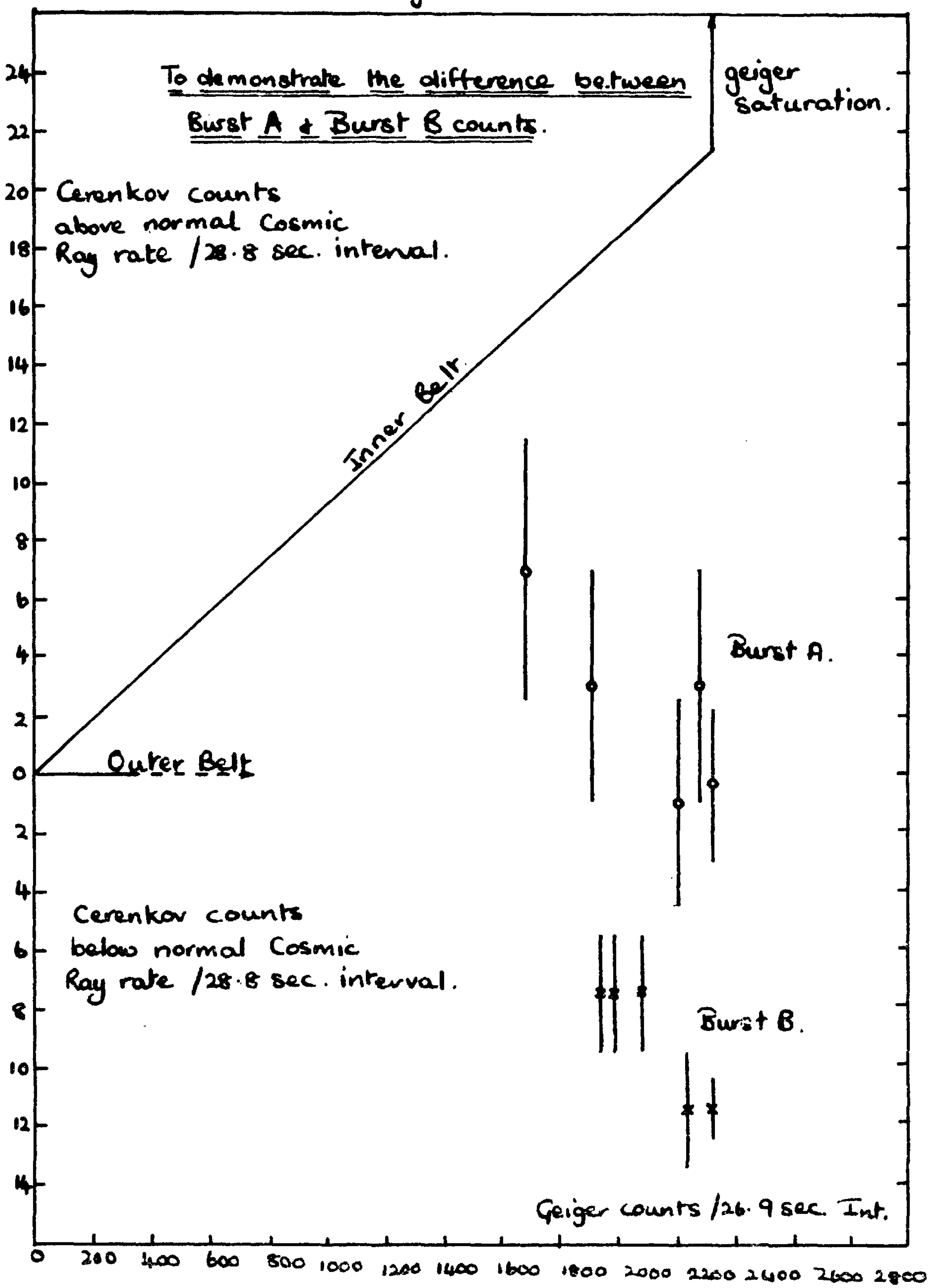
To demonstrate the difference between
Burst A & Burst B counts.
geiger saturation.
Cerenkov counts above normal Cosmic Ray rate /28.8 sec. interval.
Inner Belt
Outer Belt
Burst A.
Burst B.
Cerenkov counts below normal Cosmic Ray rate /28.8 sec. interval.
Geiger counts /26.9 sec. Int.
24
22
20
18
16
14
12
10
8
6
4
2
0
2
4
6
8
10
12
14
0
200
400
600
800
1000
1200
1400
1600
1800
2000
2200
2400
2600
2800

Figure. 27

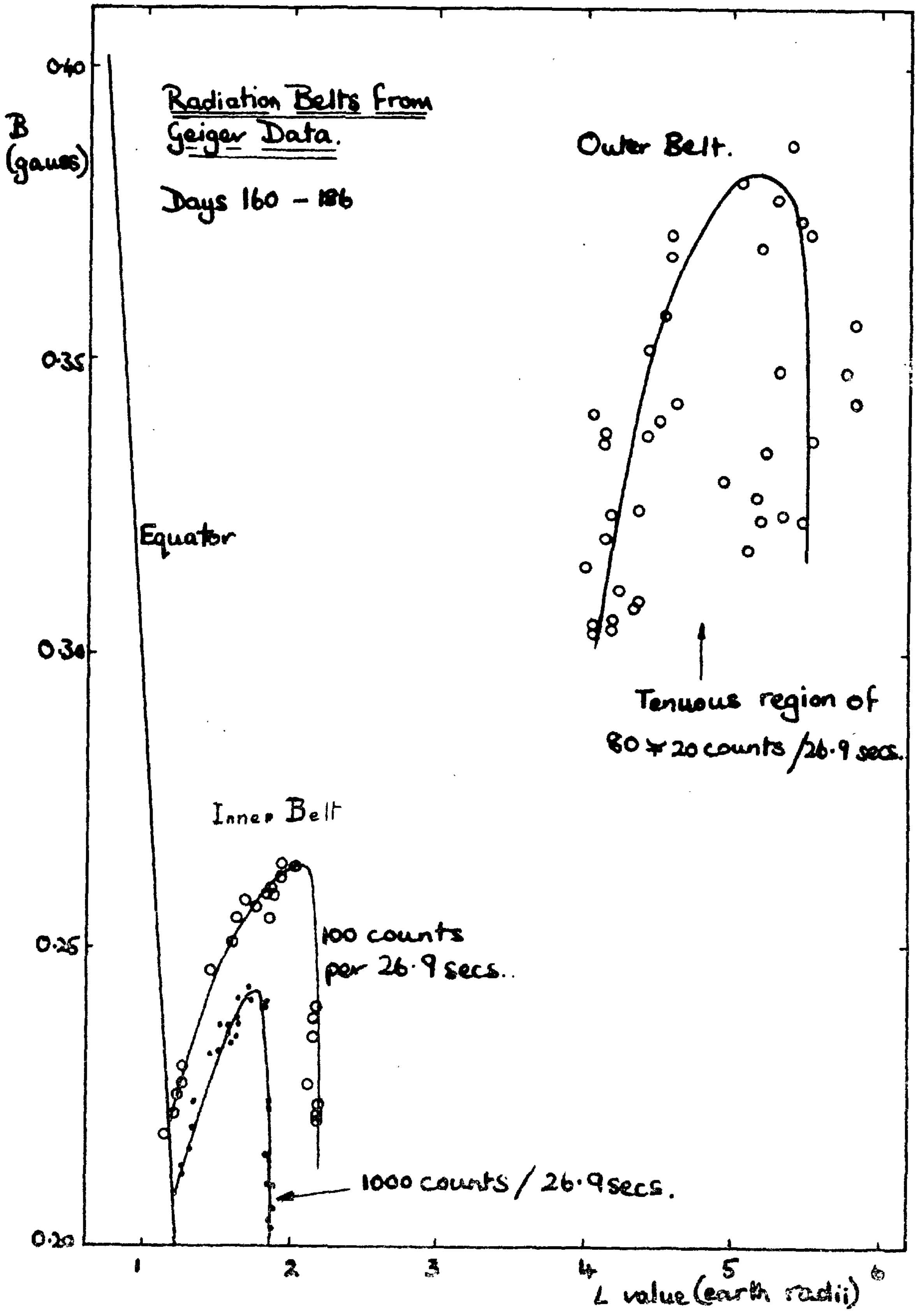
Radiation Belts from Geiger Data.
Days 160 - 186
B (gauss)
0.40
0.35
0.30
0.25
0.20
Outer Belt.
Equator
Tenuous region of 80 ∓ 20 counts/26.9 secs.
Inner Belt
100 counts per 26.9 secs.
1000 counts / 26.9 secs.
1
2
3
4
5
6
L value (earth radii)

observation of the dumping of outer belt electrons into the atmosphere as a result of the magnetic agitation caused by the explosion. However as the satellite was fairly close to the explosion, it is clear that some, or all of burst A could be due to radiation arriving at the satellite as a result of more direct processes. The processes which appear to be possible are examined in the following.

1. The particles could be electrons from the decay of fission fragments. This requires that the fission fragments should decay near to the line of force passing through the satellite at that time.

The energy spectrum of β particles from fission fragments is known (page 79) and large numbers of these electrons have energies greater than 2 Mev. Since no response of the cerenkov detector to burst A particles was observed, the flux of particles with energies greater than 2 Mev was below 10^4 per cm^2 per second, or less than 0.1 % of the electrons observed by the geiger counter, if they were electrons. Thus the energy spectrum was not that to be expected from fission fragment decay β particles, so we may reject this mechanism for causing the radiation observed as burst A.

2. Burst A could be caused by γ rays given out by fission fragments rising above the satellite horizon. The actual explosion occurred below the satellite horizon, so γ rays from the burst itself would not be detected. We have seen that at a time t seconds after the explosion, a satellite distance R km from it encounters a flux given by the expression:

$$F = aY_f\, 10^{12}\, t^{-1.2} / R^2 \quad \gamma \text{ rays per cm}^2 \text{ per second,}$$

where a = the fraction of the fireball visible to the satellite,

Y_f = the fission yield in kilotons.

If we ignore the horizon effects, an upper limit calculation can be made as follows:

Y_f = 1,400 kilotons, assuming the complete explosion is caused by fission,

R = 8,300 km,

a = 0.5, since half of the fission fragments must go down into the atmosphere.

So the flux at Ariel could be a maximum of 2×10^7 γ rays per cm^2 per second.

Now 5×10^4 γ rays per cm^2 per second is the minimum flux which may saturate the geiger counter, so it would appear that the saturation could easily be caused by this γ radiation. However, owing to the decay of the γ ray flux with time, saturation of the geiger counter would be expected to stop a maximum of T seconds after the explosion where:

$$F = 5 \times 10^4 = 2 \times 10^7\, T^{-1.2}$$

This gives T = 150 seconds.

In fact the geiger saturation was observed to last until 210 ∓ 10 seconds after the explosion, so a hard upper limit of T = 150 seconds makes it doubtful that γ rays from fission fragments could be the mechanism to explain burst A.

Further doubt is cast on this mechanism if the onset time of the burst is examined. Fenton (Edwards et al. 1962) flew a balloon from

Hobart (43^{o} S, 147^{o} E, L = 3 earth radii) at this time. The explosion occurred when the balloon had reached a depth of 80 gm per cm^2 (about 18 km. above sea level). A burst similar to Ariels' burst A was observed by the instruments with an onset time 15 ∓ 7 seconds after the explosion. As the explosion ocurred 4,500 km. below the horizon of the balloon, the fission fragments would have to travel with a velocity of 300 ∓ 80 km. per second to cause this onset. Section 6.5 indicates that the neutral fission fragments travelled with a velocity of 15 ∓ 5 km. per second, so this velocity would seem to be an order of magnitude too high. However, continuing to assume that burst A is due to this mechanism, the explosion ocurred 1500 km. below the horizon of Ariel, whose geiger counter first showed an increase 20 ∓ 10 seconds after the explosion, indicating fission fragment velocities of 100 ∓ 50 km. per second. This will be observed to disagree with the fission fragment velocities calculated from the balloon results.

Thus the timing of the onset and decay of burst A renders γ rays from neutral fission fragment decay a doubtful means for explaining this radiation entirely, although there is a possibility that some contribution was made by these rays.

<u>3.</u> The particles counted could be electrons from either fission or fusion neutrons released by the explosion which decay near to the line of force containing the satellite. In this case we would expect an immediate response from the geiger in Ariel since the velocities of both the neutrons and their decay electrons are relativistic. However a delay

of at least 10 seconds was observed. This fact alone is sufficient to make this mechanism unlikely. The calculations below also show that the flux is insufficient.

We may have a maximum of 2×10^{26} neutrons with a most probable energy of 0.8 Mev thrown out of a 1.4 megaton fission explosion. The shortest distance to the L = 4.5 shell for these neutrons is about 6,700 km. Consider 1 cc. of the L = 4.5 shell at this point.

A neutron of 0.8 Mev has a speed of 1.5×10^{9} cm. per second. The decay probability is 9×10^{4} per second and is therefore 6×10^{-13} per cm. at this velocity. Thus the number of neutrons which decay inside the distance of 6.7×10^{8} cm. is negligible.

We may then state that the total number of neutrons passing through the one cc. of L = 4.5 shell is $2 \times 10^{26} / 4\pi(6.7 \times 10^{8})^{2}$,

$$= 3.5 \times 10^{7}.$$

Thus the number of electrons injected into this one cc. by the explosion will be 2.1×10^{-5}. If we assume this to be the intensity all over the shell and neglect the atmospheric absorption, we find that Ariel may have encountered a maximum flux of $2 \times 10^{-5} c$ electrons/cm^{2}/second,

$$= 6 \times 10^{5} \text{ electrons/cm}^{2}\text{/second.}$$

This is an order of magnitude too small to saturate the counter.

Let us examine the flux of electrons which could be provided by fusion neutrons. The fusion burst can release a maximum of 3×10^{27} neutrons with an initial energy of 14 Mev, and after passing through the matter of the fireball, this energy is probably reduced to about 10 Mev.

For a relativistic particle the decay probability per centimetre is given by:

$$p = \Gamma/\beta\gamma c$$

where Γ is the decay constant $= 9 \times 10^{-4}$ per second for neutrons,

γ is the dilation factor $= (1 - \beta^2)^{-0.5}$.

Thus $p = 2 \times 10^{-13}$.

Making the same assumption as for the fission neutrons, we find the maximum possible value of the flux encountered by Ariel is 3×10^6 electrons per cm^2 per second. This crude calculation gives a hard upper limit which is nevertheless only about 30 % of the 'just saturation' flux for the geiger counter. On these grounds therefore we may reject fusion neutrons as providing the main flux of particles for burst A.

4. By a process of elimination, one possibility is left. This is that the trapped electrons in the outer belt were scattered by the hydromagnetic wave generated by the explosion, and many had their mirror points lowered so that they were scattered by the atmosphere.

Parker (1962) has made calculations of the Alfven wave velocities for altitudes up to 50,000 km. These calculations indicate that the Alfven wave from the explosion would reach the L = 4.5 shell, which contained Ariel at the onset of burst A, between 15 and 20 seconds after its initiation. This agrees with the delay of 20 ∓ 10 seconds which was observed by Ariel. The delay of 13 ∓ 7 seconds observed by Fenton's balloon at the L = 3 shell is also in good agreement with Parker's calculations. The maintenance of the apparent mirror point lowering after the hydromagnetic wave has passed through the outer radiation belt is possibly caused by the eastward drift of these electrons, whose mirror points are normally dropping closer to the atmosphere as they cross the Pacific Ocean.

This conclusion demonstrates that the outer belt electrons are sensitive to artificially produced hydromagnetic disturbances. This in turn lends support to Dessler's theory of the 'in situ' acceleration of the electrons which form the outer radiation belt.

6.4 The Johnston Island Shell.

Burst B was the first sign of a different phenomenon. On five successive orbits after the explosion, a region of very high particle intensities was observed by our instruments at heights of about 400 km. over the Pacific Ocean. The intensity was high enough, and the particles were sufficiently energetic to saturate both the geiger and the cerenkov detectors. The shape of this high intensity region is crudely represented in figure 29 by those parts of the satellite track where the cerenkov counter was completely saturated.

The interesting thing about these particles is demonstrated by figure 28 where some counting rate contours are drawn from geiger data for the last three of the five observations. These last three observations were chosen in order to allow some of the time dependance of the intensities to disappear (the first datum point was measured about three hours after the explosion). It can be seen that these particles would mirror below sea level if they reached the longitudes of the lowest mirror points. They evidently drift eastwards from approximately the

Figure 28

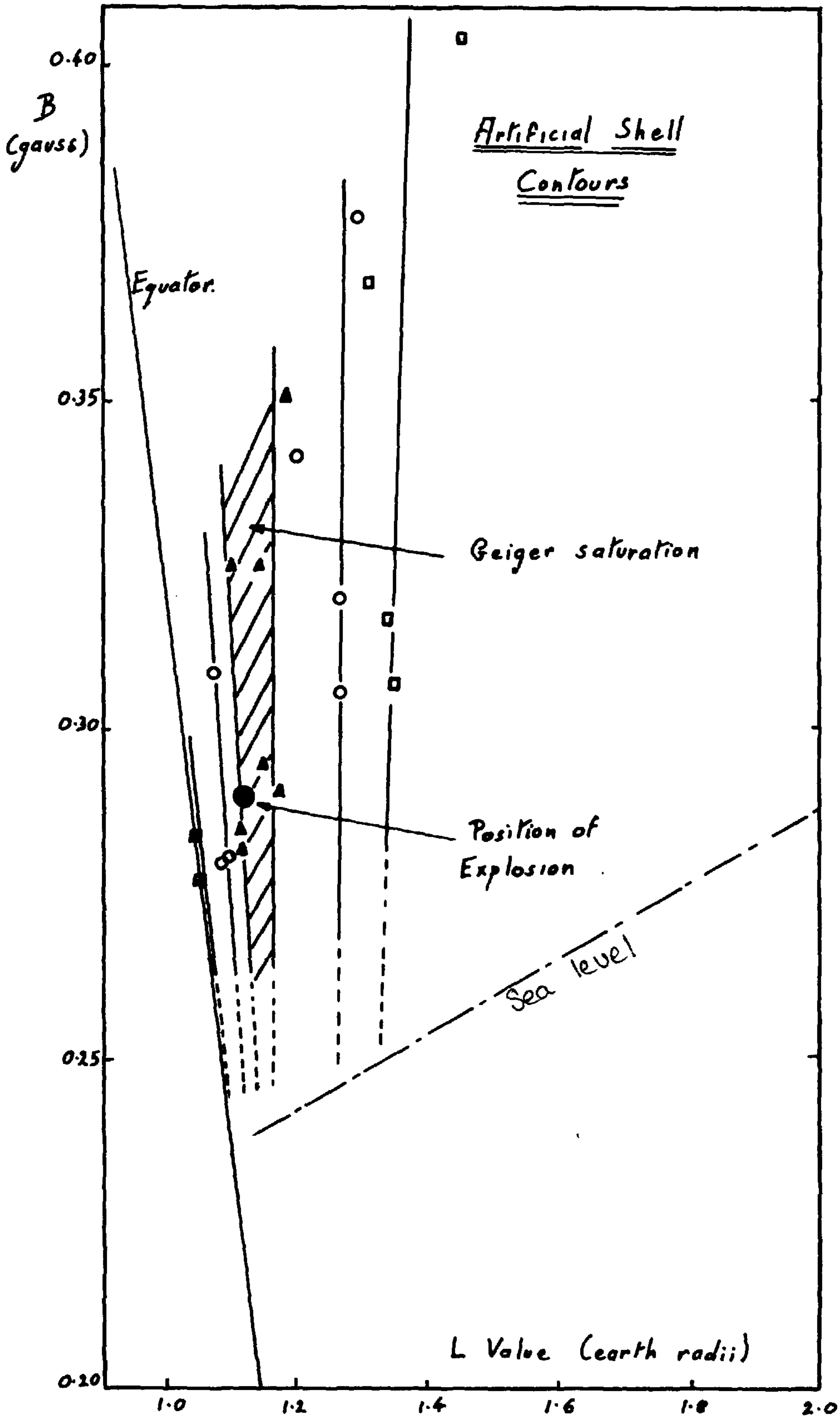
B (gauss)
0.40
0.35
0.30
0.25
0.20
Artificial Shell Contours
Equator
Geiger saturation
Position of Explosion
Sea level
L Value (earth radii)
1.0
1.2
1.4
1.6
1.8
2.0

and burst B for convenience. Burst A commenced within 20 $\mp$ 10 seconds of the explosion (the satellite was at an altitude of 819 km, latitude 52° S, longitude 163° W). The cerenkov detector, however, saw only burst B, it was unaffected by the particles in burst A. This is illustrated by figure 26 in which the group of points from burst A lies in a different area to those from burst B and in such a position that they show the cerenkov detector was counting at the normal cosmic ray rate during this burst.

Now protons released by the explosion would not be energetic enough to penetrate either of the detectors. The L values of the satellite position during burst A (L = 4.7 to 3.5 earth radii) ensured that no inner belt protons (L = 2.4 earth radii, see figure 27) were present. Thus from the discussion of cerenkov detector saturation in section 2.4, page 27, we may say immediately that in burst A the geiger was mainly counting either γ radiation or bremsstrahlung from electrons of energies less than about 2 Mev.

Multiplying the geiger saturation rate of 2,300 counts per interval by the geometric factors of the geiger counter from section 2.1 for bremsstrahlung and γ rays respectively it is found that the flux was at least:

10^7 electrons per cm^2 per second,

or 5×10^4 γ rays per cm^2 per second.

6.3.B Since the satellite was underneath the outer radiation belt at this time, it is tempting to say at once that burst A must be the

Johnston Island longitude and fall into the atmosphere somewhere before they reach the lowest mirror point line (figure 29).

The eastward drift means that these particles must be electrons, and since the cerenkov detector responds to them, there must be a large flux with energies greater than 2.5 Mev.

From Welch and Whitaker (1959) it is found that the time required for electrons with energies greater than 2 Mev to drift completely round the Earth must be less than 33 minutes. However Ariel observed this shell for over six hours on the 9th July, and found traces of it on the 10th, 11th and 12th July. This requires some form of injection mechanism for these particles.

The explanation of this electron shell must be that a number of charged fission products from the explosion were trapped in the Earth's magnetic field to form an arc in the Johnston Island longitude. These fission products decayed continuously to form fission electrons which were then swept eastwards by the magnetic field until they were scattered by the atmosphere over South America. The drift velocities for heavy ions similar to the fission fragments are very low, so that the western edge of this shell would be expected to creep westwards only very slowly. Alternatively, a group of slowly diffusing, neutral fission fragments would produce the same result. Similar effects were observed during the Argus explosions (Van Allen et alii 1959). It is interesting to notice that since these electrons are produced by the decay of fission fragments, they must have an energy spectrum given by the expression on page 79.

From figure 28 the core of the shell is found to lie at $L = 1.14 \mp 0.02$ earth radii. The explosion took place at $L = 1.12$ earth radii. This agreement supports the theory put forward above since the fission products whether charged or neutral (and therefore the electrons), would be expected to be tied to the magnetic shell in which the explosion ocurred.

6.5 The Artificial Radiation Belt.

After the explosion, apart from the regions mentioned above, the satellite ran into other large regions with particle intensities high enough to saturate both the geiger counter and the cerenkov detector. These regions were part of the artificial radiation belt. Figure 27 shows the natural radiation belts as seen by Ariel before the 9th July explosion, figure 30 shows the additional radiation contours observed between longitudes 40° E and 160° E on July 9th. Natural radiation belt intensities have been subtracted from this graph under the assumption that any disturbance of these natural intensities by the explosion was small. The broken line represents the position of sea level below the lowest mirror point line, and it can be seen that none of the particles observed in the radiation contours need have their mirror points below sea level in their drift around the Earth. Indeed, because this radiation was observed between longitudes 40° E and 160° E, in order for these electrons to have reached the point of observation they must have drifted eastwards from the explosion longitude, and so have already crossed at least once the line where they are most likely to mirror in the atmosphere and thus be scattered. This radiation therefore is truly trapped

Figure. 30

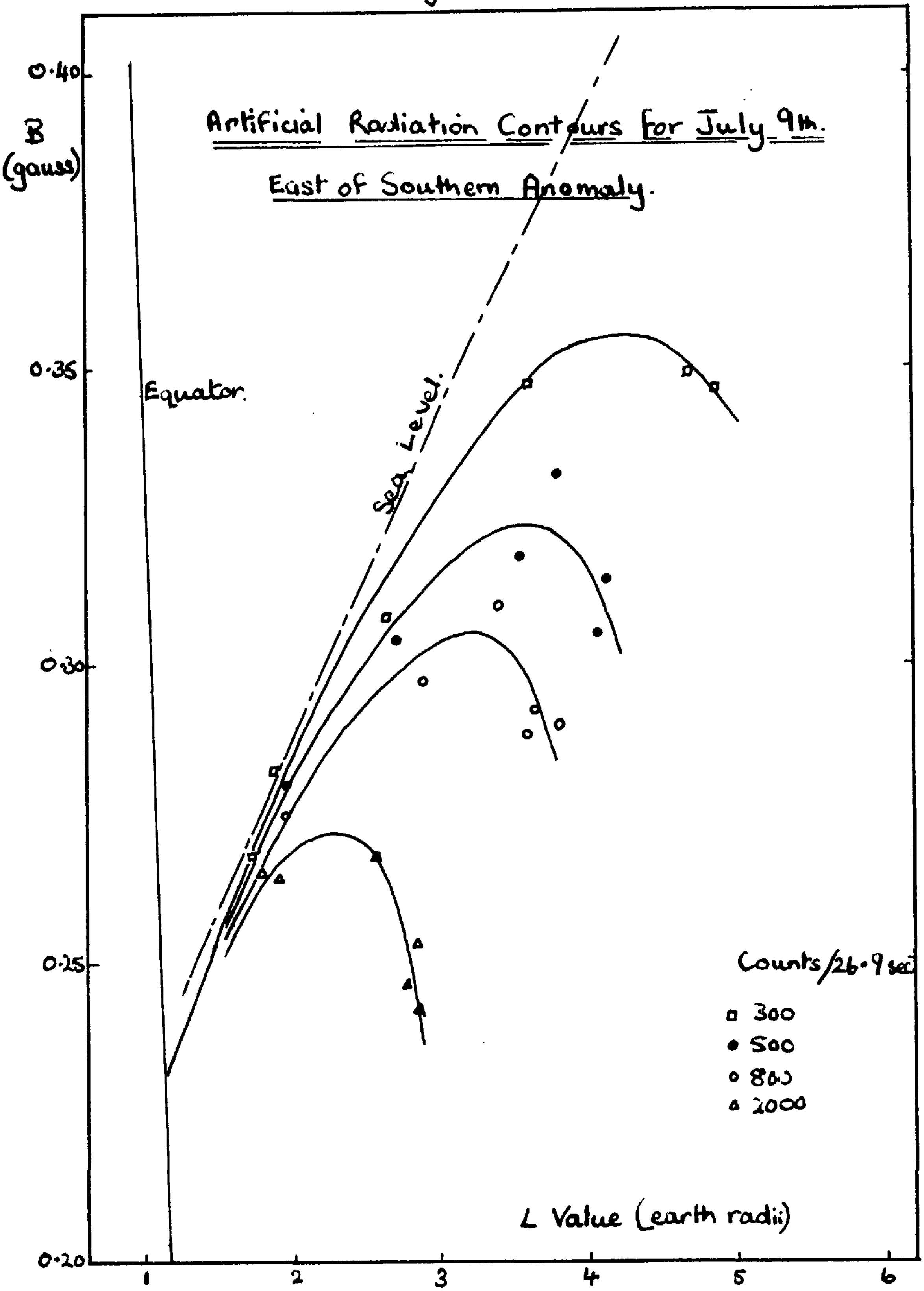
Artificial Radiation Contours for July 9th.
East of Southern Anomaly.
B (gauss)
0.40
0.35
0.30
0.25
0.20
Equator
Sea Level
Counts/26.9 sec
300
500
800
2000
L Value (earth radii)
1
2
3
4
5
6

in the sense that it may drift around the Earth at least once without being scattered and lost.

Additional radiation is observed out to values of L = 5 earth radii. It is not known how electrons from an explosion at L = 1.12 earth radii become trapped at such high L values; there are probably contributions from fission fragment decay electrons, neutron decay electrons, and disturbed outer belt particles. The presence of the fission fragment decay electrons was detected by the saturation of the cerenkov detector.

Figure 31 is intended to show crudely how the energy spectrum of the artificial electrons varies with L value. The vertical axis shows the counting rates of the geiger counter at instants when the cerenkov detector just saturated. This saturation will occur when a certain number of electrons per second, say N, is producing dark current in the photomultiplier. For a steeply exponential spectrum similar to the fission electron spectrum (page 79) most of these electrons will have energies near to the energy threshold, which is the energy at which electrons are just able to penetrate the wall of this counter. If we assume that the electrons we are considering have this type of energy spectrum, then as an approximation we can say that saturation of the cerenkov counter occurs when N electrons per second, having energies between 2 and 3 Mev, pass into the perspex sphere.

Now the threshold of the geiger counter for electrons is about 7 Mev. For a fission-like spectrum in the range 1 Mev $< E <$ 10 Mev the majority of geiger counts will be caused by electrons with energies just above the threshold, assuming the bremsstrahlung efficiency is less

Figure 31

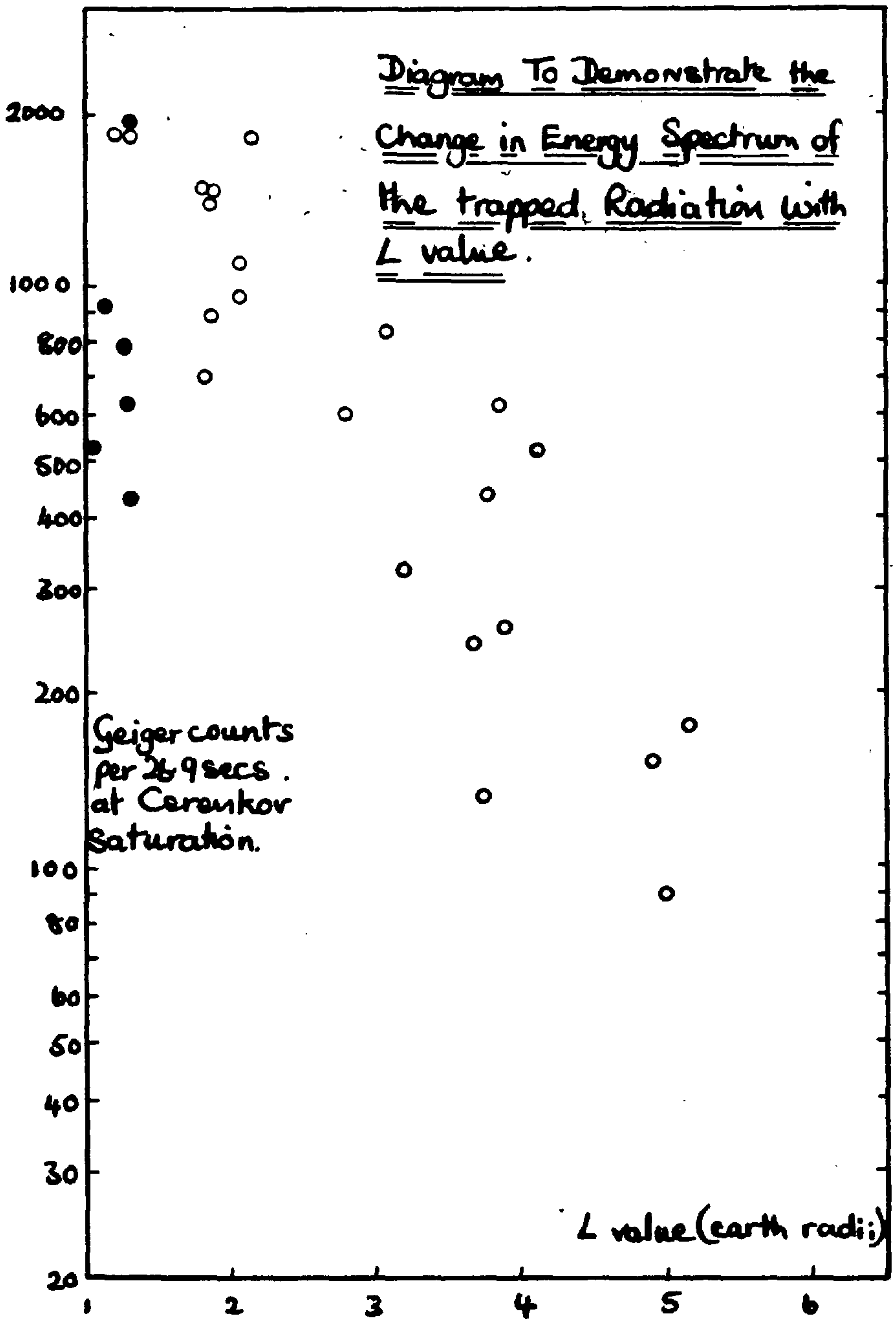
Diagram To Demonstrate the Change in Energy Spectrum of the trapped Radiation with L value.
2000
1000
800
600
500
400
300
200
100
80
60
50
40
30
20
Geiger counts per 26.9 secs. at Cerenkov Saturation.
L value (earth radii)
1
2
3
4
5
6

than 0.001 %. As a second approximation we may say that the geiger counter is only sensitive to electrons with energies greater than 7 Mev.

Thus the counting rates of the two detectors are sensitive to two different portions of the electron energy spectrum. By considering only the instants when the cerenkov detector just saturates, we fix the intensity of electrons in the 2 - 3 Mev energy range, and higher or lower counting rates of the geiger at these instants correspond to more or less electrons with energies greater than 7 Mev for a given number of electrons between 2 and 3 Mev. If, for example, the geiger counting rate is comparatively low at cerenkov saturation, then the slope of the energy spectrum must be relatively steep and there will be larger numbers of electrons with low energies. In this way the vertical axis of figure 31 gives a crude idea of the slope of the electron energy spectrum, so long as this spectrum is similar to the energy spectrum of electrons produced by the decay of fission fragments. Lower numbers on this axis indicate that the spectrum has a steeper slope.

The open circles represent points obtained in the artificial radiation belt, the filled circles represent data from the Johnston Island shell. This shell is known to have a fission spectrum as a result of the process by which it is formed, and it can be seen that at higher L values the slope of the energy spectrum of the artificial radiation belt electrons is steeper than the slope for a fission electron spectrum. This is evidence for the presence of soft electrons at high L values in addition to the fission spectrum.

It is interesting to notice that there was a six minute delay between the explosion and the first detection of fission decay β particles (burst B, figure 25). This time lag cannot be explained by longitudinal electron drifts. A more likely explanation is that this is the time required by neutral fission fragments to travel to the L = 3 earth radii shell at the satellite longitude (163° W at this time). The distance between this point and the explosion is roughly a minimum of 5,500 km, which gives these fission fragments velocities of 15 ∓ 5 km. per second. This is equivalent to a temperature of about 10^6 degrees absolute, which is a reasonable figure for a maximum temperature of the order of 10^7 degrees in the explosion. This decay of neutral fission fragments is a possible mechanism for the injection of fission β particles at high L values.

The artificial radiation belt created by starfish is also discussed in papers by O'Brien, Laughlin and Van Allen, 1962; Brown, Hess and Van Allen, 1963.

6.6 Decay of the Artificial Radiation Belt.

It has been explained how figure 30 illustrates the intensity contours of the additional radiation after it has crossed the Southern Anomalies. Figure 32 is taken from data collected between longitudes 180° W and 50° W, and shows the intensity contours of the additional radiation before it reaches the Southern Anomalies. The data for figure 32 were collected between 1400 hours and midnight on the 9th July, during which period the self-consistency of the data points indicates there was no large time variation of the contours shown.

Figure 32

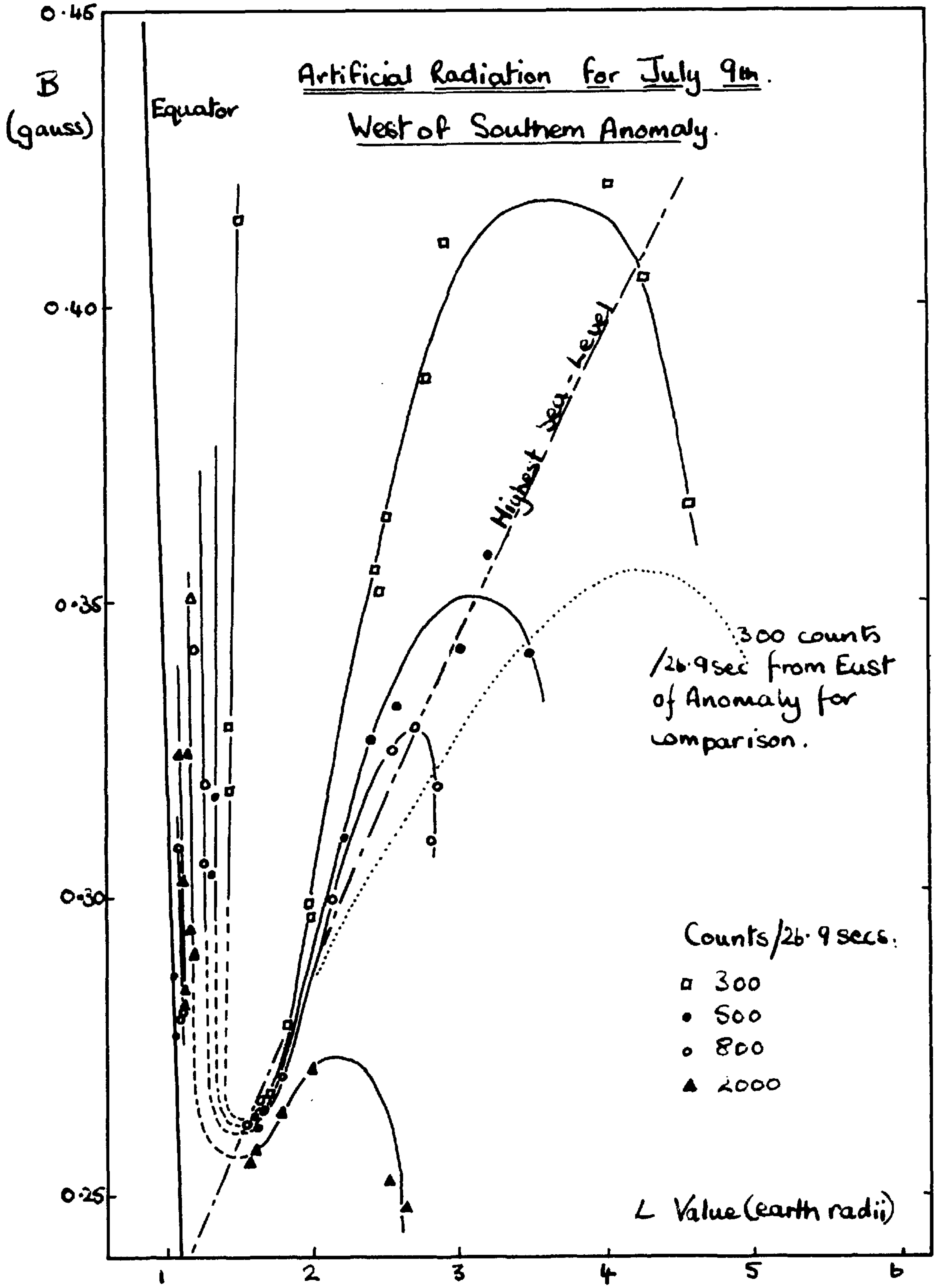
Artificial Radiation for July 9th.
West of Southern Anomaly.
B (gauss)
Equator
0·45
0·40
0·35
0·30
0·25
Highest sea-Level
300 counts /26·9sec from East of Anomaly for comparison.
Counts/26·9 secs.
300
500
800
2000
L Value (earth radii)
1
2
3
4
5
6

We can immediately say that the difference in the intensity contours between figures 30 and 32 is a result of electrons being lost into the atmosphere over South America. Notice that the Johnston Island shell disappears, as was mentioned earlier. Similarly the lobes of radiation between L = 2 and L = 5 earth radii in figure 32 shrink appreciably. The cerenkov detector indicated that the part of these lobes which disappeared into the atmosphere consisted of electrons with a flux of less than 10^4 particles per cm^2 per second with energies greater than 2.5 Mev. These regions therefore contained mainly soft electrons. Traces of this soft radiation were observed for more than 50 hours after the explosion. The most westerly point at which it was observed by the satellite was at longitude 170° E. From thence the radiation was seen to stretch over Alaska and North America to the Atlantic. Presumeably there was also a southerly belt of this radiation which our satellite was not in a position to see. As the times of flight of the electrons observed in this radiation are less than about one hour, they must be injected into these altitudes by some means. There appear to be two possible explanations.

a These are natural outer belt particles whose mirror points are being continuously disturbed by some unknown mechanism which lasts at least 50 hours. The L shells on which the soft radiation is observed do not coincide well with the shells containing the outer belt particles.

b These are artificial radiation belt particles which have their mirror points disturbed and their energy reduced by coulomb scattering in the atmosphere near their mirror points.

If (b) is accepted as being the most likely explanation, then this process is part of the decay mechanism of the artificial radiation belt. At first sight we would expect this type of decay process to affect only those particles with mirror points near to the atmosphere, and to produce roughly the same amount of scatter at all L values. However it is evident from the B - L diagram that the amount of scatter increases with increasing L. For example the scatter at L values of less than 2 earth radii produces a very low flux in the non-trapping region. This may be because the amount of time per orbit that a particle spends close to the atmosphere increases with increasing L value or it could be caused by slight hydromagnetic disturbances of the particles, the amount of disturbance increasing with distance from the Earth's surface. At present this experiment cannot distinguish between these two effects.

In figure 33 the shape of the '300 counts per interval' contour of the artificial radiation belt is plotted for the 9th - 12th July. No change is detectable between the contours for 10th - 12th July. It is reasonable to suppose that the difference between the contours is due to the decay described above, and that this mechanism has little effect after the first 24 hours

The data points for the 10th, 11th, and 12th July on this diagram were not selected for longitude; there appears to be little change in the flux contours as the radiation passes over the Southern Anomalies. Some structure is observeable near L = 2 earth radii which could not be resolved. The possibility of timing errors has been eliminated; it may be that the B and L values are inaccurate in this region.

Figure 33

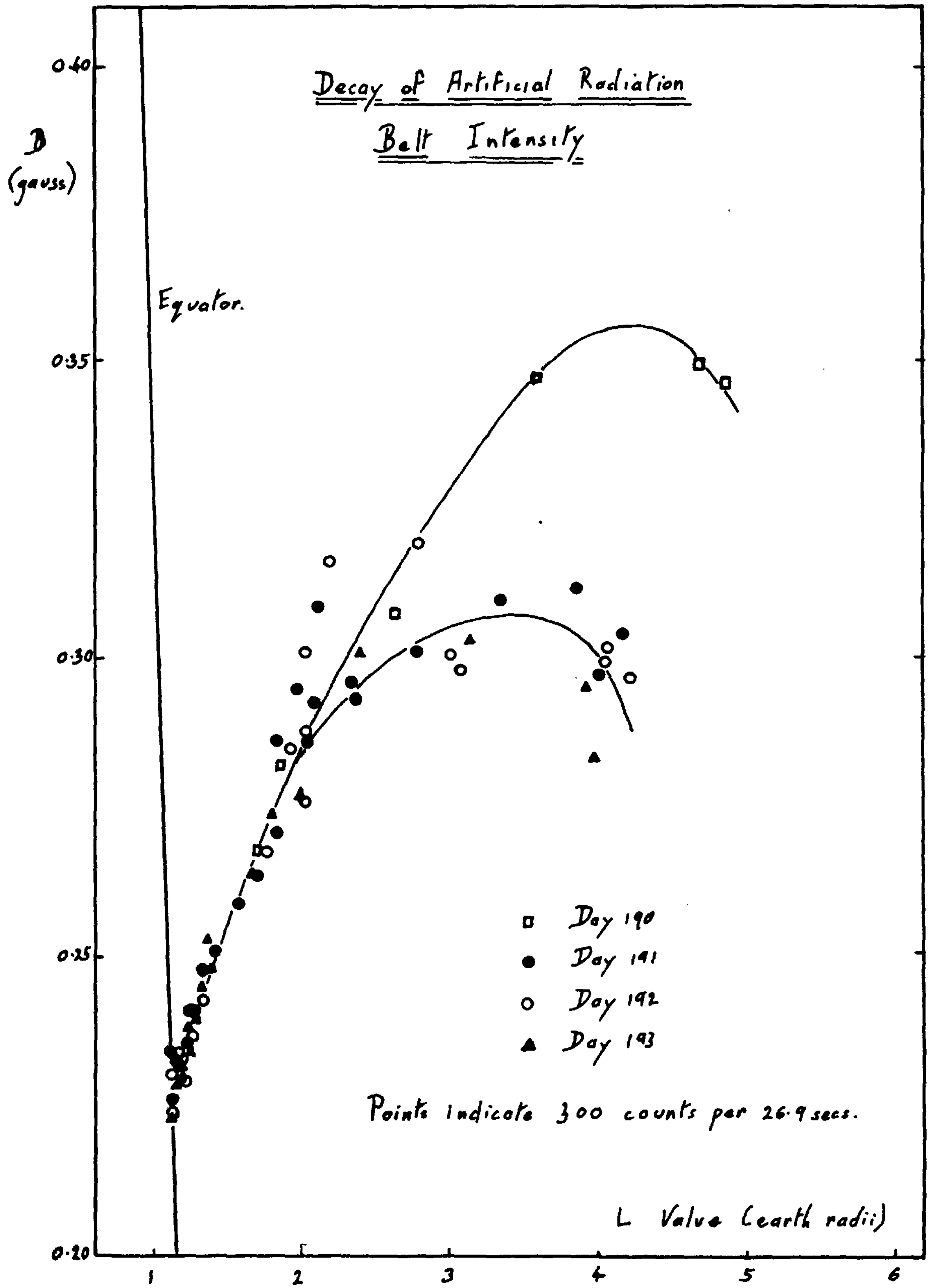
Decay of Artificial Radiation
Belt Intensity
B (gauss)
0·40
0·35
0·30
0·25
0·20
Equator.
Day 190
Day 191
Day 192
Day 193
Points indicate 300 counts per 26·9 secs.
L Value (earth radii)
1
2
3
4
5
6

6.7 Summary.

The most interesting piece of physics to emerge from this analysis is the evidence for the mirror point redistribution of the geomagnetically trapped radiation in the region between L = 4.7 and 3.2 earth radii by an explosion-generated, hydromagnetic wave. The observed velocity of the hydromagnetic wave agrees with Parker's calculated velocities within the limit of the experimental error. This provides experimental evidence to support the speculations that tho trapped particle populations are affected by hydromagnetic waves, and lends additional weight to the theory of the 'in situ' acceleration of outer belt particles by hydromagnetic waves generated at the surface of the magnetosphere.

An intense belt of electrons, presumeably generated by an arc of charged fission fragments, or a slowly diffusing group of neutral fission fragments was observed streaming eastwards towards South America. The core of this shell was found to lie at $L = 1.14 \mp 0.02$ earth radii. The explosion is reported to have taken place on the L = 1.12 shell. Traces of this shell still remained 3 days after the explosion.

An artificial radiation belt was observed; fission fragment electrons were detected out as far as L = 5 earth radii. From the Ariel results it seems likely that these were injected into these shell by neutral fission fragments. Note that the alternative theory of a bubble of charged fission fragments rising through the exosphere under the influence of magnetic pressure would be expected to have extended the core of the Johnston Island shell to much higher L values than were observed. Evidence was also found to show that the energy spectrum of the electrons has a steeper slope at higher L values for the altitudes scanned by Ariel.

The 'sweeping' effect of the Southern Anomalies on the lower edge of the artificial radiation belt has been clearly demonstrated by comparing diagrams 30 and 32. A short-lived form of decay mechanism has also been observed in operation. This could possibly be caused by small hydromagnetic disturbances lowering the mirror points of some particles in the newly-formed artificial radiation belt and allowing them to fall into the atmosphere over the Southern Anomalies.

This analysis does not exhaust the artificial radiation data collected by Ariel I. Further facts may be gleaned by closer examination of the records, in particular those collected after July 12th, which have not been used in this thesis.

APPENDIX A

CERENKOV COUNTER SATURATION

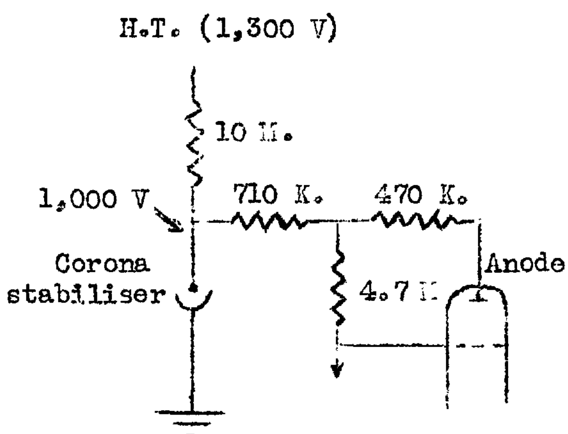

Photomultiplier High Tension Circuit.

Under conditions where the only current flowing from the anode of the photomultiplier is the dark current, about 15 microamps are taken by the corona stabiliser. If these 15 microamps are used by an increase of anode current caused by a large rate of small pulses, the corona stabiliser will just be switched off. In this condition, the anode of the photomultiplier is at a potential which is lower than in the first named condition by about 18 volts. It can be shown empirically that a reduction of about 50 volts at the anode of a photomultiplier which is being operated at 1000 volts, halves the gain. Thus an 18 volt reduction will bring about a negligible decrease in the gain. However, after the corona stabiliser is switched off, every extra microamp taken by the photomultiplier will reduce the anode potential by at least 10 volts. A background counting rate which produces 25 microamps at the anode will therefore be sufficient to reduce the gain to less than one quarter of its original value and will thus be able to 'turn off' the cerenkov detector.

But the gain of the photomultiplier flown was about 10^6 at 1000 volts (manufacturer's rating) and from the calibration curves in Appendix B, one relativistic electron passing through the centre of the sphere will release an average of one photo-electron from the photo-cathode. Allowing for the decrease in gain, this means one electron through the detector is equivalent to 10^5 electrons at the photomultiplier anode.

But 10^5 electrons per second equals approximately 10^{-8} microamps.

Thus the number of electrons which must pass through the detector to produce saturation is:

$$2 \times 10^7 \text{ per second.}$$

As the area of the detector is 80 cm^2, the flux required for saturation is a minimum of:

$$3 \times 10^5 \text{ electrons/second/cm}^2.$$

<u>Alternatively.</u>

We have shown that a drain of about 25 microamps is required from the anode of the photomultiplier for saturation of the cerenkov detector. The triggering level of the discriminator in the unit flown was set at 1000 milli-volts. Now consider the pulses produced at the anode by electrons passing through the perspex to be 100 mv high normally, or 10 mv high after the decrease in gain. The capacity in the anode circuit of the photomultiplier was about 25 pico-farads.

$$Q = C.V$$
$$= 2.5 \times 10^{-13} \text{ coulombs/pulse.}$$

Therefore we require about 10^8 pulses per second of the type considered above to keep the photomultiplier turned off. This is equivalent to a flux of:

$$10^6 \text{ electrons/second/cm}^2.$$

This figure does not disagree with that obtained in the previous calculation.

APPENDIX B

CERENKOV DETECTOR GEOMETRY

Sphere Geometry.

The path length of a particle passing through the perspex sphere will vary with the distance of the particle from the centre of the sphere. Let x be the total path length in the sphere, y the perpendicular distance of the path from the sphere centre, $2r_1$ the outside diameter of the sphere and $2r_2$ the inside diameter. By simple geometry it may be shown that:

$$x = 2(r_1^2 - y^2)^{\frac{1}{2}} - 2(r_2^2 - y^2)^{\frac{1}{2}}.$$

The real part of this curve is shown in figure 34, 50 mm being substituted for r_1 and 47 mm for r_2. As a first approximation the broken lines in this diagram may be taken to represent this curve. For convenience the two seperate sections of this approximation will be called the sphere 'centre' and the sphere 'edge' respectively.

Thus a particle may produce different amounts of light and therefore different pulse heights at the photomultiplier anode according to which part of the sphere it passes through.

Calibration Curves.

Apart from the variations in pulse height produced as explained above, the only other important geometrical effect considered here is whether the particle passes through the photomultiplier face or not. It is assumed that variations caused by different light collection

Figure 34

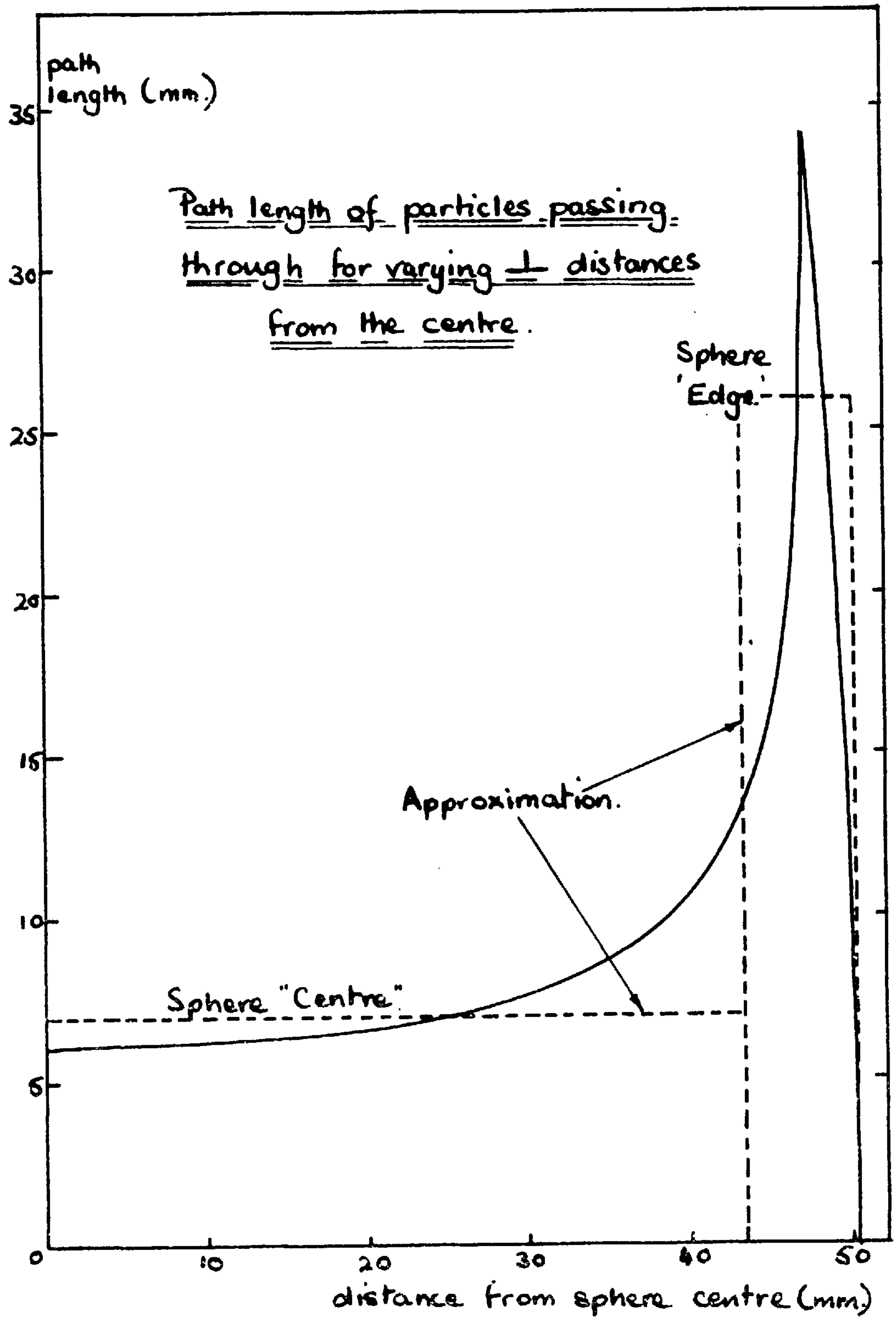
path
length (mm)
35
30
25
20
15
10
5
0
10
20
30
40
50
distance from sphere centre (mm)
Path length of particles passing
through for varying ⊥ distances
from the centre.
Sphere
'Edge'
Approximation.
Sphere "Centre"

efficiencies from different parts of the sphere are negligible (tests to detect this effect found no pulse height variations outside the experimental error of 15 %), all particles passing through the photomultiplier face are treated as if they were incident normally, and effects due to relativistic and non-relativistic particles passing sideways through the glass face are ignored. For the last-named effect the solid angle is small, approximately $\pi/3$ and the area is only 2.5 cm^2.

The curves in figure 35 were plotted using a two inch diameter scintillation telescope in conjunction with the cerenkov unit. The way in which the telescope and the unit were arranged is shown in the sketch by each curve. Curve A data are for particles passing wholly through the sphere 'centre', using the name given in the previous section, and curve B was plotted for particles passing through one thickness of perspex and the photomultiplier face. Since the light collected by the photomultiplier from that released in the perspex is an order of magnitude less than the light released in the photomultiplier face, the former will be ignored in this investigation.

The shape of curve B is determined mainly by the varying photocathode efficiency over the face, and by the varying probabilities of arriving at the first dynode for electrons released from different parts of the photo-cathode. These factors in turn depend on the method of depositing the photo-cathode and on the configuration of the electrodes. The shape of curve B was not found to differ appreciably for the types of E.M.I. and 20th Century tubes actually used, although an R.C.A. phototube of a different type of construction gave a markedly different curve.

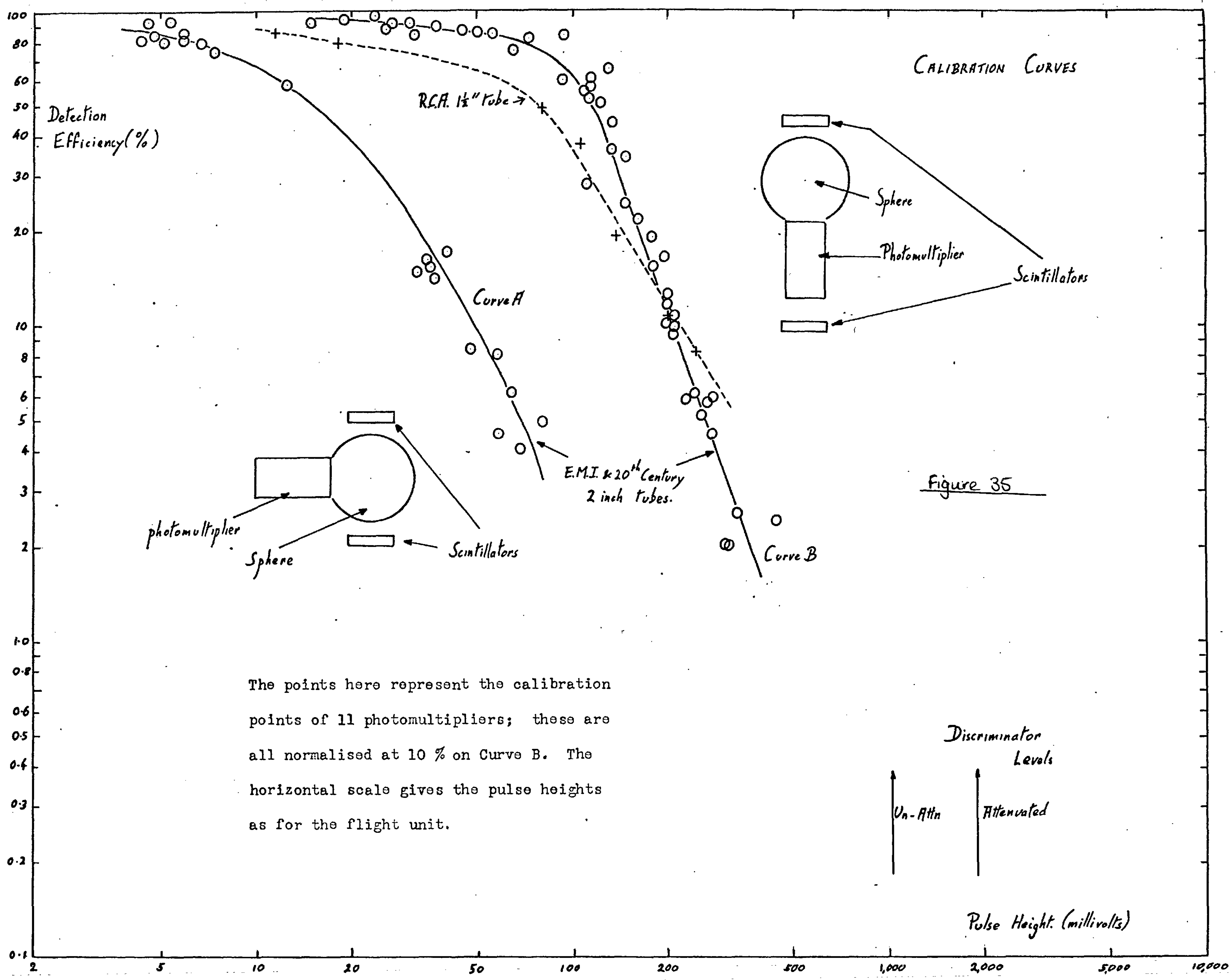

Figure 35

The points here represent the calibration points of 11 photomultipliers; these are all normalised at 10 % on Curve B. The horizontal scale gives the pulse heights as for the flight unit.

The shape of curve A depended mainly on statistics. The light from the perspex will fall evenly over the whole of the photo-cathode, so the geometry of the photomultiplier can have no effect on this curve. Since the telescope constrained us to examine only that part of the sphere where the path lengths are roughly the same, the geometry of the sphere can have little effect on this curve either. In figure 36 the distribution of points on curve A for one photomultiplier is compared with the shape of the normalised poissonian curve calculated for one particle. There is fairly good agreement. On these grounds we may state that the passage of one relativistic particle through the sphere 'centre' causes approximately one photo-electron to fall on the first dynode of the photomultiplier. Since the pulse heights for curve A were well submerged in the photomultiplier noise, which presumeably is mainly caused by single thermal electrons leaving the photo-cathode, this seems to be a reasonable statement.

The pulse heights which would be caused by multiply charged particles passing through the photomultiplier face may be found simply by multiplying the pulse heights of curve B by Z^2. For the passage of these particles through the sphere the problem is complicated by the better statistics as Z increases. As a further approximation, curve A has been assumed to be a sharp cut-off for values of Z^2 equal to or greater than 25.

Since the effective discrimination levels for the attenuated and un-attenuated sensitivities are known for the flight unit, its theoretical efficiencies may be calculated for particles of different charge passing

Figure. 36

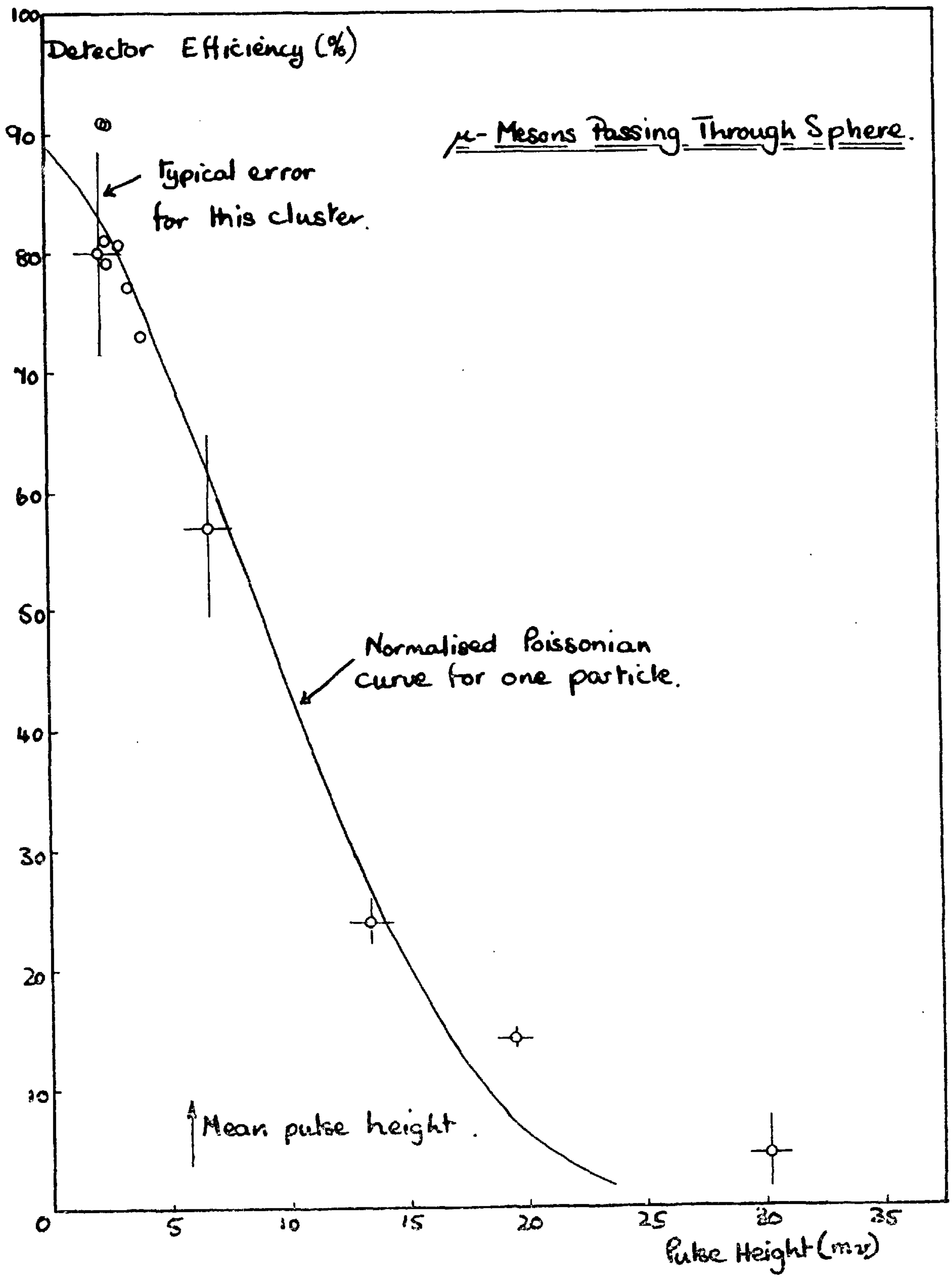
Detector Efficiency (%)
100
90
80
70
60
50
40
30
20
10
0
5
10
15
20
25
30
35
Pulse Height (mv)
μ- Mesons Passing Through Sphere.
Typical error for this cluster.
Normalised Poissonian curve for one particle.
Mean pulse height.

through the three seperate portions of the geometry. These efficiencies are given as percentages in the column labelled '%' in figure 37.

The charge spectrum of the primary cosmic radiation according to Waddington (1961) is shown by the relative numbers listed below.

H	6600
He	953
Li	3.9
Be	1.7
B	11.6
C	26
N	12.4
O	17.9
F	2.6
$Z \geq 10$	23.9

These have been normalised by taking $Z \geq 3$ as 100. If the efficiencies of the detector are multiplied by these abundance figures, the relative amounts of response will be found for differently charged particles passing through the three different parts of the detector. These numbers are shown in the 'Rel. No.' column of figure 37. In order to find the different contributions of these three parts of the geometry to the total counting rate of the detector it is necessary to take the area and solid angle of each of the seperate parts into account.

From the table it is calculated that the ratio of the counting rates in the attenuated and un-attenuated states at high lattitudes between April 26th and May 18th is 2.0 ∓ 0.7. The error given here arises from

Figure 37

A table of the theoretical relative effects of the heavy particles in the three portions of the detector geometry using the calibration of the instrument and the primary abundance spectrum given by Waddington (1961). This table was calculated for the period between April 27th and May 18th, 1962.

	SPHERE CENTRE Area = 60 cm^2 Solid angle = 4π				SPHERE EDGE Area = 18 cm^2 Solid angle = 4π				PHOTO-TUBE FACE Area = 20 cm^2 Solid angle = π			
	Attn.		Un-Attn.		Attn.		Un-Attn.		Attn.		Un-Attn.	
	%	Rel. No.	%	Rel. No.	%	Rel. No.	%	Rel. No.	%	Rel. No.	%	Rel. No.
H											0.1	6.6
He									0.9	8.5	5	48
Li									10	0.4	50	1.9
Be									45	0.8	80	1.4
B									76	8.8	100	11.6
C							100	26	85	22.1	100	26
N							100	12.4	100	12.4	100	12.4
O					100	17.9	100	17.9	100	17.9	100	17.9
F					100	2.6	100	2.6	100	2.6	100	2.6
$Z \geq 10$	100.% for $Z \geq 14$	?	100	23.9	100	23.9	100	23.9	100	23.9	100	23.9

the unknown quantity in the second column of the table. In practice, this ratio was 2.7. There is surprising agreement between these two figures in view of the crudity of the calculation.

Light-collecting Efficiencies.

The amount of light released inside the sphere from a typical μ-meson passing through it may be calculated using the equation quoted on page 46:

$$N = 2\pi\alpha d\left(\frac{1}{\lambda_1} - \frac{1}{\lambda_2}\right)(1 - 1/\beta^2 n^2).$$

Now the total energy, E, of a particle is given by:

$$E = \gamma mc = mc/(1 - \beta^2)^{\frac{1}{2}}.$$

For a μ-meson at sea level (200 Mev, say) we find:

$$m_\mu c = 106 \text{ Mev}$$

$$\text{So} \quad 1 - \beta^2 = 0.25,$$

$$\text{or} \quad \beta = 0.86$$

For a caesium-antimony cathode the wavelength range of the sensitivity is roughly from 3,500 A.u. to 5,500 A.u.. A typical path length through the sphere 'centre' is 6 mm. The refractive index for perspex is 1.54 (transmission range 3,400 A.u. to 20,000 A.u.). By substitution we find:

$$N = 200 \text{ photons}.$$

Now the overall efficiency of a fairly good photocathode is about 10 %. Thus to cause one photo-electron to fall on the first dynode, 10 photons must fall on the photo-cathode. Since the μ-meson originally produced 200 photons in the perspex, the efficiency of the photomultiplier for collecting light produced in the sphere is of the order of 5 %. This is lower than might be expected, and may be associated with the fact that more than 50 % of the light produced in the perspex is totally internally reflected, thus raising the number of times the light has to be diffused by the white paint before it is intercepted by the photo-multiplier.

ACKNOWLEDGEMENTS

Much of the work which formed the basis for this thesis was performed in the Physics Department of the Imperial College of Science and Technology, and I would like to thank Professor P.M.S.Blackett for the excellent facilities provided.

I would also like to express my sincere gratitude to Professor H. Elliot, my supervisor, for his suggestion of this project, for much advice, encouragement and many ideas. I am deeply indebted to Dr. J.J. Quenby for his remarkable liason work in the initial stages of the experiment and for many helpful suggestions during the preparation of this thesis. The programming of the computer was arranged by Dr. R.J. Hynds, who also assisted in the preparation of the apparatus and performed much of the preliminary data analysis in conjunction with Professor Elliot and Dr. Quenby. My thanks are due to him for this work and for many pleasant and helpful discussions.

I am especially grateful for the cooperation of Mr. Cail and Mr. Mayne of McMichael Radio Ltd, to Saunders-Roe Ltd who provided the facilities for proving the pilot experiment, and to Mr. R.C. Baumann and his team of the National Aeronautics and Space Administration for their enthusiastic assistance and guidance during the integration of the apparatus with the spacecraft. Unfortunately there is not room here for me to thank individually the many other persons and organisations without whose help this work would have been impossible, but to those of them who read this thesis I extend my sincere thanks.

Finally, I would like to thank the Department of Scientific and Industrial Research, the Royal Society and the United States Government who provided the large amounts of money necessary for the fruition of this project.

REFERENCES

Alfven H. 1950, Cosmical Electrodynamics (Oxford; Clarendon Press).

Alpher 1950, J Geophys Res, 55, 437

Armstrong A.H., Harrison Heckman and Rosen, 1961, J. Geophys. Res., 66, 351.

Arnoldy R.L., Hoffman and Winckler, 1960, J. Geophys Res., 65, 1361.

Atomic Energy Commission (U.S.), 1955, Reactor Handbook; Physics.

Biswas S., Fichtel and Guss, 1962, Phys. Rev., 128, 2756.

Brown, Hess, and Van Allen, 1963, J. Geophys. Res., 68, 605.

Cahill L. and Amazeen, 1962, Univ. of New Hampshire Publications.

Carter, Reines, Wagner and Wyman, 1959, Phys. Rev., 113, 280.

Casaverde M., Giesecke and Cohen, 1963, J. Geophys. Res. 68, 2603.

Christofilos N.C., 1959, J. Geophys. Res., 64, 869.

Cladis J.B., Chase, Imhof and Knecht, 1961, J. Geophys. Res., 66, 2297.

Davis and Williamson, 1962, see Hoffman R. A., Davis and Williamson, 1962 J. Geophys. Res., 67 5001.

Dessler A.J., 1958, Phys. Rev. Lett., 1 68.

Durney A.C., Elliot, Hynds and Quenby, 1962, Nature 195, 1245.

Dyce and Horowitz, 1963, J. Geophys. Res. 68, 713.

Edwards P.J., Fenton, Fenton and Greenhill, 1962, Nature, 196, 367.

Elliot H., Quenby, Mayne and Durney, 1961, J. Brit. I. R. E. 22, 251.

Elliot H., 1963, Progress in Cosmic Ray Physics, XXVI, 145.

Engel A.R., 1964, Thesis, Univ. of London, Phd.

Frank and Tamm, 1937, Dokl. Akad. Nauk., 14, 109.

Freden and White, 1959, Phys. Rev. Lett., 3, 9.

Freden and White, 1960, J. Geophys. Res., 65, 1377.

Gabites and Rowles, 1962, New Zeal. J. of Geol. and Geophys., 5, 920.

Gill P.J., 1963, New Zeal. J. of Geol. and Geophys., 5 943.

Gold T., 1959 Nature, 183, 355.

Gold T., 1962, Space Science Review, 1, 100.

Heckman H. A., and Armstrong, 1962, J. Geophys. Res., 67, 1255.

Hess W.N., 1962, Space Science Review, 1 279.

Holly and Johnson, 1960, J. Geophys. Res. 65, 771.

Hutner R.A. 1939, Phys. Rev. 55 15, 109, 614.

Johnson T.H., Rev. Mod. Phys., 10, 194.

Kaspor J.E., 1958, Il Nuovo Cim. Suppl., 11,.1.

Katcoff S., 1958, Nucleonics, 16, 78.

Kellogg P.J., 1959, Il Nuovo Cim., 11, 48.

Koenig H.P., 1940, Phys. Rev., 58, 385.

Kurnosova L.V., Logachev, Razorenov and Fradkin, 1962, Plan. Space Science, 11, 193.

Latter, Herbst and Watson, 1961, Annual Rev. Nuc. Sci., 11, 371.

Lemaitre G. and Vallarta, 1933, Phys. Rev. 43, 87.

Lencheck A.M. 1962, J. Geophys. Res., 67, 2145.

Lencheck A.M. and Singer, 1962, J. Geophys. Res., 67, 1263.

Motz H.T. and Carter, 1963, J. Geophys. Res., 68, 657.

McDonald and Webber, 1959, Phys. Rev., 115, 194.

McDonald and Webber, 1961, J. Phys. Soc. Japan, 17 Supp. A-II, 428.

McIlwain, 1961, J. Geophys. Res., 66, 3681.

Naugle and Kniffen, 1961, Phys. Rev. Lett., 7, 3.

Newman P., 1959, J. Geophys. Res., 64, 923.

Northrupp and Teller, 1960, Phys. Rev., 117, 215.

O'Brien B.J., 1962, J. Geophys. Res. 67, 1227.

O'Brien B.J. and Laughlin, 1962, J. Geophys. Res., 67, 2667.

O'Brien B.J., Laughlin and Van Allen, 1962, Nature, 195, 939.

O'Brien B.J., Van Allen, Laughlin and Frank, 1961, State Univ. Iowa publication SUI-61-23.

Parker, 1962, Space Science Review, 1, 62.

Peterson A.M., 1959, J. Geophys. Res., 64, 933.

Petrov Y.I. 1960, Reactor Sci., 12, 129.

Pizzella G., McIlwain and Van Allen, 1962, J. Geophys. Res., 67, 1235.

Pomerantz and Witten 1962, J. of Phys. Soc. Japan, 17, Suppl. A-III, 40.

Quenby and Wenk, 1962, Phil. Mag., 7, 1457.

Rosser W., O'Brien, Van Allen, Frank and Laughlin, 1962, J. Geophys. Res., 67, 4533.

Stormer C., 1955, The Polar Aurora, Oxford University Press.

Singer S.F., 1958, Phys. Rev. Lett., 1, 171 and 181.

Singer S.F., 1962, Nature, 196, 307.

Vallarta M.S., 1948, Phys. Rev., 74, 1837.

Van Allen J.A., 1958, I.G.Y. Satellite Report 13, (1961).

Van Allen J.A., Ludwig, Ray and McIlwain, 1958, Jet Propulsion 28, 588.

Van Allen et al. 1959, I.G.Y. Satellite Report 9, 1152.

Van Allen J.A. and Frank, 1959, Nature 183, 430.

Van Allen J.A., McIlwain and Ludwig, 1959, J. Geophys. Res. 64, 877.

Van Allen J.A., et al., 1962, State Univ. of Iowa publication SUI-62-26.

Vernov S.N., 1958, Fifth Gen. Assembly of C.S.A.G.I., Moscow.

Vernov S.N. and Chudakov, 1960, Space Research I, North Holland Pub. Co., Amsterdam.

Waddington, 1961, J. Phys. Soc. Japan 17, Suppl. A-III, 14.

Webber W., 1957, Il Nuovo Cim. 4, 1285.

Webber W. and Quenby, 1959, Phil. Mag. 4, 654.

Welch J.A. and Whitaker, 1959, I.G.Y. Satellite Report 9, 1190.

Willmore A.P., 1962, Private Communication.